Exciton-polaritons in low dimensional structures

Goran Pavlovic

N° d'Ordre: D.U. 2069

UNIVERSITE BLAISE PASCAL
U.F.R. Sciences et Technologies
ECOLE DOCTORALE DES SCIENCES FONDAMENTALES
N° 657

THESE

presentée pour obtenir le grade DOCTEUR D'UNIVERSITE,
specialité: Physique des Materiaux, par

Goran PAVLOVIC

Master

Exciton-Polaritons in Low-Dimensional Structures

Soutenue publiquement le 17/11/2010, devant la comission d'examen:

WHITTAKER David	**rapporteur**
KAVOKIN Alexey	**rapporteur**
RICHARD Maxime	**examinateur**
SHELYKH Ivan	**Prèsident**
MALPUECH Guillaume	**directeur de Thèse**
GIPPIUS Nikolay	**directeur de Thèse**
SOLNYSHKOV Dmitry	**invité**

Contents

Acknowledgment

This thesis has been done within the Chaire d'Excellence de l'Agence Nationale pour la recherche, from December 2007 - November 2010 in LASMEA (Laboratoire des Sciences et Matériaux pour l'Electronique) in the Group "Optoélectronique Quantique et Nanophotonique".

Before all I would like to thank to my parents - Nada and Zoran. Without their support, of any kind, they have given me through the years, I would not be able to finish this work.

Certainly my supervisors Guillaume Malpuech and Nikolay Gippius merit my profound gratitude. First, for the competent leading in my scientific maturation. Sometimes it was needed to get over childhood diseases as I was a newcomer in the world of exciton-polaritons. The cure I got in form of very pedagogical instructions helped me a lot to get on my feet and enjoy playing in the exciton-polaritons playground. Second, apart the time we spent solving scientific problems I appreciate very much the moments we were just drinking some good wine or retelling anecdotes.

I profited also from collaboration with Ivan Shelykh. A lot of work we have done together and I learned many new things inspired by his ideas and previous research in domains like mesoscopic physics or polariton pseudospin.

I am glad to have met Dmitry Solnyshkov, Robert Johne, and Hugo Flayac. We have been sharing not just the same office but also some of the best hours of my stay in Clermont-Ferrand. Their contribution to my scientific formation is not negligible.

Introduction

Excitons-polaritons are the eigenmodes of system consisting of semiconductor excitons coupled to photons in the case, when strength of this coupling overcomes the losses induced by excitonic or photonic modes (strong coupling regime). They have been theoretically predicted independently by Hopfield [1](1958) and Agranovich(1959) [2], after Pekar (1957) [3] explained in terms of additional waves (or Pekar's waves) a series of experiments on optically pumped excitons. Thirty years later Ulbrich and Weisbuch measured polariton dispersion in GaAs [4].

The interest for polaritons is both fundamental, for the studying of interaction of light with the matter, and applied, because the modern-era technologies are based on semiconductor materials. The term polaritons will be used throughout this thesis, referring always to exciton-polaritons, but it should be noted that polaritons can also arise from the coupling of other type of quasiparticles with light, like phonon-polaritons, for example.

Polaritons, emerging from mixing of matter and light, as composite particles possess very interesting properties inherited from their components.

First, they obey the Bose-Einstein statistics, undergoing at low temperatures a phase transition to Bose-Einstein condensation (BEC). It is a new collective state of matter in which we cannot anymore distinguish individual entities. This collective behavior is characterized by coherence and occurs at the lengths smaller than the coherence length. After a long search for the experimental evidence of BEC (seven decades), Cornell and Wieman reported in ref. [5] on the atomic Bose-Einstein condensate at nanoKelvin temperature (and received the Nobel Prize for this discovery, together with Ketterle a few years later). Such a small temperature, coming from the high mass of the atomic species (this dependence will be the subject of section on Bose-Einstein condesation), prohibits any room-temperature applications. Contrary to atoms, polaritons are quasiparticles of ultrasmall effective mass: compared to atoms, their mass is typically eight orders of magnitude smaller. Such a light mass leads to high temperatures at which polaritons condense in the Bose-Einstein sense. BEC of polaritons was the first time proposed by Imamoglu in a form of low-pumping inversionless polariton laser [6]. At room-temperature polariton lasing has been predicted in GaN-based microcavity by G. Malpuech in 2002 [7].

Second, to organize polariton regime one needs to confine the light, and the efficiency of

this confinement determines the polariton life-time being several tens of picoseconds. The finite life-time of polaritons in another striking difference of a polariton BEC comparing to an atomic BEC.

Third, interaction of polaritons governed by their excitonic part is responsible for variety of nonlinear behaviors, the most important being the blue shift effect of polariton dispersion. Parametric oscillations [8], bistability and multistability [9] are also effects arising from nonlinearity of polariton system under study.

The last but the most fundamental property of polaritons is their pseudospin. Total angular momentum of a polariton state has two projections on the structure growth axis: $+1$ and -1. Polarization of emitted or absorbed light determined by the polariton pseudospin [10].

In this thesis these properties will be analyzed in several situations and for structures of low dimensionality: quantum dots, quantum wires, and planar microcavities.

In Chapter 1 will be given a brief overview of 0D, 1D, and 2D structures. General theoretical introduction to polaritons will be made by original approach used by Hopfield [1]. The mathematical tools necessary to analyze the physics of BEC , including the Gross-Pitaevski (GP) equation will be considered in this chapter also. Pseudospin formalism as an useful representation of polariton polarization degree of freedom will be detailed.

Chapter 2 is devoted to quantum wires. The so-called whispering gallery modes, having momentum in the plane containing wire's cross-section, are analyzed and main effects are addressed in the general case of anisotropic systems described by some index of refraction. Further we are going to treat the case of polariton formation in ZnO wires introducing excitonic dielectric response of this material. The experimental results, as we will see, are very well reproduced by this model.

In the Chapter 3 Bose-Einstein condensation is analyzed for spinor condensates which is the case of polaritons. Josephson-type dynamics in which two subsystems of a large one couple and exchange particles by tunneling from one to another is discussed. The concept of coupled spinor components in GP-like equations is used to consider Josephson effect of polaritons.

Chapter 4 starts with an introduction to Aharonov-Bohm effect, as the best known representation of geometrical phases. Another geometrical phase - Berry phase, occurring for a wide class of systems performing adiabatic motion on a closed ring, is main subject of this section. It is intuitively very similar to the Aharonov-Bohm effect, but Berry phase is a more general concept and one could see Aharonov-Bohm effect like a kind of Berry phase. We will present a proposal for an exciton polariton ring interferometer based on Berry phase effect.

In Chapter 5 will be considered a 0D system: strongly coupled quantum dot exciton to cavity photon. Here a novel nonlocal effect, quite different from the Aharonov-Bohm effect

(which is one typical example of nonlocality), will be studied. This effect is called quantum entanglement. The modern quantum mechanics and disciplines like quantum computation and quantum communications emerged after the effect of entanglement inspired a fruitful debate among the fathers of the Theory. We will see how one can obtain entangled states by embedding a quantum dot in a photonic crystal. This recovers the degeneracy of biexciton cascade, the system in subject in this chapter, naturally destroyed by splitting of the intermediate states of the cascade.

Chapter 1

Exciton-polaritons

In this chapter a general introduction to the field of excitons-polaritons will be given together with few basic theoretical concepts of its phenomenology. A review of excitons in structures of low dimensionality will be useful to compare their binding energies and wave functions in these different structures, namely quantum dots, quantum wires, and planar microcavities. Two possible scenarios depending on the confinement strength - strong and weak confinement will be overviewed. Then we will consider quantization of an optical mode and how its interaction with light depends on the quantization volume. Polaritons, arising from strong coupling regime (interaction energy of photon with excitons overcomes the losses for both) will be considered in bulk materials and microcavities, the last being the most studied type of confined structures. Bose-Einstain condensation phenomena and pseudospin formalism will be equally treated here.

Contents

1.1 Low dimensional semiconductor structures: excitons

Semiconductor systems of low dimensionality are the subject of this thesis. They are systems which motion is 'frozen'(or trivial) in some (or all) spatial dimensions, contrary to the bulk materials, where motion is allowed in all directions.

Elementary excitations of semiconductors are called excitons. It is a quasiparticle [11] arising from many body formalism [12], for which the vacuum is defined by full valence band and empty conduction band separated by the band-gap energy E_g. They are formed by a Coulomb-correlated conduction band electron and a valence band hole. When the distance between exciton components, electron and hole, is larger than lattice parameter, which is true for semiconductor excitons we have so-called Wannier-Mott excitons for which the effective mass approximation can be used. Even at room-temperature concept of excitons is valid as their thermal energy is still much smaller than the binding energy of exciton components.

Conduction band symmetry is of s type and has no degeneracy (orbital momentum L=0) while valence band state is p symmetric (orbital momentum L=1) and has three different projections of angular momentum on some arbitrary axis: $l = -1, 0, 1$ [13]. If we account for spin degree of freedom we will have for the total angular momentum operator $J = L + S$ and corresponding eigenvalues will take the values $|l - s| \leq j \leq l + s$. Conduction band electrons therefore have $j = 1/2$ and valence bend holes $j = 1/2, 3/2$. Hole states $j = 1/2$ and $j = 3/2$ can be characterized in the sense of effective mass approximation by two different effective masses. One is called light hole and another called heavy hole state, respectively. This leads to heavy and light hole excitons.

Exciton two-particle envelope function $\Psi(\vec{r}_e, \vec{r}_h)$, in the bulk and without taking into account the spin degree of freedom is given by Schrödinger equation [14]

$$H_{ex}\Psi(\vec{r}_e, \vec{r}_h) = E\Psi(\vec{r}_e, \vec{r}_h), \tag{1.1}$$

where the exciton Hamiltonian has the form

$$H_{ex} = H_e + H_h + E_g - \frac{e^2}{4\pi\varepsilon\,|\vec{r}_e - \vec{r}_h|} \tag{1.2}$$

with $H_{e.h} = -\hbar^2 k_{e,h}^2/2m_{e,h}$ being the single particle Hamiltonian of free electrons (holes) of effective mass $m_e(m_e)$. The last term of equation 1.2 stands for Coulomb interaction of two particles having opposite charges: e and -e, interacting in surrounding described by a dielectric constant ε. Changing to relative and center of mass coordinates: $\vec{r} = \vec{r}_e - \vec{r}_e$ and $\vec{R} = (m_e\vec{r}_e + m_h\vec{r}_h)/(m_e + m_h)$ one can decouple wave function in this two directions:

$$\Psi(\vec{r}_e, \vec{r}_h) = \frac{1}{\sqrt{V}}\varphi_{n_r l}(r)e^{i\vec{K}\vec{R}} \tag{1.3}$$

with n_r being radial, l orbital quantum number and $\vec{K}$ center of mass wave vector. The wave function $\varphi_{n_r}(\vec{r})$ describing relative motion satisfies the Wannier equation [14] which for $l = 0$ reads

$$E_{n_r}\varphi_{n_r}(r) = \left(-\frac{\hbar^2\Delta_r}{2\mu} - \frac{e^2}{4\pi\varepsilon\,|\vec{r}|}\right)\varphi_{n_r}(r). \tag{1.4}$$

Here $\mu = m_e m_h/(m_e + m_h)$ denotes reduced mass. The equation 1.4 has the same form as Schrödinger equation of hydrogen atom. For $E_{n_r} < 0$ we have bound states, the ground one ($n_r = 1$ and $l = 0$) is given like in the case of hydrogen atom by

$$.\varphi_{1s}(r) = \frac{e^{-r/a_B}}{\sqrt{\pi(a_B^{3D})^3}}. \tag{1.5}$$

The exciton Bohr radius $a_B^{3D} = \hbar^2\varepsilon/e^2\mu$ tells us the length after which exciton wave function rapidly goes to zero. The binding energy of electron and hole in exciton ground state is inversely proportional to it: $E_B = \hbar^2/2\mu\left(a_B^{3D}\right)^2$. Typical values for bulk GaAs, one of the most studied semiconductor material are : $E_B = -4.8meV$ and $a_B^{3D} = 11.6nm$. The larger Bohr radii and the smaller binding energies of excitons in semiconductors with respect to atoms reveal that analogy with atoms is only formal. Due to absence of any confinement in z-direction the bulk envelope function 1.3 is simply multiplied by plane wave $e^{ik_z z}$ with wave number k_z taking any real value.

$2D$ structures possess confinement of motion in one spatial direction. The structure which will be studied in this thesis is a quantum well (or several quantum wells) embedded in the antinodes of electromagnetic field formed in a microcavity made by distributed Bragg reflectors. The electron and hole confinement in semiconductor quantum wells is provided putting two semiconductors in contact and creating a potential barrier due to energy difference of the valence and the conduction bands in growth direction. Due to this we have to add in the exciton Hamiltonian 1.2 extra terms corresponding to the confinement of electron and hole motion in structure growth direction - z-axis: $V_e(z_e)$ and $V_h(z_h)$. Depending on the ratio of quantum well thickness a and the exciton Bohr radius, we can distinguish two limiting cases, so called weak confinement regime for which $a/a_B >> 1$ and strong confinement regime for which $a/a_B << 1$. The first one is very similar to bulk semiconductor case, except that instead of $e^{i\vec{K}\vec{R}}$ we have $e^{i\vec{K}_\parallel\vec{R}_\parallel}\cos(\nu\pi Z/a)$ in exciton envelope function for odd ν and $e^{i\vec{K}_\parallel\vec{R}_\parallel}\sin(\nu\pi Z/a)$ for even ν. Z is z-component of center of mass radius vector. Quantization in the z-direction includes exciton as a whole, and relative motion has both in-plane and confinement direction components. The effect of confinement is present only through the modification of the center of mass motion but not the relative one.

In strong confinement regime electron and hole are quantized separately because of very thin well. The wave function part which describes relative motion from the same

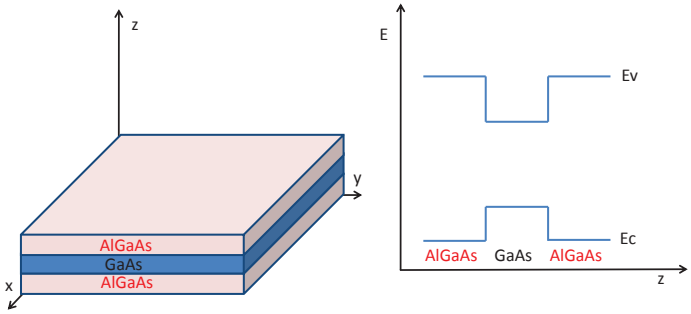

Figure 1.1 | GaAs/AlGaAs heterostructure (left) with the conduction-valence band energy offsets (right)

reason depends not on whole relative radius vector r but on its in-plane component $\rho = \rho_e - \rho_h$. The total wave function of the ground state is given by

$$\Psi^{2D}(\vec{r}_e, \vec{r}_h) = \sqrt{\frac{2}{S\pi}} \frac{4}{a a_B^{2D}} e^{i\vec{K}_\parallel \vec{R}_\parallel} \cos(\pi z_e/a) \cos(\pi z_h/a) e^{-2\rho/a_B^{2D}}. \tag{1.6}$$

The binding energy is 4 times the bulk value $E_B^{2D} = 4E_B$ if the motion is completely two dimensional. That means an infinitely narrow QW (which then has to be infinitely high to keep the bound state). 2D Bohr radius is half of it in a bulk $a_B^{2D} = a_B^{3D}/2$. This is how the strong confinement regime influences the exciton properties.

In quantum wires confinement is realized in two spatial dimensions while the motion in third dimension is unrestrained. In weak confinement regime relative motion of electron and hole rests unaltered and like in microcavities one should replace bulk plane wave $e^{i\vec{K}\vec{R}}$ by $e^{i\vec{K}_z\vec{Z}}\phi(X)\phi(Y)$ for the case of quantum wire. Function ϕ depends on wire shape. For example in rectangular wires it is a product of sines or cosines (for an even or an odd harmonic in x or y direction, respectively). For circular cross-section wires one should replace this product by Bessel functions. In the strong confinement regime the relative motion is restrained in the cross-section of wire and relaxed along z-direction and following the same reasoning like for QWs one can write the wave function:

$$\Psi^{1D}(\vec{r}_e, \vec{r}_h) = C e^{i\vec{K}_z\vec{Z}} \phi(x_e, y_e)\phi(x_h, y_h) e^{-z/a_B^{1D}} \tag{1.7}$$

It was shown that in an ideal quantum wire, for which we take $x_e = x_h$ and $y_e = y_h$, binding energy E_B^{1D} diverges [15]. But if we take into account the displacement of electron from hole in the cross-section by introducing a small parameter δ Coulomb interaction is regularized to $V_{1D}(z) = (|z| + \delta)^{-1}$ giving a finite value of E_B^{1D} satisfying following

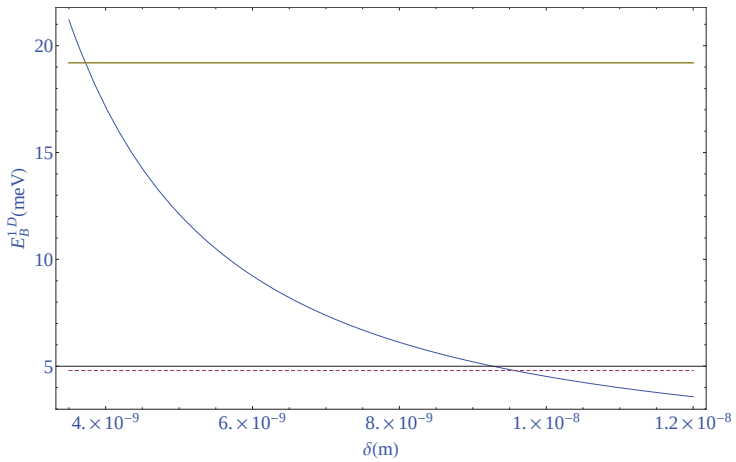

Figure 1.2 | Binding energy E_B^{1D} for a GaAs quantum wire (full blue line) vs electron hole displacement δ. Dashed line is bulk exciton binding energy while green line represents $E_B^{2D} = 4E_B$.

expression [13]:

$$\frac{\delta}{a_B^{3D}} = \frac{1}{2}\sqrt{\frac{E_B^{3D}}{E_B^{1D}}}\exp(-\frac{1}{2}\sqrt{\frac{E_B^{3D}}{E_B^{1D}}}). \tag{1.8}$$

Controlling parameter δ by tuning confinement potential it is possible to tune exciton binding energy up to very high values for small δ. Differently from microcavities where an upper limit for binding energy $E_B^{2D} = 4E_B$ exists, in wires such limit does not exist (the Fig. 1.2). High binding energies are advantageous from the point of view of excitonic physics at room temperature.

Quantum dots are strained in all spatial directions thus quasi-$0D$ structures. They are constituted of hundreds or only of a few atoms, having different shapes. Quantum dots of rectangular or spherical geometry are very well studied both theoretically and experimentally. As the motion is fully quantized energy spectrum of excitons is discrete. Exciton concept in quantum dots is valid until the exciton Bohr radius exceeds the dot size, otherwise system prefers to form uncorrelated electron hole pairs than excitons. Weak confinement occurs for confinement energy lower than binding energy of exciton in quantum dot while strong confinement establishes in the opposite case. In the first scenario exciton is more similar to bulk exciton, like it was a case for $2D$ and $1D$ structures, with the difference that center of mass motion is quantized while in the last situation the exciton wave function becomes product of single particle functions of electron and hole:

$$\Psi^{0D}(\vec{r}_e, \vec{r}_h) = \phi_e(\vec{r}_e)\phi_h(\vec{r}_h). \tag{1.9}$$

Discrete nature of QD spectra is the reason why the dots are usually called 'artificial atoms'.

1.2 Optical mode confinement

The quantization procedure of electromagnetic field leading to quanta of light - photons will be briefly discussed here following more rigorous treatment of reference [16]. We will concentrate on the case of light confinement in an optical cavity. In general, Lagrangian density of electromagnetic field $\mathcal{L}$ is

$$\mathcal{L}_{EM} = \frac{1}{2}(\varepsilon_0 E^2 + \frac{1}{\mu_0} B^2), \tag{1.10}$$

The fields $\vec{E}$ and $\vec{B}$ can be expressed in terms of electromagnetic four-potential $A^\alpha = (\phi/c, \vec{A})$

$$\vec{E} = -\nabla\phi - \frac{\partial \vec{A}}{\partial t}, \tag{1.11}$$

$$\vec{B} = \nabla \times \vec{A}. \tag{1.12}$$

One can show that Maxwell's equation follows directly from Lagrangian 1.10 making replacement given by 1.11, 1.12 and then performing usual variational procedure with respect to components of four-potential A^α. The result is:

$$\nabla \times \vec{E} = -\frac{\partial \vec{B}}{\partial t}, \tag{1.13}$$

$$\nabla \times \vec{B} = \frac{1}{c^2}\frac{\partial \vec{E}}{\partial t}, \tag{1.14}$$

$$\nabla \vec{E} = 0, \tag{1.15}$$

$$\nabla \vec{B} = 0. \tag{1.16}$$

where the total charge and current are set to zero as we are interested in a such kind of problems. We will consider that electromagnetic field is confined within a rectangular volume of space L^3 with dielectric constant ε_0. In Coulomb gauge: $\nabla\vec{A} = 0$ vector potential $\vec{A}$ satisfies (from Maxwell's equations) an ordinary wave equation

$$\nabla^2 \vec{A} - \frac{1}{c^2}\frac{\partial^2 \vec{A}}{\partial t} = 0, \tag{1.17}$$

Thus one can make the Fourier expansion of $\vec{A}$ in propagating plane waves, which are the proper modes in the case of a very large volume

$$\vec{A}(\vec{r}, t) = \frac{1}{\sqrt{\varepsilon_0 L^3}} \sum_{\vec{k}} \vec{\mathcal{A}}_{\vec{k}}(t) e^{i\vec{k}\vec{r}}, \tag{1.18}$$

where summation over $\vec{k}$ means summation over $n_i, i = x, y, z$ and $n_i = 0, 1, ...$ being quantum numbers associated to each $\vec{k}$-component: $k_i = 2\pi n_i/L$. Each plane wave component $\vec{\mathcal{A}}_{\vec{k}}$ is perpendicular to its wave vector

$$\vec{k}\vec{\mathcal{A}}_{\vec{k}} = 0, \tag{1.19}$$

i.e., the field is transversal. This can be easy shown by plugging 1.18 into Coulomb gauge condition. From equations 1.17 and 1.18 time-dependent amplitude $\vec{\mathcal{A}}_{\vec{k}}(t)$ reads

$$\vec{\mathcal{A}}_{\vec{k}}(t) = \vec{u}_{\vec{k}}(0)e^{-i\omega t} + \vec{u}^*_{-\vec{k}}(0)e^{i\omega t}. \tag{1.20}$$

As the field is transversal, one can decompose vectors $\vec{u}_{\vec{k}}$ into two orthogonal states of circular polarization forming a right-hand Cartesian basis together with $\vec{k}/|\vec{k}|$

$$\vec{u}_{\vec{k}} = \sum_{s=1}^{2} u_{\vec{k},s}\vec{\epsilon}_s. \tag{1.21}$$

Bearing in mind that $\vec{\epsilon}_s\vec{\epsilon}^*_{s'} = \delta_{s,s'}$ we can express now the vector potential $\vec{A}$ as follows

$$\vec{A}(\vec{r},t) = \frac{1}{\sqrt{\epsilon_0 L^3}} \sum_{\vec{k},s} (u_{\vec{k},s}(t)\vec{\epsilon}_s e^{i\vec{k}\vec{r}} + u^*_{\vec{k},s}(t)\vec{\epsilon}^*_s e^{-i\vec{k}\vec{r}}). \tag{1.22}$$

where $u_{\vec{k},s}(t) = u_{\vec{k},s}(0)e^{-i\omega_{\vec{k},s}t}$. Using expressions 1.11 and 1.12 we expand the electric and magnetic fields in terms of new amplitudes $u_{\vec{k},s}(t)$

$$\vec{E}(\vec{r},t) = \frac{1}{\sqrt{\varepsilon_0 L^3}} \sum_{\vec{k},s} i\omega_{\vec{k},s}(u_{\vec{k},s}(t)\vec{\epsilon}_s e^{i\vec{k}\vec{r}} + h.c), \tag{1.23}$$

$$\vec{B}(\vec{r},t) = \frac{1}{\sqrt{\varepsilon_0 L^3}} \sum_{\vec{k},s} (u_{\vec{k},s}(t)(\vec{k}\times\vec{\epsilon}_s) e^{i\vec{k}\vec{r}} + h.c). \tag{1.24}$$

The Hamiltonian of the field from the general expression

$$H = \frac{1}{2}\int_{L^3} (\varepsilon_0 \vec{E}^2(\vec{r},t)) + \frac{1}{\mu_0}\vec{B}^2(\vec{r},t))d^3r. \tag{1.25}$$

takes after some algebra the simple form

$$H = 2\sum_{\vec{k},s} \omega^2_{\vec{k},s}|u_{\vec{k},s}(t)|^2. \tag{1.26}$$

Introducing canonical variables

$$q_{\vec{k},s}(t) = (u_{\vec{k},s}(t) + u^*_{\vec{k},s}(t)) \tag{1.27}$$

$$p_{\vec{k},s}(t) = -i\omega_{\vec{k},s}(u_{\vec{k},s}(t) - u^*_{\vec{k},s}(t)). \tag{1.28}$$

it becomes

$$H = \frac{1}{2}\sum_{\vec{k},s}(p^2_{\vec{k},s}(t) + \omega^2_{\vec{k},s}q^2_{\vec{k},s}(t)). \tag{1.29}$$

The expression 1.29 represents a sum over independent harmonic oscillators each with a wave vector $\vec{k}$ and a polarization s oscillating with frequency $\omega_{\vec{k},s}$.

From this expression the usual canonical quantization procedure consists of introducing commutation relations:

$$[\hat{q}_{\vec{k},s}(t), \hat{p}_{\vec{k\prime},s\prime}(t)] = i\hbar\delta_{\vec{k}\vec{k\prime}}\delta_{s,s\prime}, [\hat{q}_{\vec{k},s}(t), \hat{q}_{\vec{k\prime},s\prime}(t)] = 0, [\hat{p}_{\vec{k},s}(t), \hat{p}_{\vec{k\prime},s\prime}(t)] = 0, \tag{1.30}$$

where operators $\hat{q}$ and $\hat{p}$ are associated to classical variables p and q. From obvious analogy with quantization of harmonic oscillator for which we define annihilation and creation operator in terms of coordinate and momentum operator we proceed by defining $\hat{a}_{\vec{k},s}(t)$ and $\hat{a}^*_{\vec{k},s}(t)$

$$\hat{a}_{\vec{k},s}(t) = \frac{1}{(2\hbar\omega_{\vec{k},s})^{1/2}}(\omega_{\vec{k},s}\hat{q}_{\vec{k},s}(t) + i\hat{p}_{\vec{k},s}(t)), \tag{1.31}$$

$$\hat{a}^\dagger_{\vec{k},s}(t) = \frac{1}{(2\hbar\omega_{\vec{k},s})^{1/2}}(\omega_{\vec{k},s}\hat{q}_{\vec{k},s}(t) - i\hat{p}_{\vec{k},s}(t)). \tag{1.32}$$

Operators $\hat{a}$ and $\hat{a}^\dagger$ are quantum mechanical analogs of the complex amplitudes u and u^* to the factor $(\hbar/2\omega)^{1/2}$. We then write the quantum version of the Hamiltonian 1.29

$$\hat{H} = \sum_{\vec{k},s} \hbar\omega_{\vec{k},s}(\hat{a}^\dagger_{\vec{k},s}(t)\hat{a}_{\vec{k},s}(t) + 1/2). \tag{1.33}$$

The product of annihilation and creation operators $\hat{n}_{\vec{k},s} = \hat{a}^\dagger_{\vec{k},s}\hat{a}_{\vec{k},s}$ gives the number of photons in the mode $(\vec{k}, s)$: $\hat{n}_{\vec{k},s}|n_{\vec{k},s}> = n_{\vec{k},s}|n_{\vec{k},s}>$. As the Hamiltonian 1.30 is a many-body Hamiltonian, the space in which it is acting is given by

$$\prod_{\vec{k},s} |n_{\vec{k},s}> = |n> \tag{1.34}$$

being the direct product of single particle states. The vacuum state is defined as the state without photons in any mode: $|vac\rangle = |0>$. In second quantization electric and magnetic fields become operators $\hat{\vec{E}}(\vec{r}, t)$ and $\hat{\vec{B}}(\vec{r}, t)$ defined in terms of $\hat{a}$ and $\hat{a}^\dagger$ which follows straightforwardly from expressions 1.11,1.12 and 1.22.

Therefore for a cavity of volume L^3 the electric field $\hat{\vec{E}}(\vec{r}, t)$ reads

$$\hat{E}(\vec{r}, t) = \sum_{\vec{k},s}(i\sqrt{\frac{\hbar\omega_{\vec{k},s}}{2\varepsilon_0 L^3}}\hat{a}_{\vec{k},s}(t)f_{\vec{k},s} + h.c.). \tag{1.35}$$

In free space instead of proper functions of our cavity $f_{\vec{k},s}$ whose specific form depends on the cavity geometry, one should put plane waves into above formula. Since the expected value of electric field in vacuum state is zero: $< vac|\hat{\vec{E}}(\vec{r}, t)|vac >= 0$, fluctuations in a single cavity mode described by function $f_{\vec{k},s}$ are:

$$< vac|\hat{\vec{E}}^2(\vec{r}, t)|vac >= \frac{\hbar\omega}{2\varepsilon_0 L^3}|f_{\vec{k},s}|^2. \tag{1.36}$$

they are inversely proportional to quantization volume L^3 and for very small volumes,i.e. strong confinement, they are much more pronounced compared with the fluctuations in free space. The amplitude of these fluctuations E_{cav} being the square root of the latter expression is an important quantity describing interaction of an optical mode with an electric dipole through the relation

$$\Omega_R = \frac{\mu E_{cav}}{\hbar}. \tag{1.37}$$

The relation is valid no matter what is the nature of the electric dipole - it certainly holds for atomic and excitonic dipoles with μ being the dipole matrix element. As the confinement is stronger, vacuum fluctuations E_{cav} increase, resulting in higher values of the coupling Ω_R. It is usually refereed as Rabi frequency - the frequency at which an optical and an atomic/excitonic mode exchange energy thus performing oscillations.

1.3 Strongly coupled excitons and photons: polaritons

1.3.1 Bulk polaritons

Polaritons were theoretically studied for the first time in reference [1] by Hopfield. In this seminal paper, optical properties of excitons in bulk isotropic materials, were analyzed using quantum-electrodynamical approach from which in the second quantization procedure excitons-polaritons appear as normal modes of EM field interacting with polarization induced by excitons. This approach starts with classical Lagrangian density $\mathcal{L}$, classical in the sense that no relativistic effects are present, which takes into account the above-mentioned interaction

$$\mathcal{L} = \mathcal{L}_{exc} + \mathcal{L}_{EM} + \mathcal{L}_{int} \tag{1.38}$$

The first term represents Lagrangian density of free excitons $\mathcal{L}_{exc}$. It originates from an oscillating polarization field $\vec{P}$ induced by excitons due to presence of the electric field $\vec{E}$. The simplest equation for this induced polarization, neglecting damping and spatial dispersion is an equation of driven harmonic oscillator [1]:

$$\frac{\partial^2 \vec{P}}{\partial t^2} + \omega_0^2 \vec{P} = \varepsilon_b \omega_{LT} \omega_0^2 \vec{E}, \tag{1.39}$$

where ω_0 is exciton resonance, ω_{LT} splitting of transverse and longitudinal mode of EM field and ε_b dielectric constant. From here Lagrangian density $\mathcal{L}_{exc}$ in terms of field $\vec{P}$ is

$$\mathcal{L}_{exc} = \frac{1}{2\beta}\frac{1}{\omega_0^2}(\frac{\partial \vec{P}}{\partial t})^2 - \frac{1}{2\beta}\vec{P}^2. \tag{1.40}$$

where parameter β equals $2\varepsilon_b(\omega_{LT}/\omega_0)$. Photon field, vectors $\vec{E}$ and $\vec{B}$, as we have seen, is given in terms of components of the electromagnetic four-potential A^α by expressions 1.11 and 1.12. Plugging those in Lagrangian density of free electromagnetic field 1.10 we obtain

$$\mathcal{L}_{EM} = \frac{\varepsilon_b}{2}(-\frac{\partial \vec{A}}{\partial t} - \nabla\phi)^2 - \frac{1}{2\mu_0}(\nabla \times \vec{A})^2. \tag{1.41}$$

The interaction part $\mathcal{L}_{int}$ comes from coupling of four-current $J^\alpha = (\rho/c, \vec{j})$ due to presence of excitons with the four-potential A^α of electromagnetic field

$$\mathcal{L}_{int} = J_\alpha A^\alpha. \tag{1.42}$$

As ρ describes density of induced charge given by $\rho = -\nabla\vec{P}$ and $\vec{j}$ induced current $\vec{j} = \partial\vec{P}/\partial t$ $\mathcal{L}_{int}$ becomes

$$\mathcal{L}_{int} = \partial\vec{P}/\partial t\vec{A} + (\nabla\vec{P})\phi. \tag{1.43}$$

The same second quantization procedure we performed in previous section leads to operators $\hat{\vec{A}}$ and $\hat{\vec{P}}$ of following form

$$\hat{\vec{A}} = \sum_{\vec{k},s} \sqrt{\frac{\hbar}{2\varepsilon_b V \omega_{\vec{k}}}}(\hat{a}_{\vec{k},s}\vec{\epsilon}_s e^{i\vec{k}\vec{r}} + h.c.), \tag{1.44}$$

$$\hat{\vec{P}} = \sum_{\vec{k},s} \sqrt{\frac{\hbar\omega_0}{2\varepsilon_b V}}(\hat{b}_{\vec{k},s}\vec{\epsilon}_s e^{i\vec{k}\vec{r}} + h.c.), \tag{1.45}$$

with $\hat{a}_{\vec{k},s}$ and $\hat{a}_{\vec{k},s}$ being photon and exciton annihilation operators, respectively. The resulting second quantization Hamiltonian is

$$\hat{H} = \sum_k \frac{\hbar c k}{\sqrt{\varepsilon_b}}(\hat{a}_k^\dagger\hat{a}_k + \frac{1}{2}) + \hbar\omega_k(\hat{b}_k^\dagger\hat{b}_k + \frac{1}{2}) + iG_k(\hat{a}_k + \hat{a}_{-k}^\dagger)(\hat{b}_{-k} - \hat{b}_k^\dagger). \tag{1.46}$$

where summation goes over $k = (s, \vec{k})$. One can include dispersion of excitons by letting $\hbar\omega_k = \hbar\omega_0 + \frac{\hbar^2k^2}{2M}$, with M being exciton mass. The first coefficient G_k describes exciton-photon coupling and in most situations is many times larger than an extra term coming from photon-photon coupling due to the presence of atoms. The latter will therefore be neglected. To find the normal modes we have to diagonalize the Hamiltonian 1.46. To do this we use a transformation of operators in which new operator $\hat{p}_k$ is given as a linear combination

$$\hat{p}_k = X\hat{a}_k + C\hat{b}_k + Y\hat{a}_{-k}^\dagger + Z\hat{b}_{-k}^\dagger. \tag{1.47}$$

New operators $\hat{p}_k$ defined by above Hopfield-Bogoliubov transformation describe the normal modes of the Hamiltonian, called exciton-polaritons. They are a mixture of exciton and photons as it's obvious from the transformation 1.47. Since the normal mode operator $\hat{p}_k$ satisfies eigen-problem

$$[\hat{p}_k, \hat{H}] = E_k\hat{p}_k. \tag{1.48}$$

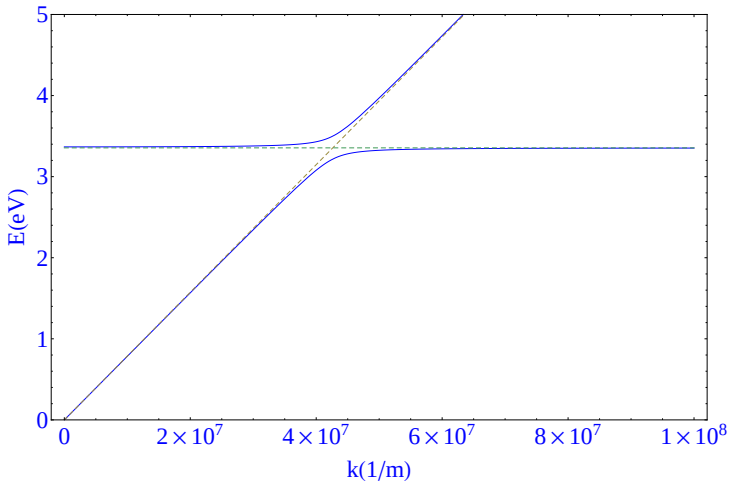

Figure 1.3 | Dispersion of transverse polaritons in an infinite crystal (solid lines). Dashed curves represent uncoupled photon and exciton dispersions (green and gray line, respectively). Parameters used in the plot correspond to bulk ZnO values.

we find the dispersion relation

$$E^4(k) - \hbar^2(v^2k^2 + \omega_k^2 + 2\omega_{LT}\omega_0)E^2(k) + \hbar^4v^2k^2\omega_k^2 = 0, \tag{1.49}$$

with $v = c/\sqrt{\varepsilon_b}$. On the Figure 1.3 is shown the dispersion in an ideal bulk material. There are two eigenmodes - upper and lower polariton, as follows from 1.49. Strong interaction between photons and excitons manifests itself in the repulsion of polariton eigenmodes, so called anti-crossing. In the absence of coupling in this point the dispersion is degenerate and exciton and photon mode cross each other. This degeneracy is removed by strong coupling.

Due to the momentum conservation in an infinite structure each photon oscillator of wave vector $\vec{k}$ couples to one exciton oscillator of the same wave vector. The energy exchanges between them at Rabi frequency Ω_R. The result of above concept is a simple model of two coupled harmonic oscillators, which can be generalized to include the damping of exciton and photon modes. Strong coupling regime (polariton picture) is valid as far as energy of coupling,e.g. Rabi frequency Ω_R exceeds the dumping of both modes. Otherwise the system is in the regime of weak coupling, which is not the subject of this thesis.

1.3.2 Cavity polaritons

In confined structures 1.6, the momentum conservation is relaxed in directions in which confinement is imposed. An exciton oscillator with wave vector $\vec{k} = (k_\parallel, k_z)$, where $k_\parallel$ is in-plane component and $k_z = n_z\pi/L$ is the component along the growth direction of

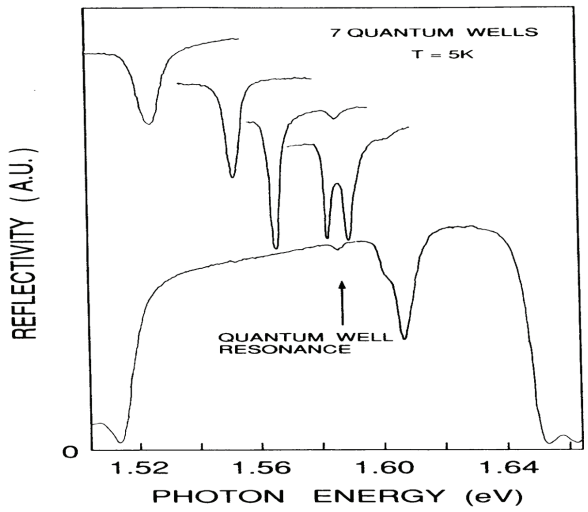

Figure 1.4 | Reflectivity of a microcavity with seven GaAlAs QWs observed in the experiment of reference [4].Different curves stand for different values of exciton-photon detuning.

microcavity of length L, couples to the photon of the same in-plane wave vector because of the absence of in-plane confinement. In z-direction there is no momentum conservation and exciton couples to photons of different k_z. Energy exchange between one exciton mode and set of photon modes therefore occurs at different Rabi frequencies which leads, for a weak coupling, to enhancement of cavity emission (Purcell effect). Instead of a simple modification of emission, in the case of strong coupling a reversible exchange between exciton and photons modes is established. Due to this, cavity line-width becomes smaller what was experimentally observed in [4] inspecting reflectivity of cavity containing several GaAlAs QWs. The dip in the reflectivity (the Fig. 1.4) is a clear sign of strong coupling and of the establishing of polariton regime when the energy is rather transferred between exciton and photon components than radiated from the cavity. A multiple QW cavity structure was used in this experiment to enhance the Rabi oscillations by factor $\sqrt{N}$ with respect to Rabi frequency of a single QW structure.

Differently from the bulk case where the photon dispersion is a linear function of $3D$ wave-vector k, photon dispersion in microcavities is rather a function of $2D$ in-plane wave vector $k_\parallel$. Taking into account the decay rate Γ_C, in first approximation it reads

$$\hbar\omega_C(k_\parallel) = E_C(k_\parallel = 0) + \frac{\hbar k_\parallel^2}{2m_{ph}} - \frac{i\hbar}{2}\Gamma_C(k_\parallel). \tag{1.50}$$

where we associate the mass $m_{ph} = h\sqrt(\varepsilon_b)n_z/(cL)$ to photon of quantum number n_z in microcavity of length L and background dielectric constant ε_b. Dispersion law 1.50 has the same form as dispersion of electrons in effective mass approximation. This inspires writing of an equation analogous to Schrödinger equation for photons of "mass" m_{ph}.

$2D$ dispersion of excitons with decay rate Γ_X is

$$\hbar\omega_X(k_\parallel) = E_X(k_\parallel = 0) + \frac{\hbar k_\parallel^2}{2M} - \frac{i\hbar}{2}\Gamma_X(k_\parallel). \tag{1.51}$$

The interaction term of the bulk Hamiltonian 1.46 using rotating-wave approximation ($E_C - E_X << E_C + E_X$), which neglects the products of only annihilation or only creation operators of exciton and photon, becomes in microcavity case

$$\hat{H}_{int} = \sum_{k_\parallel} i\hbar\Omega_R(\hat{a}^\dagger_{k_\parallel}\hat{b}_{k_\parallel} - \hat{a}_{k_\parallel}\hat{b}^\dagger_{k_\parallel}) \tag{1.52}$$

where coupling Ω_R is given by

$$\Omega_R(k_\parallel) = \frac{\mu}{2\pi a_B^{2D}}\sqrt{\frac{E_X(k_\parallel)}{\varepsilon_B L}} \tag{1.53}$$

and μ is exciton dipole. Solving the eigenvalue problem of this Hamiltonian we find the eigenvalues

$$E_{+(-)}(k_\parallel) = \frac{E_C(k_\parallel) + E_X(k_\parallel)}{2} \pm \frac{1}{2}\sqrt{(E_C(k_\parallel) - E_X(k_\parallel)^2 + 4\hbar\Omega_R(k_\parallel)^2} \tag{1.54}$$

and eigen-vectors

$$v_+(k_\parallel) = \begin{pmatrix} X_+(k_\parallel) \\ C_+(k_\parallel) \end{pmatrix}, v_-(k_\parallel) = \begin{pmatrix} C_+(k_\parallel) \\ -X_+(k_\parallel) \end{pmatrix} \tag{1.55}$$

which corresponds to the upper$(+)$ and lower $(-)$ polariton mode. Hopfield's coefficients $X_+(k_\parallel)$ and $C_+(k_\parallel)$ satisfying $|X_+(k_\parallel)|^2 + |C_+(k_\parallel)|^2 = 1$, are exciton and photon fraction in the mixed polariton state. They are

$$X_+(k_\parallel) = \frac{E_+(k_\parallel) - E_-(k_\parallel)}{\sqrt{\hbar^2\Omega_R(k_\parallel)^2 + (E_+(k_\parallel) - E_-(k_\parallel))^2}}, \tag{1.56}$$

$$C_+(k_\parallel) = \frac{\hbar\Omega_R(k_\parallel)}{\sqrt{\hbar^2\Omega(k_\parallel)^2 + (E_+(k_\parallel) - E_-(k_\parallel))^2}} \tag{1.57}$$

Linear transformation defined on the exciton and photon operators similar to those of the bulk case 1.47

$$\hat{p}_+(k_\parallel) = X_+(k_\parallel)\hat{a}(k_\parallel) + C_+(k_\parallel)\hat{b}(k_\parallel) \tag{1.58}$$

diagonalizes the Hamiltonian written on exciton and photon basis giving the dispersion relation 1.54 we have obtained. The former reads

$$\hat{H}(k_\parallel) = \sum_{k_\parallel} E_+(k_\parallel)\hat{p}^\dagger_+(k_\parallel)\hat{p}_+(k_\parallel) + E_-(k_\parallel)\hat{p}^\dagger_-(k_\parallel)\hat{p}_-(k_\parallel). \tag{1.59}$$

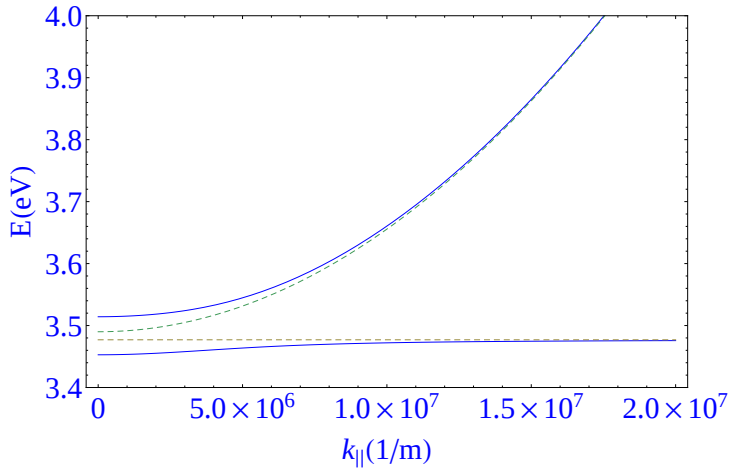

Figure 1.5 | Dispersion of exciton-polaritons in microcavity with GaN QW at zero detuning and $\Omega_R = 30meV$.

Figure 1.5 shows theoretically calculated polariton dispersion for a GaN based microcavity. In vicinity of $k_{\|} = 0$ we can use effective mass approximation to obtain the polariton mass

$$m_{+,-} = \hbar^2 (\frac{\partial^2 E_{+,-}(k_{\|})}{\partial {k_{\|}}^2})^{-1}. \tag{1.60}$$

At resonance $m_+ = m_- \simeq 2m_{ph}$, which is extremely small: about five orders of magnitude smaller than the exciton mass. An important consequence of this ultra small mass is that polaritons efficiently average out the random potential, thus having smaller line-widths [17] than bare excitons and photons.

1.3.3 Polariton-polariton interaction in microcavities

It has been pointed out that polaritons are quasi-particles formed by photons and excitons which are itself composite particles. Experimentally it is known that excitons show bosonic behavior up to high densities [18], though there are some theoretical works [19] putting in question the treatment of excitons like bosons. Nevertheless, based on the first heuristical argument there exists an agreement that (at least at not very high densities) they can be considered like pure bosons obeying usual bosonic commutation relation

$$[\hat{b}_k, \hat{b}^{\dagger}_{k'}] = \delta_{k,k'} \tag{1.61}$$

(we condense the subscript $\|$ in k to shorten the notation). Polariton-polariton interactions is due to the mutual interaction of excitons. Neglecting the spin degree of freedom it is

$$\hat{H}_{int} = \hat{H}_{exc-exc} + \hat{H}_{sat}, \tag{1.62}$$

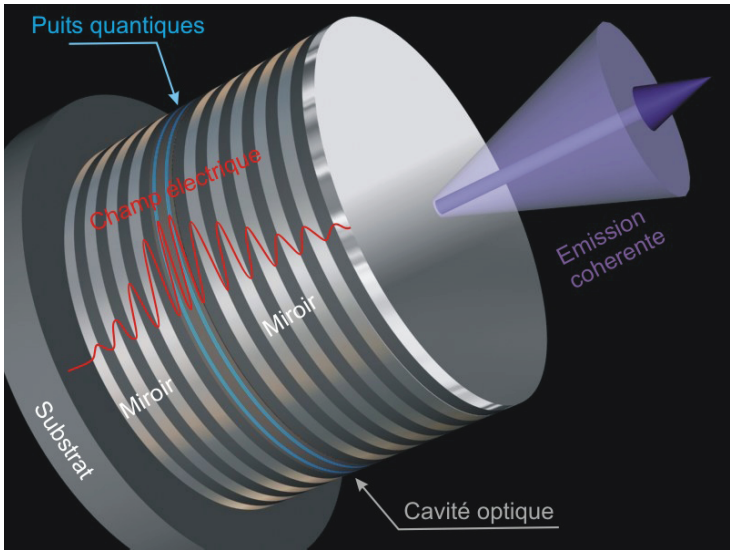

Figure 1.6 | A sketch of a typical microcavity (from private communication with Dr. Dmitry Solnyshkov). An semiconductor QW is embedded between the Bragg mirrors in the anti-nodes of the cavity field providing an efficient overlap of exciton and photon

where

$$\hat{H}_{exc-exc} = \sum_{k,k',q} v_{exc-exc}(k,k',q)\hat{b}^{\dagger}_{k+q}\hat{b}^{\dagger}_{k'-q}\hat{b}_{k'}\hat{b}_{k}, \tag{1.63}$$

is the term including exciton-exciton scattering due Coulomb interaction and Pauli exclusion principle in which two excitons exchange momentum $\hbar q$ and

$$\hat{H}_{sat} = \sum_{k,k',q} v_{sat}(k,k',q)\hat{a}^{\dagger}_{k+q}\hat{b}^{\dagger}_{k'-q}\hat{b}_{k'}\hat{b}_{k}, \tag{1.64}$$

is the saturation term coming only from Pauli exclusion. It is a process in which the scattering of two excitons of momenta $\hbar k, \hbar k'$ produce a photon with momentum $\hbar(k+q)$ and an exciton of momentum $\hbar(k'-q)$. The first term 1.63 is always positive referring to repulsive interaction between excitons of the same spin. Interaction of opposite spins is an open question [20, 21] although, it is usually considered to be much smaller than those of the same spins.

Contrary to this, the sign of interaction of the excitons with the photon field in H_{sat} is always negative. The exact calculation of matrix elements $v_{exc-exc}$ and v_{sat} determining the magnitudes of two interactions is a cumbersome task and not entering in details we will use the result obtained in [22, 23]. The matrix elements $v_{exc-exc}(k,k',q)$ and $v_{sat}(k,k',q)$ in zero-momentum limit read

$$v_{exc-exc} = \frac{3E_b(a_B^{2D})^2}{S}, \tag{1.65}$$

$$v_{sat} = -\frac{\hbar\Omega_R}{n_{sat}S}, \tag{1.66}$$

where S is the quantization surface and n_{sat} is the so-called saturation density. In mean-field approximation $\hat{b}_k^\dagger \hat{b}_k' \sim \delta_{k,k\prime} n_k^{exc}$, where n_k^{exc} is the exciton density in the state k thus giving for $\hat{H}_{sat}$

$$\hat{H}_{sat} \sim -\sum_k \frac{n^{exc}}{n^{sat}S}\hbar\Omega_R(\hat{a}_k^\dagger \hat{b}_k + h.c.), \tag{1.67}$$

which in fact reduces linear exciton coupling $\hbar\Omega_R$, since exactly at $n^{exc} = n_{sat}$ exciton-photon coupling vanishes ($n_{sat} \sim (a_B^{2D})^{-2}$).

Starting from the interaction written on the exciton-photon basis one may obtain an effective polariton-polariton interaction Hamiltonian. This prescription is obtained as previously by linear Hopfield transformation. Restricting ourselves to only the lower polariton branch, as population of upper polaritons is in most of situations very small, polariton-polariton interaction in the new basis takes the form

$$\hat{H}_{int}^+ = \frac{1}{2}\sum_{k,k\prime,q} V(k,k\prime,q)\hat{p}_{k+q}^\dagger \hat{p}_{k\prime-q}^\dagger \hat{p}_{k\prime}\hat{p}_k. \tag{1.68}$$

where the effective interaction term now includes both contributions. The matrix element is

$$V(k,k\prime,q) = v_{exc-exc}X_{k+q}^- X_{k\prime-q}^- X_k^- X_{k\prime}^- + v_{sat}X_{k\prime-q}^-(C_{k+q}^- X_k^- + X_{k+q}^- C_k^-)X_k^+. \tag{1.69}$$

with X_k^- and C_k^- being the exciton and photon fraction defined by expressions 1.57 and 1.57. In what follows we will neglect saturation term assuming that $n_{sat}^+ >> n^{exc,+}$. Then all polariton-polariton interactions come from the interaction of excitons with excitons. It is why in polariton basis the matrix element for this interaction in exciton-photon basis is multiplied by Hopfield's coefficient X_k^+ which describes the excitonic contribution to polariton state.

1.4 Bose-Einstein condensation

1.4.1 Bose-Einstein condensation of ideal Bose gas

Indistinguishability of quantum mechanical particles reflects the properties of many-particle wave function under permutation symmetry. Interchanging two coordinates in wave function $\psi(r_1, ..., r_N)$ should give the same physical state which differs from the initial one only to a phase factor α [24]

$$\psi(r_1, ..., r_j, ..., r_k, ..., r_N) = \alpha\psi(r_1, ..., r_k, ..., r_j, ..., r_N) = \alpha^2\psi(r_1, ..., r_j, ..., r_k, ..., r_N). \tag{1.70}$$

It is obvious that $\alpha = \pm 1$. The particles which wave function transforms symmetrically under interchange of coordinates are called bosons ($\alpha = 1$) whereas anti-symmetric wave

function describes fermions ($\alpha = -1$):

$$\psi(r_1, ..., r_j, ..., r_k, ..., r_N) = +\psi(r_1, ..., r_k, ..., r_j, ..., r_N)(bosons), \tag{1.71}$$

$$\psi(r_1, ..., r_j, ..., r_k, ..., r_N) = -\psi(r_1, ..., r_k, ..., r_j, ..., r_N)(fermions). \tag{1.72}$$

For given temperature T bosons obey Bose-Einstein and fermions Fermi-Dirac statistics [25].We write both in the short notation

$$n_i(T) = \frac{1}{\exp\beta(\epsilon_i - \mu) \mp 1} \tag{1.73}$$

where n_i denotes the most probable occupation number in thermodynamic limit ($V \to \infty$,$N \to \infty$).The factor $\beta = 1/kT$ and $-(+)$ stands for bosons (fermions). ϵ_i are the eigen-values of single-particle Hamiltonians and the chemical potential is defined by normalization

$$N = \sum_i n_i(\mu, T) \tag{1.74}$$

fixing the total number of particles N. Satyendra Nath Bose was the first to propose what is now called Bose-Einstein statistics which Einstein used as a photon statistic to explain the Planck distribution. This preceded the famous paper [26] of Einstein on the subject of this section but also the Fermi statistics. Fermions and bosons show quite different properties. For fermions holds the Pauli principle which forbids two identical fermions to occupy the same state. It is clearly seen putting $r_j = r_k$ in equation 1.72. Contrary to fermions, it turns out that bosons have the tendency to fill the same quantum state by condensing in the Bose-Einstein sense.

To see this let's consider non-interacting bosons with dispersion $\epsilon_k = \hbar^2 k^2/2m$ and change summation over i in 1.74 by k

$$N = \sum_k \frac{1}{\exp\beta(\epsilon_k - \mu) - 1}. \tag{1.75}$$

Substituting $x = k/(\sqrt{2m/\beta\hbar^2})$ and taking thermodynamic limit we get expression

$$n\lambda^3 = g_{3/2}(z), \tag{1.76}$$

where $\lambda = \hbar/\sqrt{2\pi mkT}$ is thermal de Broglie wavelength and $z = \exp(\beta\mu)$ is fugacity. The RHS is integral representation of Bose function

$$g_k(z) = \sum_{l=1}^{\infty} z^l/l^k. \tag{1.77}$$

The series 1.77 converge for $z \leq 1$ and is bounded by value $g_{3/2}(z = 1)$

$$g_{3/2}(1) = \sum_{l=1}^{\infty} l^{-3/2} = \zeta(3/2) = 2.612.... \tag{1.78}$$

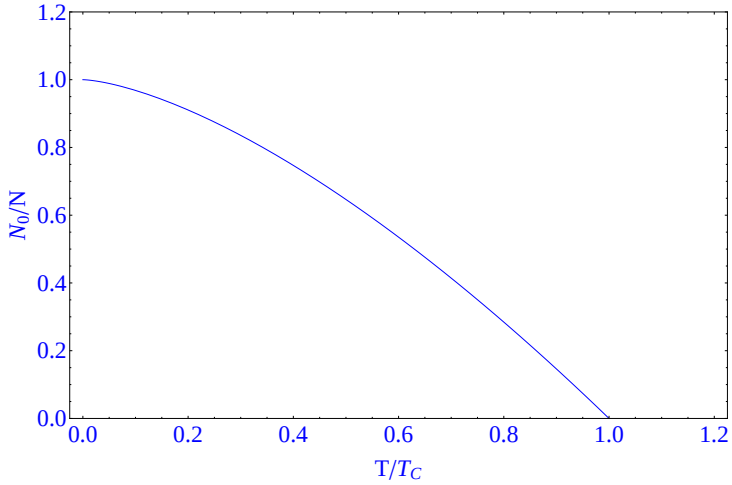

Figure 1.7 | Condensate fraction showing that at $T = T_C$ particles undergo transition to the from Bose gas to BEC condensate state with $k = 0$

The last denotes famous Riemann zeta function $\zeta(z)$. Equation 1.76 has a solution if

$$n\lambda^3 \leq \zeta(3/2). \tag{1.79}$$

Once the condition is fulfilled $n\lambda^3 = \zeta(3/2)$ we can easily imagine a situation when we either increase n or decrease T and by doing this violate the last inequality. This, in fact, does not happen as the expression 1.76 is obtained in thermodynamic limit replacing

$$\frac{1}{V}\sum_k \rightarrow \int \frac{d^3k}{(2\pi)^3} \tag{1.80}$$

in which the term for $k = 0$ vanishes. Removing thermodynamic limit the expression for large but finite volume V reads

$$\frac{N}{V} = \frac{1}{V}\frac{z}{1-z} + \int_k \frac{d^3k}{(2\pi)^3}\frac{1}{z^{-1}\exp{(\beta\frac{\hbar^2k^2}{2m})} - 1}, \tag{1.81}$$

where the first term corresponds to $k = 0$ and the second one for the states with $k \neq 0$. Instead, violating the condition 1.79, particles prefer to condense into $k = 0$ state which thus becomes macroscopically occupied. This is what is called Bose-Einstein condensation. During the process of condensate forming z stays fixed at $z = 1$ and in the limit $V \rightarrow \infty$ the first term of 1.81, being the condensate density $n(k = 0)$ is indeterminate, otherwise for $z \neq 1$ it is zero. This critical point defines the temperature T_C of BEC at a given density n or vice versa:

$$kT_C = \frac{2\pi\hbar^2}{m}(\frac{n}{\zeta(3/2)})^{2/3}, \tag{1.82}$$

$$n_C = \zeta(3/2)(\frac{mkT}{2\pi\hbar^2})^{2/3}. \tag{1.83}$$

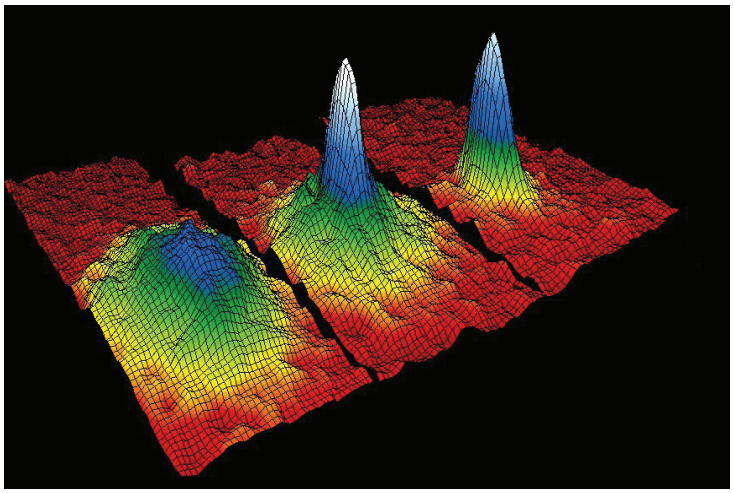

Figure 1.8 | Distribution of particles in the momentum space. Temperatures are 400 nK, 200 nK, and 50nK (from left to right)[5]. Macroscopical occupation occurs for $T < T_C$ (central and right distributions)

Using the definition of critical temperature and relation 1.76 we find the fraction of particles being in Bose-Einstein condensate:

$$\frac{N_0}{N} = (1 - (\frac{T}{T_C})^{3/2}). \tag{1.84}$$

The condensate fraction is zero below T_C. Lowering the temperature, thermal part $1 - N_0/N$ decreases and at $T = 0K$ all particles are forced to condense (the Fig. 1.7). For the first time BEC was observed by E. Cornell,C. Wieman et al. [5] seventy years after Einstein's paper [26]. The experiment consist in cooling rubidium-87 atoms below the critical temperature $T_C = 170nK$. The Figure 1.8 shows the distribution of particles at three different temperatures of this experiment. It's clearly seen that at the temperatures far below the critical one, most of the particles occupy the ground state $k = 0$.

1.4.2 Bose-Einstain condensation in weakly-interacting gases

The previous section was dedicated to BEC in an ideal Bose gas in three dimensions. As we have seen, cavity polaritons are 2D objects. It is interesting to see how BEC depends on the dimensionality of the system in the question. Coming back to expression 1.81, one can easily check that the thermal part which we denote like

$$n_T = \int_k \frac{d^3k}{(2\pi)^3} \frac{1}{z^{-1} \exp{(\beta \frac{\hbar^2 k^2}{2m})} - 1}, \tag{1.85}$$

shows infrared divergence in $1D$ and $2D$, and converges to some definite value n_T^c for 3D in the limit $z = 1$, which we is said to be the fugacity value during occurrence of BEC phase transition. In this manner in three spatial dimensions all particles $N - N_T^c$

at finite temperatures $T < T_C$ are obliged to descent into condensate, as the capability to accommodate new particles in the thermal part is exhausted by reaching n_T^c. This is not true for $1D$ and $2D$ situations - the integral 1.85 is infinite due to contributions at $\vec{k} \approx 0$ and the condensation at finite temperature can't take place. Adding new particles we will increase the density of thermal part but not that of the condensate as in this case n_T is an unbounded function. For one-dimensional Bose gas this holds also at $T = 0$. This is the consequence of one "no-go" theorem [27] under name of Mermin, Wagner, and Hohenberg. It forbids that a continuous symmetry could be spontaneously broken in dimensions less then three. The spontaneous symmetry breaking means that there is some physical observable which was zero before BEC transition and which takes a non-zero value in the condensed phase. This observable is called the order parameter. BEC is a second order phase transition in which at $T = T_C$ $U(1)$ symmetry,representing the phase freedom of normal Bose gas and being continuous, spontaneously disappears at $T = T_c$. BEC formed in this transition fixes its phase to some particular value and following mentioned theorem it is not in principle possible in $1D$ and $2D$. But this restriction refers exclusively to the spontaneous symmetry breaking of a continuous symmetry and not to phase transitions in general.

It is well known that in $2D$ systems another kind of thermodynamical phase transition occurs - Berezinskii-Kosterlitz-Thouless (BKT) phase transition [28] to a superfluid phase. 'Spontaneous' binding of thermally excited vortices of opposite directions establishes at some temperatures $T = T_{BKT}$, while a free vortex could be observed at $T > T_{BKT}$. BKT phase transition is not a second order phase transition - there is not an order parameter vanishing as soon as the last condition is fulfilled. Instead of disappearance of the order parameter the change is more qualitative and one can speak about "quasi-condensate".

In finite systems 1D and 2D, the convergence of the expression 1.85 is recovered. But in a finite system z cannot reach one. This means that the particle number in condensate is not macroscopically but rather significantly larger than the particle number in thermal part.

If we want to consider BEC of polaritons as we have seen before, we have to include polariton-polariton interaction. To do this we introduce one-body density matrix

$$n(\vec{r}, \vec{r'}) =< \hat{\psi}^\dagger(\vec{r})\hat{\psi}(\vec{r'}) >, \tag{1.86}$$

where $\hat{\psi}^\dagger(\vec{r}), \hat{\psi}(\vec{r'})$ are creation and annihilation operators of our Bose field satisfying

$$\hat{\psi}(\vec{r}) = \phi_0(\vec{r})\hat{a}_0(\vec{r}) + \sum_i \phi_i(\vec{r})\hat{a}_i(\vec{r}). \tag{1.87}$$

The field operator is expanded over single particle states defined in general case by eigen-problem of density matrix 1.86

$$\int d\vec{r'}\, n(\vec{r}, \vec{r'})\phi_i(\vec{r'}) = N_i\phi_i(\vec{r}). \tag{1.88}$$

The density matrix describes correlations of Bose field in two space points $\vec{r}$ and $\vec{r'}$. Equation 1.87 allows us to write the density matrix in the form

$$n(\vec{r},\vec{r'}) = n_0(\vec{r},\vec{r'}) + \tilde{n}(\vec{r},\vec{r'}) = N_0\phi_0^*(\vec{r})\phi_0(\vec{r'}) + \sum_{i\neq 0} N_i\phi_i^*(\vec{r})\phi_i(\vec{r'}). \tag{1.89}$$

The first term represents occupation of BEC and the second one occupation of thermal reservoir. The density matrix of the latter decays exponentially with distance $s = |r' - r|$ with characteristic length $\lambda_T = \sqrt{2\pi\hbar/mk_BT}$. Correlations are present only on this scale whereas for $s > \lambda_T$ thermal part of the system is uncorrelated, independent of the temperature. However, the density-matrix $n_0(\vec{r},\vec{r'})$ below the critical temperature $T < T_C$ shows finite correlations in the limit $s \to \infty$ contributing to the finite correlations of total density matrix. This should be supported, as its Fourier transform is equal to $\vec{k}$-distribution $n(\vec{k})$, by particle distribution below $T < T_C$ of the form

$$N(\vec{k}) = N_0\delta(\vec{k}) + \tilde{N}(\vec{k}). \tag{1.90}$$

The above distribution recovers the condition of the macroscopical occupation of the ground state for finite systems. Finite correlations in the long-range limit ($s \to \infty$) or off-diagonal long-range is called Penrose-Osanger criterion of BEC [28] which is a well-defined criterion not only in an ideal Bose gas, but also in a weakly interacting nonuniform system. In what follows we will assume that interaction between particles can be characterized by s-wave scattering length a which enables witting the condition of diluteness in the form: $a << n^{1/3}$ and apply Bogoliubov approach. The approximation consists of replacing the creation and annihilation operators, $\hat{a}_0$ and $\hat{a}_0^\dagger$, in Hamiltonian of weakly-interacting bosons

$$\hat{H} = \sum_k E_{\vec{k}}^0 \hat{a}_{\vec{k}}^\dagger \hat{a}_{\vec{k'}} + \frac{g}{2V}\sum_{\vec{k},\vec{k'},\vec{q}} \hat{a}_{\vec{k}+\vec{q}}^\dagger \hat{a}_{\vec{k'}-\vec{q}}^\dagger \hat{a}_{\vec{k}}\hat{a}_{\vec{k'}}. \tag{1.91}$$

by complex numbers

$$\hat{a}_0, \hat{a}_0^\dagger \to \sqrt{N_0}. \tag{1.92}$$

which is applicable always when the density of ground state remains finite and depletion is not very strong $N - N_0 << N$, in thermodynamic limit. The interaction constant $g \approx 4\pi\hbar^2 a/m$. For fixed number of particles number operator $\hat{N}$

$$\hat{N} = \sum_{\vec{k}} \hat{a}_{\vec{k}}^\dagger \hat{a}_{\vec{k}} \approx N_0 + \frac{1}{2}\sum_{\vec{k}\neq 0} (\hat{a}_{\vec{k}}^\dagger \hat{a}_{\vec{k}} + \hat{a}_{-\vec{k}}^\dagger \hat{a}_{-\vec{k}}). \tag{1.93}$$

can be replaced by its eigenvalue N. After some straightforward calculation, which includes keeping the terms of order N and N^2 only, one obtains:

$$\hat{H} \approx \frac{gN^2}{2V} + \frac{1}{2}\sum_{\vec{k}\neq 0} (E_{\vec{k}^0} + ng)(\hat{a}_{\vec{k}}^\dagger \hat{a}_{\vec{k}} + \hat{a}_{-\vec{k}}^\dagger \hat{a}_{-\vec{k}}) + ng(\hat{a}_{\vec{k}}^\dagger \hat{a}_{-\vec{k}}^\dagger + \hat{a}_{\vec{k}}\hat{a}_{-\vec{k}}). \tag{1.94}$$

which is reasonable as has been pointed out in the case of small depletion. Introducing Bogoliubov transformation of operators

$$\hat{a}_{\vec{k}} = u_{\vec{k}}\hat{\alpha}_{\vec{k}} - v_{\vec{k}}\hat{\alpha}^{\dagger}_{-\vec{k}}, \tag{1.95}$$

$$\hat{a}^{\dagger}_{-\vec{k}} = u_{\vec{k}}\hat{\alpha}^{\dagger}_{-\vec{k}} - v_{\vec{k}}\hat{\alpha}_{\vec{k}}, \tag{1.96}$$

where coefficients $u_{\vec{k}}$ and $v_{\vec{k}}$ satisfies

$$v^2_{\vec{k}} = u^2_{\vec{k}} - 1 = \frac{1}{2}(\frac{E^0_{\vec{k}} + ng}{E_{\vec{k}}} - 1) \tag{1.97}$$

the Hamiltonian 1.94 in terms of new quasi-particle operators reads

$$\hat{H} = \frac{1}{2}gn^2V - \frac{1}{2}\sum_{\vec{k}\neq 0}(E^0_{\vec{k}} + ng - E_{\vec{k}}) + \frac{1}{2}\sum_{\vec{k}\neq 0} E_{\vec{k}}(\hat{\alpha}^{\dagger}_{\vec{k}}\hat{\alpha}_{\vec{k}} + \hat{\alpha}^{\dagger}_{-\vec{k}}\hat{\alpha}_{-\vec{k}}), \tag{1.98}$$

where

$$E_{\vec{k}} = \sqrt{(E^0_{\vec{k}})^2 + 2ngE^0_{\vec{k}}}. \tag{1.99}$$

It is the famous Bogoliubov dispersion law of elementary excitations of the system as it refers to states with $\vec{k} \neq 0$. The obtained Hamiltonian makes possible to describe the excited states of an interacting Bose gas like the ones of the non-interacting gas of Bogoliubov quanta. The dispersion law in long-wavelength and short-wavelength limit is

$$E_{\vec{k}} = \begin{cases} c\vec{k} & (\vec{k} \to 0) \\ E^0_{\vec{k}} + gn & (\vec{k} \to \infty) \end{cases} \tag{1.100}$$

The former corresponds to sound waves - phonons with velocity $c = \sqrt{gn/m}$ and the latter gives the dispersion of free particles. Transition from phonon to free particle dispersion occurs when $E^0_{\vec{k}} \approx gn$ defining healing length

$$\xi = \frac{1}{\sqrt{8\pi na}}. \tag{1.101}$$

1.4.3 Bose-Einstain condensation in non-uniform systems

The first observation of the BEC phase transition of Cornell group 1.8 was done for a trapped atoms - an non-uniform system. As in practice this is rather a rule than exception, this section will be dedicated to BEC in non-uniform gases. In the spirit of Bogoliubov approximation we replace the field operator of the spatial coordinate $\vec{r}$ in time instant t with a classical field

$$\hat{\psi}(\vec{r}) = \psi_0(\vec{r}) + \delta\hat{\psi}(\vec{r}). \tag{1.102}$$

In mean-field approximation $\psi_0(\vec{r}) =< \hat{\psi}(\vec{r}) >$ and as $< \delta\hat{\psi}(\vec{r}) >= 0$ we will neglect all terms $\sim< \delta\hat{\psi}(\vec{r}) >$. The wave function $\psi_0(\vec{r})$ plays the role of the condensate order

parameter. For a weakly interacting dilute Bose gas in some external potential $V_{ext}(\vec{r})$ from Hamiltonian 1.91 given in $\vec{k}$-space we can write second quantization Hamiltonian in real space

$$\hat{H} = \int d^3\vec{r}(\frac{\hbar^2}{2m}\nabla\hat{\psi}^\dagger\nabla\hat{\psi} + \hat{\psi}^\dagger V_{ext}(\vec{r})\hat{\psi}) + \int\int d^3\vec{r}d^3\vec{r}'(\hat{\psi}^\dagger\hat{\psi}'^\dagger V(\vec{r}-\vec{r}')\hat{\psi}\hat{\psi}') \qquad (1.103)$$

As interaction is constant in $\vec{k}$-representation: $g = 4\pi\hbar/m$ in r-representation it will have contact interaction $V(r-r') = g\delta(r-r')$ which assumes scattering of hard spheres of the radius a. From the previous Hamiltonian we write an energy functional as follows

$$E = \int d^3\vec{r}(\frac{\hbar^2}{2m}|\nabla\psi_0|^2 + V_{ext}(\vec{r})|\psi_0|^2 + \frac{g}{2}|\psi_0|^4), \qquad (1.104)$$

bearing in mind that we neglected 'fluctuations' by performing the mean-field approximation. Variational procedure with the above energy functional gives an equation for the order parameter

$$i\hbar\frac{\partial}{\partial t}\psi_0(\vec{r},t) = (\frac{\hbar^2\nabla^2}{2m} + V_{ext}(\vec{r}) + g|\psi_0(\vec{r},t)|^2)\psi_0(\vec{r},t). \qquad (1.105)$$

The obtained equation is the famous Gross-Pitaevskii (GP), a non-linear Schrödinger-type equation, with an exception that it is its quantum version (contains $\hbar$) describing one nonclassical quantity - the probability amplitude $\psi_0(\vec{r},t)$. As $\psi_0(\vec{r},t)$ is no more operator but rather a complex number in each $\vec{r}$ and t one has:

$$\psi_0 = |\psi_0|exp(i\chi); \qquad N_0 = |\psi_0|^2; \qquad \vec{v} = \frac{\hbar}{m}\nabla\chi. \qquad (1.106)$$

The last two expressions describe number of particles in BEC (in a dilute system $N_0 \approx N$) and velocity.

The time-dependence of the ground state is given by: $\psi_0(\vec{r},t) = \psi_0(\vec{r})exp(-i\mu t)$, where μ is the chemical potential and GP equation becomes:

$$(\frac{\hbar^2\nabla^2}{2m} + V_{ext}(\vec{r}) - \mu + g|\psi_0(\vec{r})|^2)\psi_0(\vec{r}) = 0 \qquad (1.107)$$

Immamoglu and Ram [6] were first to theoretically consider a polariton BEC in frame of one novel type of laser: polariton laser. Besides the conceptual importance of BEC in a solid state system very small polariton mass opens a way to study BEC at higher temperatures, as the temperature of phase transition T_C is inversely proportional to mass of particles (see expression1.82). The first experimental observation of BEC for microcavity polaritons was reported in 2006 [29]. Room-temperature polariton laser has been proposed in 2002 by Malpuech et al. [7].

An important characteristic of polaritons it is their finite-life time. Polaritons in lower dispersion branch in the $\vec{k}_\parallel = 0$ state have the life time much shorter than in excited

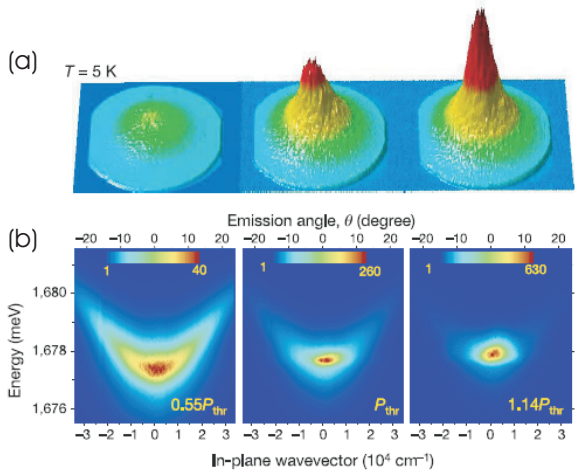

Figure 1.9 | Bose-Einstein condensation of microcavity polaritons [29]: (a) Emission pattern vs excitation powers at 5K (form the left to the right). (b) Energy resolved spectra of panel (a)

state, as the life-time is proportional to photon fraction which we have seen to decrease with $\vec{k}_{\|}$. Then, if polariton population is is created somewhere on the lower polariton branch $\vec{k}_{\|} \neq 0$, one should have efficient relaxation mechanisms in order to thermalize and reach a macroscopical occupation of ground state forming BEC. More details on this interesting question concerning quantum kinetics and thermodynamics of polaritons can be found in ref. [30].

1.5 Pseudo-spin of exciton-polaritons

In section 1.1 on excitons and quantum confinement, we have seen that a heavy exciton is composed of an electron having a one half spin and a heavy hole state which due orbital angular momentum $L = 1$ makes total angular momentum $J = 3/2$. The operator of total angular momentum along quantization axis (growth axis)for excitons is thus given by

$$\hat{J}_z^{exc} = (s_z^h + l_z^h)\hat{\sigma}_z \otimes \hat{I} + \hat{I} \otimes s_z^e \hat{\sigma}_z. \tag{1.108}$$

$\hat{I}$ is 2×2 unity matrix and $\hat{\sigma}_z$ z-Pauli matrix. For $j_z^h = j_z^{hh} = s_z^{hh} + l_z^{hh} = 3/2$ and $s_z^e = 1/2$ the z-component of total angular momentum operator for a heavy hole exciton is

$$\hat{J}_z^{exc} = \begin{bmatrix} 2 & 0 & 0 & 0 \\ 0 & -1 & 0 & 0 \\ 0 & 0 & 1 & 0 \\ 0 & 0 & 0 & -2 \end{bmatrix}. \tag{1.109}$$

We are interested in only heavy hole excitons only as in confined system they form ground state, being lower in energy than light hole excitons. In bulk samples at $\vec{k} = 0$ the light and heavy hole excitons are degenerate (Kramer's degeneracy) due to possession of the center of inversion, as there is no confinement (pg. 52-57 of ref. [13]).

The operator 1.109 has eigenvalues $J_z^{exc} = \pm 1$ called bright and $J_z^{exc} = \pm 2$ called dark excitons. The former are dark states because they cannot be optically excited like bright excitons. During the process of absorption of a photon by an exciton, the spin is conserved as it was shown in ref. [31]. Thus, only bright excitons having $J_z^{exc} = \pm 1$ can be excited by photons, as helicity (spin) of photon is either $+1$ or -1. It can be understood as eigenvalues of operator

$$\hat{S} = \begin{bmatrix} 0 & -i \\ i & 0 \end{bmatrix} \tag{1.110}$$

with eigenvectors

$$|R>= \frac{1}{\sqrt{2}} \begin{pmatrix} 1 \\ i \end{pmatrix} \qquad and \qquad |L>= \frac{1}{\sqrt{2}} \begin{pmatrix} 1 \\ -i \end{pmatrix}, \tag{1.111}$$

corresponding to right and to left circularly polarized photon. All other states can be described as some linear combination of basis vectors $|R>, |L>$. For example, x and y linearly-polarized light can be expressed in this basis by combinations

$$\begin{pmatrix} 1 \\ 0 \end{pmatrix} = |R> + |L> \qquad and \qquad \begin{pmatrix} 0 \\ 1 \end{pmatrix} = |R> - |L>, \tag{1.112}$$

for x and y polarization, respectively. The state is in general elliptically polarized: $a_R|R> + a_L|L>$, where $a_R \neq a_L$. As dark states are optically inactive (at least in most of the situations of our interest), we will neglect them and treat cavity polaritons as effective two-level system using the pseudospin formalism. For this, let's consider a quasi-monochromatic wave propagating in z-plane with wave vector $\vec{k}$ and whose x and y components are given by

$$E_x^k(t) = E_{x0}^k(t) e^{i(kz - \omega t + \alpha_x(t))} \qquad and \qquad E_y^k(t) = E_{y0}^k(t) e^{i(kz - \omega t + \alpha_y(t))} \tag{1.113}$$

write the coherence matrix

$$\hat{\rho_k} = \begin{bmatrix} < E_x^{k,*}(t) E_x^k(t) > & < E_x^{k,*}(t) E_y^k(t) > \\ < E_y^{k,*}(t) E_x^k(t) > & < E_y^{k,*}(t) E_y^k(t) > \end{bmatrix}. \tag{1.114}$$

The pseudospin components are directly related to Stokes parameters defined by

$$S_0^k =< (E_{x0}^k)^2 > + < (E_{y0}^k)^2 >, \tag{1.115}$$

$$S_x^k = 2 < E_{x0}^k E_{y0}^k cos\Delta(t) >, \tag{1.116}$$

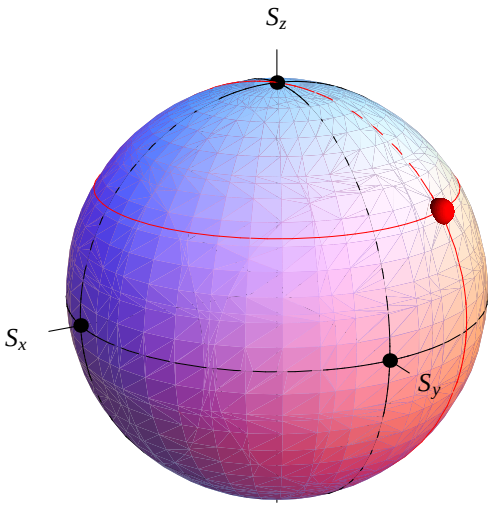

Figure 1.10 | Poincaré sphere [32]. Red point represents an elliptically polarized state

$$S_y^k = 2 < E_{x0}^k E_{y0}^k sin\Delta(t) >, \tag{1.117}$$

$$S_z^k =< (E_{x0}^k)^2 > - < (E_{y0}^k)^2 >, \tag{1.118}$$

where $\Delta(t) = \alpha_x(t) - \alpha_y(t)$. The matrix 1.114 can be write in terms of Stokes parameters and reads

$$\hat{\rho}_k = \frac{1}{2} \sum_{i=0,x,y,z} S_i^k \hat{\sigma}_i, \tag{1.119}$$

where $\hat{\sigma}_0$ is unit matrix and $\hat{\sigma}_x, \hat{\sigma}_y$ and $\hat{\sigma}_z$ are usual Pauli matrices. From non-negativity of 1.119 one has

$$(S_0^k)^2 \leq (S_x^k)^2 + (S_y^k)^2 + (S_z^k)^2. \tag{1.120}$$

The last expression defines a sphere in Stokes parameter space (S_x, S_y, S_z). The inequality holds in the case of partial polarization. This sphere is known as Poincaré sphere. The states with pseudospin $S_z = \pm 1$ correspond to right- or left-circular polarization. The states with $S_x = \pm 1$ correspond to x- and y-linear polarization, while the states $S_y = \pm 1$ correspond to diagonal linear polarization. Other points on the pseudospin sphere describe the general case of elliptical polarization (shown on the Fig. 1.10).

Degree of polarization in the case of partial polarization is

$$P = \frac{\sqrt{S_x^2 + S_y^2 + S_z^2}}{S_0}, \tag{1.121}$$

and $0 \leq P \leq 1$.

1.6 Conclusions

In Chapter 1 we have introduced the basic concept and mathematical apparatus of the exciton-polariton theory. We have discussed the effect of strong and week confinement in different low-dimensional structures, namely quantum dots, quantum wires, and microcavities. The quantization procedure for electromagnetic field and light-matter coupling have been revisited in bulks and confined systems. We detailed on BEC in ideal systems and represented the Bogoliubov theory of weakly interacting nonuniform Bose gas. The accent have been given on the case of exciton-polaritons. Pseudospin formalism has been introduced.

Chapter 2

Exciton-polaritons in wires

In this Chapiter we will focus on the strong coupling in regime in (micro/nano)-wires. In the first part of this chapter we will analyze the wires without taking into account the frequency-dependent optical respones of particular materials [33]. We will be more interested in general properties like energy and line-width dispersion in these quasi-1D structures. Particular attention will be given to cylindrical and hexagonal wires, first, as a simple theoretical model and second, as the usual geometry of Wurzite structures.

In the second part of this chapter we will concentrate on the ZnO microwires. The work presented in Thesis has grown from the close collaboration with the Grenoble group. We will model a PL (photoluminescence) spectra obtained for this type of wires, and some comment on its linewidths will be given. Very high Rabi splitting measured in experiment is reproduced by our theory, as well as small line-width of polariton modes at room-temperature.

Contents

2.1 Introduction

Nano-wires are the objects with cross-section dimension a reduced to nanoscale values, several orders of magnitude smaller than their length L. The dynamics along wire axis can be decoupled from the transverse one in case when $L >> a$ and the system can be treated as quasi one-dimensional. Low dimensional systems in general reveal novel phenomena and are excellent candidates for applications in new technologies. NWs could be used in communications [34], quantum computation [35], or biological sensors [36].

In the last years, significant progress has been achieved in the growth of semiconductor NWs. Interesting novel optical effects have been reported for such structures, like ultraviolet lasing under optical pumping in ZnO NWs [37] and very recently, polaritonic effects: $1D$ exciton-polaritons [38] appear due to the strong coupling of excitons with photonic whispering gallery modes (WGMs) [39]. These modes owe the name to their similarity with acoustic resonances in real galleries. They propagate in the NW's cross-section and due to azimuthal momentum undergo multiple internal reflections. The number of these reflections can be very high, resulting in a high quality factor.

The problem of resonant mode frequencies and their life-time in dielectric resonators has been studied for the cylindrical and hexagonal cross-sections in mesoscopic (large ka) [40] and microscopic (small ka) [41] regimes; where k is the wave vector of the incident light. NWs with cylindrical cross-sections are very well studied theoretically in the isotropic case, being a textbook subject [42]. On the other hand, discrete cross-sections symmetries are much less studied whereas they are of particular interest as real structures often have polygonal cross-sections. Wurtzite or diamond crystals (like ZnO or GaN) generally form hexagonal NWs, but rectangular and triangular forms are also possible [**?**].

A remaining theoretical task in these systems with discrete symmetry cross-sections is to calculate energy dispersion of WGMs (dependence of their energy versus the axial wave vector), as well as their linewidth dispersion. The impact of the anisotropy in dielectric response of wurtzite materials on the polarization eigenstates of the WGMs, has also not been addressed so far. On the other hand, it is well known that semiconductors with wurtzite structure possess birefringent optical anisotropy [**?**]. NWs fabricated from such materials have directionally-dependent dielectric response characterized by two refractive indexes - along the axis of anisotropy n_z and perpendicular to it n_r. Another source of birefringence $\delta n = n_z - n_r$ comes from axial variation of the NW radius due to inevitable growth imperfections.

In this paper, we determine the optical eigenmodes of NWs of various cross-sections, considering both isotropic and anisotropic materials. In the case of circular cross-section, the solutions are cylindrical harmonics of particular azimuthal quantum number m. For arbitrary discrete geometries, an appropriate linear combination of cylindrical harmonics

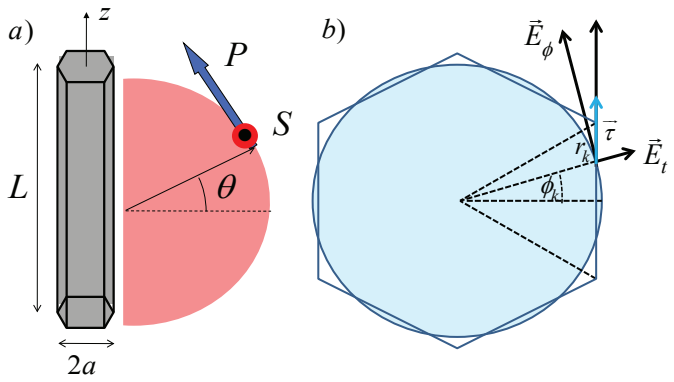

Figure 2.1 | *a*) Hexagonal cylinder of finite height L and with a radius a of its circum-circle. The arrows show the plane of S and P polarized light, θ is the angle of incidence. *b*) Tangential component of the electric field on the surface of the hexagon at the point (r_k, ϕ_k).

is used to fulfill the boundary conditions for tangential electric and magnetic fields on the NW surface. The energy and linewidth dispersions are calculated using this model in an anisotropic medium for the first time, to the best of our knowledge. Polarization and field distribution of the modes versus the angle of incident light (longitudinal wave vector) are also the novelties comparing to the previous works [40, 41].

In the case of a birefringent media, $k_z = 0$ WGMs are either transverse electric (TE) or transverse magnetic (TM) polarized. For the others longitudinal wave vectors, strong mixing of polarization occurs in both isotropic and anisotropic NWs leading to formation of hybrid modes - EH and HE, depending on whether the electric or magnetic field dominates in z-direction. Nevertheless, in this paper we will use the notation TE for the former and TM for the later.

2.2 Cylindrical and hexagonal wires

2.2.1 Mode symmetries

We consider an infinitely long wire with its main axis along the z-direction and having either circular or polygonal cross-section. The Fig. 2.1(a) shows a finite length hexagonal cross-section wire. The presence of translational symmetry along the z-direction imposes an additional factor in the wave functions having the phase form $e^{ik_z z}$. k_z is a good quantum number taking any real value for an infinitely long wire.

The axial symmetry of regular polygons are n-fold rotations C_n, where n is the number of polygon sides. For a circular cross-section $n = \infty$, which corresponds to rotations by infinitesimally small angles around the z-axis. The symmetry group C_∞ is continuous and, like in the case of translation, there is a good quantum number $m \in \mathbb{Z}$. Then, φ-dependence of eigenmodes for each m is given by a single angular harmonic $e^{im\varphi}$.

For regular polygons, n is finite: triangle C_3, square C_4, pentagon C_5, hexagon C_6 etc. These systems remain invariant for in-plane rotations by corresponding discrete angles $2\pi m/n$. The existence of the minimal angle of rotation in these symmetries results in finite number of irreducible representations of the group with $m = 0, \pm 1, ..., \pm(n-2)/2, n/2$ (n even) or $m = 0, \pm 1, ..., \pm(n-1)/2$ (n odd) [43]. The transformation properties of higher m-s appear to be equivalent to those of the first "Brillouin's zone" in m-space. The eigenmodes behavior along φ coordinate is no more given by a single angular harmonic, but rather by their linear combination.

Another important class of polygonal cross section symmetries are reflections - vertical mirror symmetries. The hexagon, for example, is unchanged under reflections in the six vertical planes: 3 containing large hexagon diagonals and 3 connecting the centers of the opposite sides. These operations $\sigma_{d,i}$ and $\sigma_{v,i}$ transform in-plane rotations by angle φ,$R(\varphi)$, into rotations by opposite angles -φ, $R(-\varphi)$: $\sigma_{v,d}R(\varphi)\sigma_{v,d} = R(-\varphi)$. An important physical consequence is the equivalence of m and $-m$. The whole symmetry group describing the axial symmetry of polygonal cross-section NWs containing both n-fold rotations and mirror reflections is denoted with C_{nv}.

The electric $\vec{E} = (E_r, E_\varphi, E_z)$ and magnetic field $\vec{H} = (H_r, H_\varphi, H_z)$ transform differently under reflections. The electric field is a polar (ordinary) vector and magnetic field, being the cross-product $\vec{H} = (1/\mu)\vec{\nabla} \times \vec{A}$, is a pseudovector. Reflections change an eigenmode $(E_r, H_r, E_\varphi, H_\varphi, E_z, H_z)$ to $(E_r, -H_r, -E_\varphi, H_\varphi, E_z, -H_z)$. It is interesting to see how the usual TE and TM eigenmodes for $k_z = 0$ are modified under reflection. TE modes transform from (E_r, E_φ, H_z) to $(E_r, -E_\varphi, -H_z)$, i.e. their parity is opposite to that of the scalar function H_z. TM modes transform from (H_r, H_φ, E_z) to $(-H_r, H_\varphi, E_z)$ after reflection, preserving the parity of the scalar function E_z.

2.2.2 Formalism

We start with the Maxwell's equations written in the frequency domain

$$\nabla \times \vec{H}(\vec{r}, \omega) = -i\frac{\omega}{c}\vec{D}(\vec{r}, \omega) \tag{2.1}$$

$$\nabla \times \vec{E}(\vec{r}, \omega) = i\frac{\omega}{c}\vec{B}(\vec{r}, \omega) \tag{2.2}$$

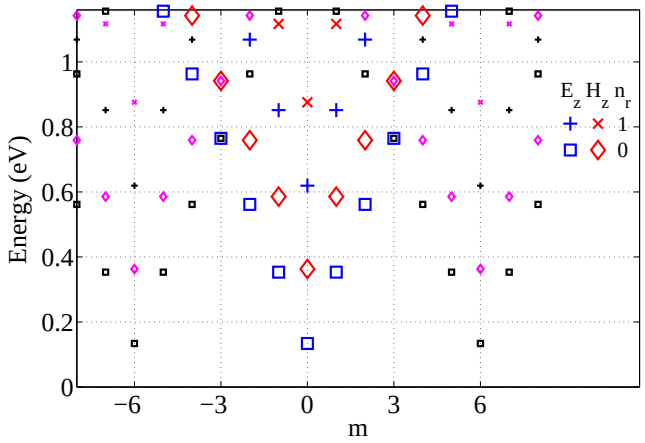

Figure 2.2 | Modes of a cylindrical cross-section NWs versus the angular momentum m (large symbols). The small symbols represent the perturbations of the cylindrical modes due to the imposed hexagonal symmetry.

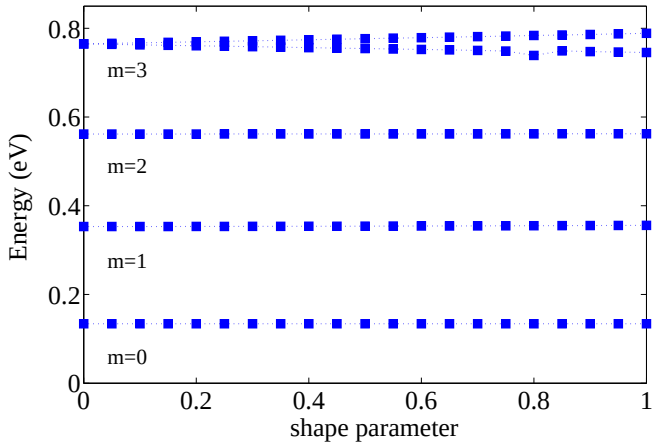

Figure 2.3 | Cylindrical mode evolution versus the shape parameter x which varies from 0 for cylinder to 1 for hexagonal wire.

$$\nabla \cdot \vec{D}(\vec{r},\omega) = 0 \tag{2.3}$$

$$\nabla \cdot \vec{B}(\vec{r},\omega) = 0. \tag{2.4}$$

Taking the curl of the second equation and using $\vec{B}(\vec{r},\omega) = \mu\vec{H}(\vec{r},\omega)$ from Eq.(2.1) follows the wave equation

$$\nabla \times \nabla \times \vec{E}(\vec{r},\omega) - \frac{\omega^2}{c^2}\mu\vec{D}(\vec{r},\omega) = 0. \tag{2.5}$$

Displacement field is given by $\vec{D}(\vec{r},\omega) = \varepsilon\vec{E}(\vec{r},\omega)$, and we consider anisotropic permittivity ε given by tensor $\varepsilon = diag(\varepsilon_r, \varepsilon_r, \varepsilon_z)$, where ε_r and ε_z are the permittivities in NW's cross-section and along the z-axis, respectively.

The double *curl* of the electric field in Eq.(2.5) can be rewritten as

$$\nabla \times \nabla \times \vec{E} = \nabla \cdot (\nabla \cdot \vec{E}) - \Delta \vec{E}. \tag{2.6}$$

In an isotropic medium Eq.(2.3) gives immediately $\nabla \cdot \vec{E} = 0$ and Eq.(2.6) reduces to $-\Delta \vec{E}$. In an anisotropic medium, both terms of Eq.(2.6) are in general non-zero. However, one still can decompose the waves into pure TE ones (for which $E_z = 0$ and $\nabla \cdot \vec{E} = \vec{k} \cdot \vec{E} = 0$) and pure TM ones (for which $H_z = 0$ and $\nabla \cdot \vec{E} = \vec{k} \cdot \vec{E} \neq 0$).

Let's now derive the equation for E_z for the TM wave from Eq.(2.6). Using Eq.(2.3) we calculate $\nabla \cdot \vec{E} = \partial E_z / \partial z \, (1 - \varepsilon_z / \varepsilon_r)$ which is non zero in case of TM waves in anisotropic materials. The z-component of Eq.(2.6) reads

$$\nabla \cdot (\nabla \cdot \vec{E})\Big|_z = \frac{\partial^2 E_z}{\partial z^2} \left(1 - \frac{\varepsilon_z}{\varepsilon_r}\right). \tag{2.7}$$

Inserting Eq.(2.7) in the wave equation (2.5) allows us to obtain the equation for E_z for the TM wave:

$$\frac{\partial^2 E_z}{\partial z^2} \left(\frac{\varepsilon_z}{\varepsilon_r} - 1\right) + \Delta E_z + \frac{\omega^2}{c^2} \varepsilon_z E_z = 0. \tag{2.8}$$

The equation for the H_z field for the TE wave has the form of the usual Helmholtz's equation for an isotropic problem:

$$\Delta H_z + \frac{\omega^2}{c^2} \varepsilon_r H_z = 0. \tag{2.9}$$

So far we have considered infinite homogeneous media. The solution for the wires can be obtained by matching the boundary conditions for the bulk waves on the wire surface. These boundary conditions mix bulk TE and TM waves, making decomposition into pure TE and TM modes only possible for $k_z = 0$. Because of the non-separability of TE and TM modes, we have to simultaneously solve Eq.(2.8) and Eq.(2.9). For cylindrical wires, we search for the solution in the form $R_{E,H}(r) e^{i(m\varphi + k_z z - \omega t)}$, as it follows from the section on the mode symmetry. The radial parts $R_{E,H}(r)$ satisfy

$$\frac{d}{dr}\left(r \frac{dR_{E,H}(r)}{dr}\right) + \left(r q_{E,H}^2 - \frac{m^2}{r}\right) R_{E,H}(r) = 0, \tag{2.10}$$

where

$$q_H = q_E (\varepsilon_r / \varepsilon_z)^{1/2} = (\varepsilon_r \omega^2 / c^2 - k_z^2)^{1/2} \tag{2.11}$$

are in plane wave vectors of the magnetic and electric field within the wire. In the isotropic case $q_H = q_E$. Outside the NW, the same equation (2.10) holds for the radial part with $q_{out} = (\varepsilon_{out} \omega^2 / c^2 - k_z^2)^{1/2}$; ε_{out} is the dielectric constant of wire's environment which is assumed to be isotropic.

Eq.(2.10) is a Bessel's differential equation. The solutions inside the wire are linear combinations of Bessel's functions of the first kind $J_m(x)$, whereas propagating solutions outside are linear combinations of Hankel's functions $H_m^1(x)$ of the first kind. Therefore one can look for the solution for the fields inside (E_z^{in},H_z^{in}) and outside (E_z^{out},H_z^{out}) the wire in the following form:

$$E_z^{in} = \sum_m A_m J_m(q_E r)\phi_m; H_z^{in} = \sum_m B_m J_m(q_H r)\phi_m \tag{2.12}$$

$$E_z^{out} = \sum_m C_m H_m^1(q_{out} r)\phi_m; H_z^{out} = \sum_m D_m H_m^1(q_{out} r)\phi_m \tag{2.13}$$

where $\phi_m = \exp(i(m\varphi + k_z z - \omega t))$. The transverse in-plane components of the fields can be deduced from the z-components (Eq.(12) and Eq.(13)) from following equations:

$$q^2 \vec{E}_T = i\frac{\omega}{c}\nabla_T \times \vec{H}_z + ik_z \nabla_T \vec{E}_z, \tag{2.14}$$

$$q^2 \vec{H}_T = -i\frac{\omega}{c}\nabla_T \times \vec{E}_z + ik_z \nabla_T \vec{H}_z, \tag{2.15}$$

where $q = q_{H,E}$ for internal fields and $q = q_{out}$ for external field. Inside the wire we directly find:

$$E_\varphi^{in} = -\sum_m \left(A_m \frac{mk_z}{q_H^2 r} J_m(q_E r) + iB_m \frac{\omega}{cq_H} J_m'(q_H r) \right) \phi_m, \tag{2.16}$$

$$E_r^{in} = \sum_m \left(iA_m \frac{k_z q_E}{q_H^2} J_m'(q_E r) - B_m \frac{m\omega}{cq_H^2 r} J_m(q_H r) \right) \phi_m, \tag{2.17}$$

$$H_\varphi^{in} = \sum_m \left(iA_m \frac{\omega \varepsilon_z}{cq_E} J_m'(q_E r) - B_m \frac{mk_z}{q_H^2 r} J_m(q_H r) \right) \phi_m, \tag{2.18}$$

$$H_r^{in} = \sum_m \left(A_m \frac{m\omega\varepsilon_r}{cq_H^2 r} J_m(q_E r) + iB_m \frac{ik_z}{cq_H} J_m'(q_H r) \right) \phi_m. \tag{2.19}$$

The outside fields read:

$$E_\varphi^{out} = -\sum_m \left(C_m \frac{mk_z}{q_{out}^2 r} H_m^1(q_{out} r) + iD_m \frac{\omega}{cq_{out}} H_m^{1'}(q_{out} r) \right) \phi_m, \tag{2.20}$$

$$E_r^{out} = \sum_m \left(C_m \frac{ik_z}{q_{out}} H_m^{1'}(q_{out} r) - iD_m \frac{m\omega}{cq_{out}^2 r} H_m^1(q_{out} r) \right) \phi_m, \tag{2.21}$$

$$H_\varphi^{out} = \sum_m \left(C_m \frac{\omega\varepsilon_{out}}{cq_{out}} H_m^{1'}(q_{out} r) - iD_m \frac{mk_z}{q_{out}^2 r} H_m^1(q_{out} r) \right) \phi_m, \tag{2.22}$$

$$H_r^{out} = \sum_m \left(C_m \frac{m\omega\varepsilon_{out}}{cq_{out}^2 r} J_m(q_{out}r) + iD_m \frac{k_z}{q_{out}} J_m'(q_{out}r) \right) \phi_m. \tag{2.23}$$

From these expressions one can check that it is not possible to have a pure TE mode putting $A_m = 0$ (no longitudinal electric field $E_z = 0$). For $k_z \neq 0$, the magnetic field is also present in the transverse plane and the last two terms in Eq.(2.18) and Eq.(2.19)) are non-zero. Similar argumentation holds for the existence of a pure TM mode. In the general case of $k_z \neq 0$ a sharp separation of TE and TM modes is no more possible and the modes are mixed.

To calculate the mode dispersion, one needs to write proper boundary conditions for both electric and magnetic fields resulting in a system of equations for the fields amplitudes. The tangential external and internal electric and magnetic fields should match on the wire boundary. If we denote $F_{in,out} = (E_z^{in,out}, E_t^{in,out}, H_z^{in,out}, H_t^{in,out})^T$, boundary conditions are fulfilled if $\delta F = F_{in} - F_{out}$ is zero on the surface of the wire. In the case of cylindrical wires of radius a, the fields for a single angular harmonics are proper solutions, and the last statement is valid for each of them independently. Tangential components on the boundary are φ-field (equations 2.16 and 2.18) and for a chosen m, on the boundary $r = a$, we can write matrix equation $F_m(\omega, k_z; a)X_m = 0$. The vector X_m being a set of partial amplitudes $X_m = (A_m, B_m, C_m, D_m)$ and the matrix $F_m(\omega, k_z; a)$ given by following expression:

$$F_m(\omega, k_z; a) = \begin{bmatrix} J_m(q_E a) & 0 & -H_m^1(q_{out}a) & 0 \\ -\frac{mk_z}{q_H^2 a} J_m(q_E a) & -\frac{i\omega}{cq_H} J_m'(q_H a) & \frac{mk_z}{q_{out}^2 a} H_m^1(q_{out}a) & \frac{i\omega}{cq_{out}} H_m^{1\prime}(q_{out}a) \\ 0 & J_m(q_H a) & 0 & -H_m^1(q_{out}a) \\ \frac{i\omega\varepsilon_z}{cq_E} J_m'(q_E a) & -\frac{mk_z}{q_H^2 a} J_m(q_H a) & -\frac{i\omega\varepsilon_z}{cq_{out}} H_m^{1\prime}(q_{out}a) & \frac{mk_z}{q_{out}^2 a} H_m^1(q_{out}a) \end{bmatrix}. \tag{2.24}$$

Dispersion relation $\omega_m(k_z)$ is calculated from the condition that the determinant of a homogeneous system of equations must be zero in order to have nontrivial solution $X_m \neq 0$. These dispersions can be found by an efficient iterative numerical procedure [**?**], based on the linearization of the matrix $F_m(\omega, k_z; a)$ with respect to ω.

Fig. 5.9 shows (large symbols) the calculated mode energies at $k_z = 0$ for a cylindrical NW. For each angular momentum m, and for each polarization (E_z, H_z), series of modes characterized by their radial quantum number n_r are showing up. For simplicity we show only the modes $n_r = 0$ and $n_r = 1$ on Fig. 5.9, calculated for a radius $a = 0.6\mu m$ and an index of refraction $n = 2.52$.

Before discussing the details of the calculation procedure for non-cylindrical NWs, it is helpful to consider qualitatively the expected modification of the mode spectra induced by the deviation of the NW's shape from the cylindrical geometry. When NW cross-

section is just slightly deviated from a circle, the qualitative description of the modes can be obtained by perturbative considerations. The approximations made within our model, which we are going to consider in more details in the second part of this section, are based on Rayleigh hypothesis for expansion of fields of modulated structures in cylindrical waves [44]. In the last ref. it is demonstrated that such expansion is valid for the perturbation of particular symmetry unless the ratio of the perturbation amplitude to the radius of cylinder exceed some critical value making the expansion divergent. Convex polygonal geometries, which we consider here to be cross-sections of NWs, fall deep below this critical point, defined for each type of polygonal shape separately (see Ref. [44]) justifying the validity of the method we use.

The small deviation of the boundary cross-section results in the mixing between the cylindrical modes of different momenta. The physical reason of this mixing is the additional scattering of a cylindrical mode on a non-cylindrical boundary. The 'selection rules' of this scattering obviously depend on the symmetry of the NW. In case of an hexagonal perturbation e.g., that is invariant in respect to any rotation on multiples of $2\pi/6$, the changes of angular momentum are the multiples of 6. As a result, each cylindrical mode acquires a 'tail' of other harmonics whose amplitude depends on the energy mismatch between the energy of the main mode and that of the member of the 'tail'. The less is the energy mismatch, the stronger is the admixture of the other state to the initial cylindrical mode. The states with opposite m are degenerate in the absence of magnetic field and consequently can be strongly coupled by the surface perturbation, in case when angular momentum difference corresponds to that of boundary perturbation.

To illustrate the mixing between the modes Fig. 5.9 shows the structure of the cylindrical modes for small angular momenta with superposed harmonics with the periodicity of hexagon (calculations shown in Fig. 5.9 are performed using matrix (2.24)).

For the hexagon, a strong coupling of degenerate harmonics occurs for $m-(-m) = 6k$, and results in strong mixing of the modes with $m = \pm 3$. As a result, the $m = \pm 3$ doublet splits into a pair of singlet states. The dependence of this splitting on the hexagonal perturbation is illustrated on Fig. 2.3 for a set of cross-sections smoothly varying from cylinder to hexagon for the same cross-sectional area. The radial position of the boundary for each angle was obtained by linear interpolation between the cylinder ($x = 0$) and the hexagon ($x = 1$), with x being the shape parameter

$$r(\phi) = (1 - x)r_C(\phi) + xr_H(\phi), \tag{2.25}$$

where with r we denote the NW's radius (subscripts C and H correspond to cylinder and hexagon, respectively).

Let us now discuss in more details the calculation procedure for non-cylindrical NWs. We assume that the solutions inside and outside the wire can be written as linear combinations of the cylindrical harmonics, according to the Rayleigh hypothesis. Boundary

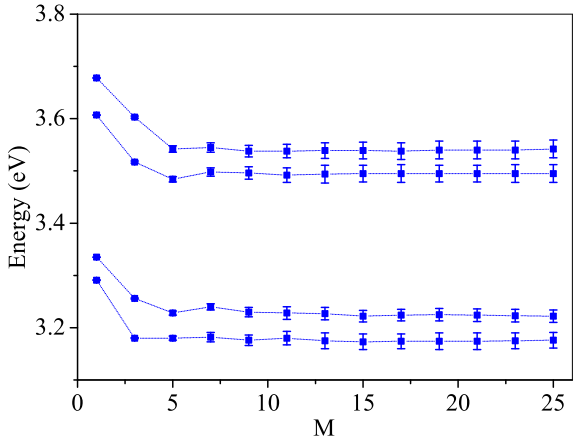

Figure 2.4 | Convergence of the modes $m = 2$(TE),$m = 3$(TM),$m = 3$(TE) and $m = 4$(TM) (modes of Fig. 2.7) being in the energy range 3.1-3.8 eV versus the number of cylindrical harmonics M used in the calculation. Vertical bars show imaginary part of each mode at given M

conditions in this case are more complicated. Single angular harmonics are no more proper solutions because they cannot match the tangential field boundary conditions on a boundary changing with the azimuth. The solution has to be written as an infinite combination of cylindrical harmonics as shown in Eq.(2.16)-Eq.(2.23). Moreover, because the normal to the boundary is not parallel to the radial vector, the tangential fields on the wire's surface contain both radial and azimuthal components (Fig. 2.1(b)):

$$\vec{E}_t^{in,out}(r_k,\varphi_k) = E_r^{in,out}(r_k,\varphi_k)\sin(\vec{\tau}\vec{e}_r)\vec{e}_r + E_\varphi^{in,out}(r_k,\varphi_k)\cos(\vec{\tau}\vec{e}_\varphi)\vec{e}_\varphi. \tag{2.26}$$

The matching of inside and outside fields should be realized at any angle $0 \leq \varphi_k < 2\pi/n$ with corresponding radius $r_k = r(\varphi_k)$ along the wire boundary. The r and φ components in the above expression are given by Eqs.(2.17,2.21) and Eqs.(2.16,2.20). The magnetic field tangential to the NW surface is described in a similar way. In order to keep a convenient matrix description of the problem, we are going to consider boundary conditions only for a finite number of points on the surface, and also to consider a finite number of cylindrical harmonics in the expressions for the electric and magnetic fields. In this framework, boundary conditions can be expressed through the matrix equation $\tilde{F}(\omega,k_z)\tilde{X} = 0$, where the matrix $\tilde{F}(\omega,k_z)$ is given by:

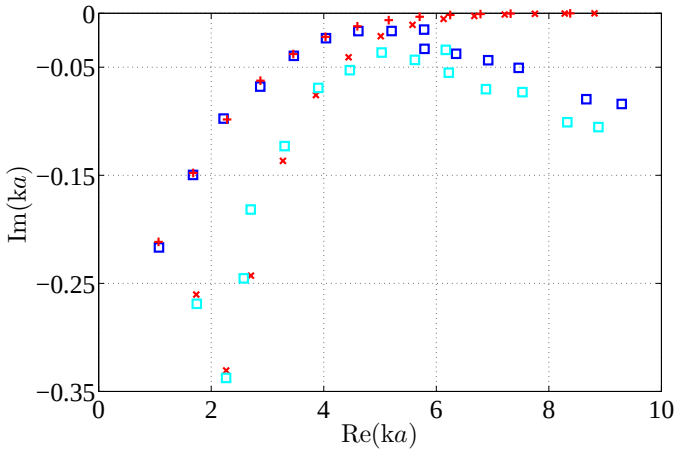

Figure 2.5 | The modes of hexagon in complex plane. The refractive index is $n = 2.1$ and the radius of the same cross-section surface cylinder $a = 300\ nm$. The upper branch (dark blue squares) shows TM modes and the lower one TE modes (bright blue squares). Corresponding cylindrical modes, with m increasing from left to right ($Re(ka)$-axis) are shown in both polarization with plus and x-signs.

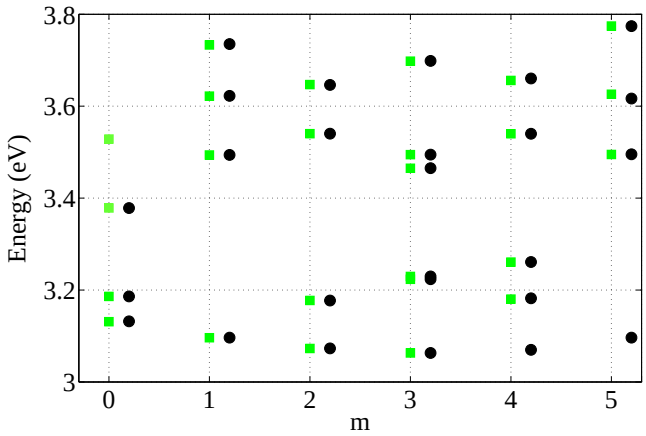

Figure 2.6 | Energy position of the hexagonal modes being in the chosen energy range (3.1-3.8 eV) versus their angular momentum. The circles show the modes belonging to the second "Brillouin zone".

$$\tilde{F}(\omega, k_z) = \begin{bmatrix} F_{11} & \cdots & F_{1m} & \cdots & F_{1M} \\ \vdots & & \vdots & & \vdots \\ F_{k1} & \cdots & F_{km} & \cdots & F_{kM} \\ \vdots & & \vdots & & \vdots \\ F_{K1} & \cdots & F_{Km} & \cdots & F_{KM} \end{bmatrix} \tag{2.27}$$

Here K is the number of points we take on the boundary and M is the number of harmonics we sum up. F_{km} stands for an analog of $F_m(\omega, k_z; r_k)$ - the matrices given by the expression (2.24) with tangential φ-components replaced by Eq.(2.26). These sub-matrices describe contribution of a single m-harmonic to the boundary condition in the surface point $r_k =$

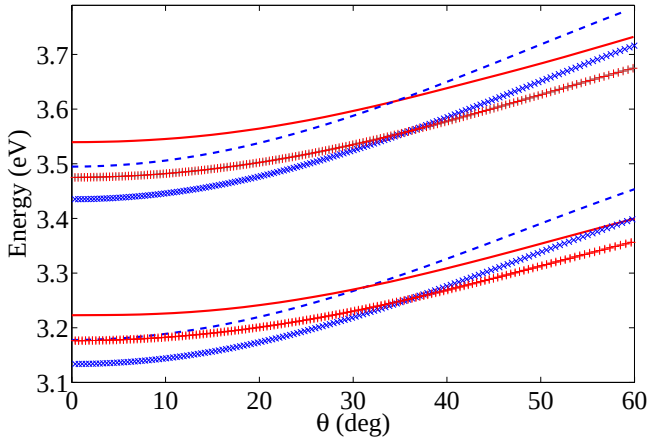

Figure 2.7 | The four lower energy branches show the dispersion of TE and TM modes of circular cross-section wires: TE, $m = 8$ (x symbols, blue) and TM, $m = 9$ (+ symbols, red) and of the corresponding hexagonal modes: TE, $m = 2$ (dashed blue line) and TM, $m = 3$ (full red line). The four upper branches are the same modes but replacing m by $m + 1$.

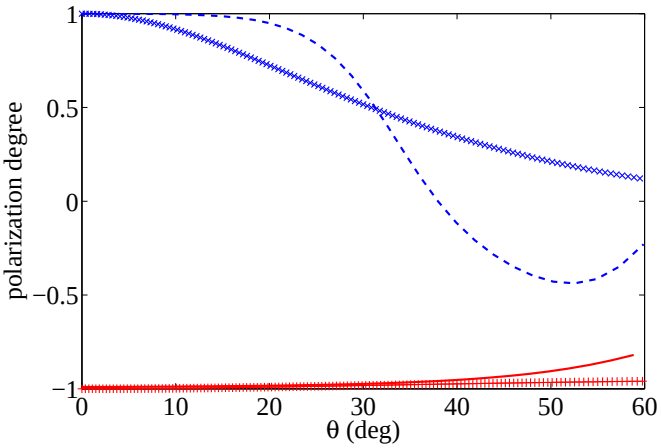

Figure 2.8 | Polarization degree of the lower energy modes of the Fig. 2.7: hexagon modes $m = 2$ (TE, red full line) and $m = 3$ (TM, blue dashed line) and corresponding cylindrical modes.

$r(\varphi_k)$. The vector $\tilde{X}$ is now a $4M$-dimensional colon $(X_1, \ldots, X_m, \ldots, X_M)^T$ and X_m is defined again like in the case of circular cross-section $X_m = (A_m, B_m, C_m, D_m)$. The meaning of the matrix (2.27) is that, in any point r_k on the NW's surface, the same linear combination of cylindrical harmonics allows to verify the boundary conditions in these points. Taking the number of harmonics equal to the number of points on the boundary $K = M$ allows us to make the matrix (2.27) square. In this case the eigenmodes $\omega(k_z)$ are found as the solutions of the system $\tilde{F}(\omega, k_z)\tilde{X} = 0$. Each eigenmode of a n-polygonal system contains in addition to the principal harmonic m all other harmonics which add to it by rule $m + sn$, where s is an non-zero integer (for hexagon $n = 6$). Such eigenmodes, resulting from summation over different harmonics, do not have a well

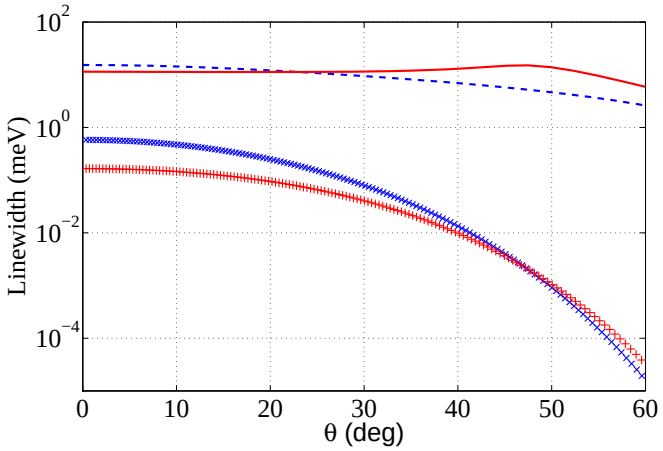

Figure 2.9 | Linewidths of the lower energy modes of the Fig. 2.7. The index of refraction is $n = 2.5$ and the cross section area $S = 0.09\pi\mu m^2$

defined angular momentum because of the fact that they are not eigenstates of angular momentum operator. Nevertheless, we will associate a number m corresponding to the angular momentum of the principal harmonic to each mode, like in the case of the cylinder. The dispersion of these modes $\omega(k_z)$ can be found solving $\det(\tilde{F}) = 0$ or alternatively by a more efficient numerical procedure [45, 46].

2.3 Numerical analysis

In this section we consider the important particular case of the hexagonal cross-section and compare the eigenmodes with the ones obtained for the cylinder. The special case of the hexagonal cross-section is of strong practical interest since it is realized experimentally by wires made of wurtzite semiconductors such as GaN and ZnO. The comparison with the cylindrical geometry is also particularly relevant since it is a much simpler problem to solve. In practice, modeling of hexagonal NWs is often performed using cylindrical description. In order to directly compare the properties of the modes in circular and polygonal cross-section NWs we have to consider structures having the same cross-section area. If the radius of the cylinder is a, then the large diagonal of the corresponding n-side polygon can be found from the formula $d = 2a(\csc(2\pi/n)2\pi/n)^{1/2}$.

Fig.2.5 shows the energy of the eigenmodes of hexagonal and cylindrical NWs in the complex plane, at $k_z = 0$, calculated with the same parameters as the one used for the Fig. 7 of Ref. [41]. In this last work, boundary element method (BEM) of Ref. [40] is used. Both simulations are in good agreement which demonstrate the reliability of our method.

We deduce empirically, how many cylindrical harmonics should be taken into account in order to get a good precision in the finding of the energies of the eigenmodes. We

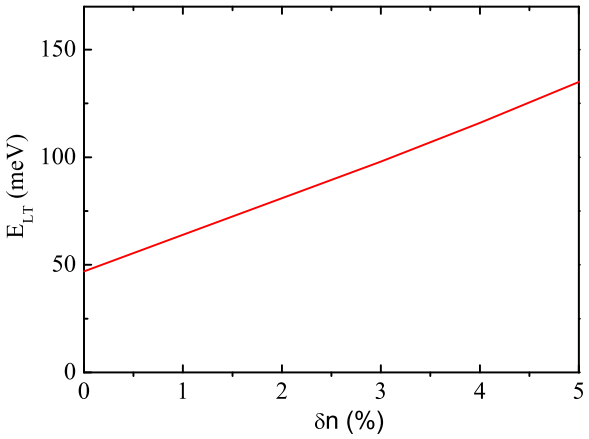

Figure 2.10 | Splitting between the modes TE($m = 3$) and TM ($m = 4$) of an hexagonal wire at $k_z = 0$.

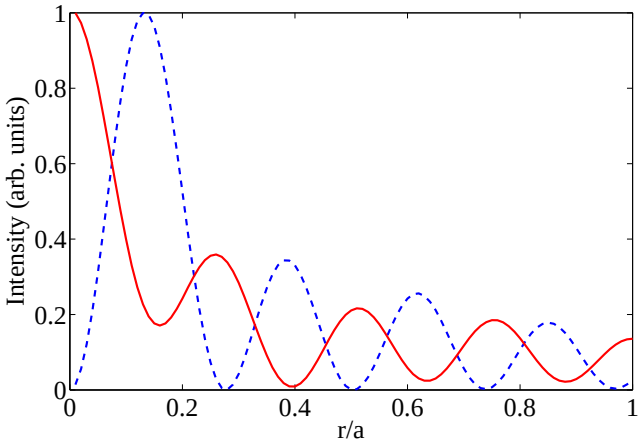

Figure 2.11 | Radial distribution of energy density for the upper pair of hexagon modes: TE($m = 3$)(full red line) and TM($m = 4$)(dashed blue line)

consider a NW with an hexagonal cross-section and circum-circle radius of 330 nm. For Fig. 2.4, we consider an isotropic dielectric response with an optical index 2.5. We look for the eigenmodes in the energy range 3.1-3.8 eV versus the number of cylindrical harmonics M taken into account in our calculations. One can clearly see that the energy of the modes converges for M large enough. In calculations which follows, we will use $M = 15$.

The energies of the modes are studied in the angular momentum space - m-space (Fig. 2.6). The modes of the hexagonal NW with the circum-circle radius of 330 nm are analyzed for $m = 0, ...11$, and the energies $m = 6, ..., 11$ are shown with some small shift with respect to the first six harmonics in order to ease the comparison. The number of modes and their energies repeat themselves with periodicity $\Delta m = 6$ as expected from the discussion on mode symmetries for hexagonal system. All relevant physical properties of a hexagonal NW can be therefore deduced looking into the first "Brillouin zone" placed

between $m = 0$ and $m = 5$.

Next, we compare the energy position, energy dispersion, and polarization of hexagonal and circular NWs. Such comparison has been already performed in Ref. [40], but only from the point of view of the energy positions of the eigenmodes at $k_z = 0$. We are focused on the particular energies (3.1-3.8 eV, Fig. 2.7) corresponding to the energy range in which semiconductor's excitons couple to light, like for example in ZnO NWs [39, 47]. The Fig. 2.7 shows the energy dispersions versus the angle of the incident light $\theta = \arcsin(k_z/k)$ (Fig. 2.1(a)) of the modes of two NWs with circular and hexagonal cross-section respectively, and having the same area. In both geometries the modes appear in TE-TM polarization pairs in one narrow energy range. The upper mode of the pair is characterized by an angular momentum m and is TM polarized, whereas the lower mode has an angular momentum $m-1$ and is TE polarized. The modes of the hexagon appear at higher energies and have a bit changed dispersion compared to those of the cylinder. Using slightly different index of refraction for the cylinder and the hexagon, it is possible to match the dispersion of one eigenmode of the two different structures. This shows that in practice the eigenmode of an hexagonal NW can be reasonably described by a simple model assuming a cylindrical geometry.

Both in the cylinder and in the hexagonal wires, the modes are purely TE and TM only at $k_z = 0$. The Fig. 2.8 shows dependence of the polarization degree $\rho = (I_{TE} - I_{TM})/(I_{TE} + I_{TM})$ of the modes versus the incidence angle. In the case of cylindrical wires ρ can be expressed directly through the coefficients of the external fields as $\rho_m = (|D_m|^2 - |C_m|^2)/(|C_m|^2 + |D_m|^2)$. The polarization degree of a TE mode decreases from 1 approaching zero value at higher angles. The polarization of a TM mode changes very slowly, remaining close to -1 for all θ. The polarization mixing in hexagonal NWs has a bit different behavior in comparison with the circular geometry case. This difference is most obvious for TE modes. After being almost constant for a wide range of angles, it starts to decrease significantly near $\theta \approx 30°$ and becomes even slightly TM polarized between 40° and 60°. On the other hand, the evolution of TM modes is similar to the case of cylindrical structure. Such behavior results form the mixing of the hight-m wispering gallery harmonics with low-m ones with larger radial numbers.

While calculating the modes linewidths, the mechanism which we consider is the leakage trough the NW interfaces. This is the dominant mechanism of losses in both cylindrical and hexagonal geometries. External waves are partially transmit at NW's boundaries due to difference of external and internal refraction indices. In our model this leakage is given by the imaginary part of the modes found by solving the eigenvalue problems Eq.(2.24) and Eq.(2.27). In the present analysis, we do not consider an excitonic contribution to the linewidths as we have already done in Ref. [39]. An extra contribution to the linewidths of the modes in hexagonal NWs related to the transmission exactly at the

edges is equally omitted here. Linewidths extracted from our calculations at $k_z = 0$, as it has already been mentioned coincide with those obtained by BEM (see Fig. 2.5 and Fig. 7 of Ref. [41]).

The main difference between the hexagon and circular cross-sections NWs lies in the linewidths of the eigenmodes which is much larger for the hexagonal structure. This is demonstrated by Fig. 2.9 which shows the mode linewidth versus angle for the 4 lower modes shown in the Fig. 2.7. The linewidths of the hexagon modes are about 10 meV which is more than an order of magnitude larger than in the cylinder. It is even much larger at higher angles for which the linewidths of the modes of the hexagon remain roughly constant whereas the ones of the cylinder drop by several orders of magnitude. This is due to more efficient transmission on hexagonal border than on cylindrical one resulting in larger linewidths for the hexagonal wire. In Ref. [40] mode-width dependence versus rounding of corners of hexagon was considered demonstrating (numerically) that transition from cylinder to hexagon is followed by an increase in linewidths. Another important feature of wurtzite materials is their optical birefringence. The optical index along the main c-axis, corresponding to the z-axis of the hexagonal NW differs from the one in the cross-section plane. The effect of the birefringence on the longitudinal-transverse splitting E_{LT} (energy splitting of TE and TM polarizations) is shown on Fig. 2.10 at $\theta = 0°$. E_{LT} depends linearly on δn and we show dependance for positive birefrigence as it is the case in ZnO wires [39]. Even a small birefringence leads to a significant splitting. It is therefore important to take the anisotropy into account in order to be able to reproduce realistic experimental situations. The radial dependence of the electromagnetic field density is shown in Fig. 2.11 for the case of hexagonal NW.

We have developed a method which allows to solve Maxwell's equations in NWs of discrete symmetries, and even ones showing an anisotropic dielectric response. This method can be applied to any system having the cross-section symmetry of regular polygons. It allows finding the eigenmodes of the structure (whispering gallery modes) labeled by their angular, or pseudo-angular momentum in the case of non-cylindrical structures. The dispersion (dependence of the energy on the wave vector along the wire axis), polarization, linewidth, and radial densities of the modes are calculated for the cases of hexagonal and circular cross-sections having the same areas. The modes in both cases appear to be quite similar, except from the point of view of the linewidths, which is much larger for hexagonal NWs. We have found some interesting polarization mixing effect with the transformation of TE modes close to $k_z = 0$ in modes mainly TM polarized.

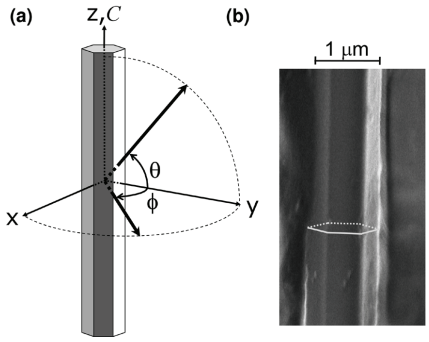

Figure 2.12 | a) Definition of the angles θ and ϕ b) Scanning Electron Microscope (SEM) image of the microwire under study in experiment

2.4 Room-temperature 1D polaritons

2.4.1 Introduction

Intense effort has been carried out over the last decade to realize photonic structures using wide band-gap semiconductor materials like III-Nitrides or Zinc-Oxide, which offer both large exciton oscillator strength and binding energy. However, the epitaxial growth of microcavities of high structural quality is challenging with these materials, due to the lack of adapted substrates and the large lattice mismatch within the same family materials: for example, 4% of lattice mismatch between GaN and AlN and - 10% between GaN and InN.

With an exciton binding energy of 60 meV and Bohr radius smaller than 2 nm, ZnO appears to be one of the most adapted semiconductor materials for the study of bosonic quantum degeneracy at elevated temperatures [48]. It is a direct wide bandgap semiconductor with a Wurtzite crystal structure, featuring three types of excitons: by order of increasing energy, A excitons are TE polarized (electric field E perpendicular to the wire c axis), B excitons are strongly TE and weakly TM polarized (E//c), and C excitons are weakly TE and strongly TM polarized [49]. In recent years, ZnO polaritons have been observed in various photonic structures [50, 51, 52, 53, 54, 47]. The strong coupling regime has been reported in Fabry-Perot bulk ZnO microcavities, which require the complex fabrication of hybrid and dielectric mirrors [50, 51, 52, 53]. In the most advanced structure, a quality factor of 500 and Rabi splitting of 80 meV have been obtained [52].

Much simpler photonic structures for ZnO polaritons are bulk microwires, which can be grown in very simple ovens [55]. Single crystalline ZnO microwires of hexagonal cross-section, with typical length of 50μm and diameter of 1μm, are grown by a vapor phase transport method under atmospheric pressure at about 900°C [55]. Surprisingly, this

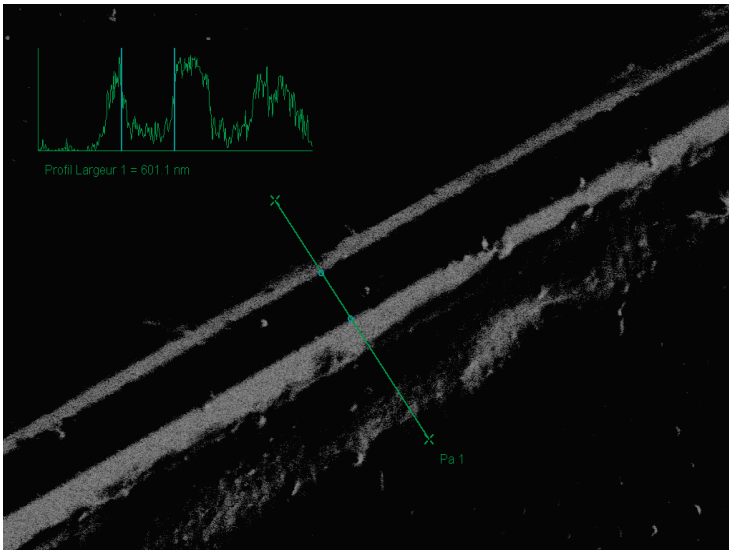

Figure 2.13 | Microwires are mechanically detached from their substrate and spread on a glass plate

rather simple growth method provides excellent regularity of the hexagonal shape and very low surface roughness, as shown by the SEM image of the microwire used in experiment on the Figure 2.12(b. In this system light can be highly confined and guided within the wire in modes similar to whispering gallery modes in microdisks [56], and strong coupling with the bulk exciton can be achieved [54, 47].

2.4.2 PL experiment

To get a deeper insight on the intrinsic properties of $1D$ polaritons in ZnO microwires, in [39] space and angle resolved photoluminescence spectroscopy of single ZnO microwires at various temperatures (5-300K) have been performed.

The ZnO microwires are spread on a glass substrate to which they remain loosely attached by some electrostatic forces of Van der Walls kind. Wires of good spectral quality have been selected for the experiments. The sample is placed into a variable temperature (5-300K) cryostat of large optical aperture. For angle-resolved measurement, a long segment (5μm length) of the microwire featuring constant diameter (like that shown on the figures 2.12b) and 2.13 for L=40μm-45μm) needs to be found, in order for the momentum k_z to be well defined. This segment is excited by the 325nm line of a CW He-Cd laser focused by an aspheric lens and passing through the rear side of the substrate. The photoluminescence is collected by a 0.5 NA NUV enhanced objective. The Fourier plane image is formed on the slit of a monochromator by a "4f" setup. For θ-resolved measurement, the wire axis is carefully set parallel to the slit by rotating the whole sample. For ϕ-resolved measurement, the wire axis is set perpendicular to the slit. Over-heating of the wire due the optical excitation is also checked spectrally: the laser intensity is set low enough to prevent any redshift of the spectrum. Angle resolved photoluminescence at room temperature are shown in 2.14 a) and 2.14 b) for two different orientations of

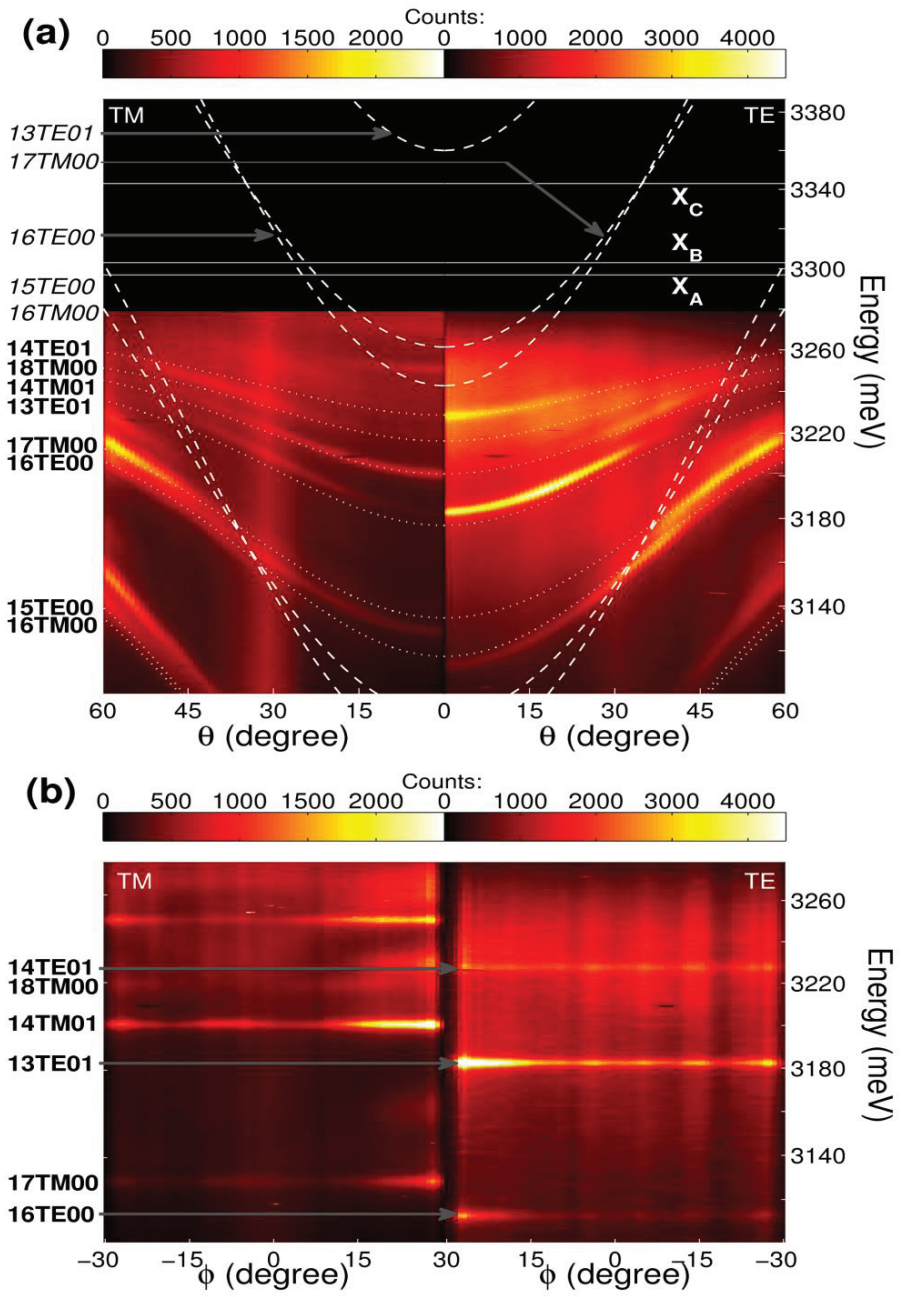

Figure 2.14 | Room temperature photoluminescence (PL) of microwire 2.13 for TE (right) and TM (left) polarizations. The emission intensity is color scaled (online) and increases from black to yellow. a) PL in the (θ, energy) dispersion plane. The dashed and solid lines represent the calculated dispersion of bare (uncoupled) cavity and exciton modes, respectively. The dotted lines represent the calculated polariton modes. b) PL in the (ϕ , energy) dispersion plane.

the detection angle θ and ϕ respectively (see 2.12a)). Due to the translational invariance along the wire main axis $z//c$, the emission angle θ is related to the polariton scalar momentum by $k_z = E\sin\theta/\hbar c$. Thus the Fig. 2.14 a represents also the dispersion of polaritons in the (Momentum, Energy) plane. Several well defined branches are visible, which can be separated into two families according to their linear polarization, i.e. mostly TE with respect to the main axis of the wire (electric field E perpendicular to the wire c axis, right side of the figure) or mostly TM ($E//c$, left side) at $k_z = 0$ ($\theta = 0$). They correspond to different lower polariton branches, which result from the coupling between A, B, and C excitons and different whispering gallery modes. Their dispersion features are typical of free polaritons:

1)modes of high energy (i.e. closer to the exciton resonances) have smaller dispersion than lower energy modes;

2)an inflexion point shows up at $\sim 40° - 50°$, which results from the onset of anti-crossing between the involved WGM and the exciton level.

The dispersion and polarization properties of these polariton branches are well accounted for, using a semi-classical calculation developed in the first part of this chapter which, as we have seen, takes into account the finite momentum k_z along the wire axis and the strong excitonic anisotropy in ZnO . This will be discussed in more details in the next section. Normal mode splittings about 200 meV are deduced from this modeling, which is less then in the bulk material.

The Fig. 2.14 b shows the polariton dispersion measured versus the angle ϕ . Polariton modes are now found to be strictly dispersionless, i.e. strictly monomode in the plane perpendicular to the wire main axis. This is direct evidence of the $1D$ nature of polaritons investigated here, rarely achieved before [57] and never with such a figure-of-merit, *a fortiori* at room temperature. They differ from polaritons confined along the c axis in ZnO wire cavities reported in [54, 58].

2.4.3 One-dimensional exciton-polaritons

Dispersion

We have already seen that we can quite reasonably describe energy dispersion of hexagonal wires using simple model with cylindrical geometry. To reproduce the data for this microwire, we solve Maxwell's equations like in the first part of this chapter in the cylindrical geometry, and take into account the anisotropy of the excitonic response. In cylindrical coordinates, the permittivity reads:

$$\varepsilon_{r(z)}(\omega) = \varepsilon_B \left(1 + \sum_{t=A,B,C} \frac{\omega_{t,LT}^{r(z)}}{\omega_{t,ex} - \omega - i\Gamma}\right) \tag{2.28}$$

Where $\omega_{t,LT}^{r(z)}$ are the longitudinal-transverse splittings along the microwire axis z and

the radial direction r in the cross-section plane, ε_B and Γ are the background dielectric constant and excitonic non-radiative decay rate, respectively, t_{ex} are the A, B and C excitonic resonances.

We again solve the boundary value problem using the formalism developed in the second section of this chapter, but now taking ZnO excitons into account with the permittivity 2.28. As shown on the Fig. 2.14a, the main polariton characteristics of the strong coupling are well reproduced by the model, and a general agreement can be found between calculated and measured mode dispersions. The parameters used in the fit are:

$$\text{a} = 500 \text{ nm}, \varepsilon_b = 6.35;$$

$$\hbar\omega_A = 3.297\text{eV}, \hbar\omega^r_{LT,A} = 2.7\text{meV};$$

$$\hbar\omega_B = 3.303\text{eV}, \hbar\omega^r_{LT,B} = 12.8\text{meV};$$

$$\hbar\omega_C = 3.343\text{eV}, \hbar\omega^z_{LT,C} = 16\text{meV};$$

and the other LT splittings are taken to be 0, i.e. A, B, and C excitons are assumed to be purely TE, TE, and TM polarized, respectively. The eight modes used in the modeling are (in order of decreasing energy) 14TE01, 18TM00, 14TM01, 13TE01, 17TM00, 16TE00, 15TE00, 16TM00 (the first number stands for m, the last for n_r - radial quantum number). The dashed and solid lines in the Figure 2.14a are the dispersions of the bare photonic and excitonic modes, respectively. The first four modes are positively detuned, while the last four ones are negatively detuned in energy with respect to the exciton modes. Changing the microwire radius by ± 20 nm would change indeed the mode quantum numbers. However a similar overall fit as displayed in the Fig.2.14 a can be achieved by adjusting the set of parameter values by less than $\pm 10\%$ percent. These values are also in general agreement with those of Refs. [47, 59, 60].

Rabi splitting

It is not straightforward to determine an exact Rabi-splitting because polariton modes at non zero θ result from the superposition between several excitonic and photonic modes. Depending on the mode label, normal mode Rabi splittings ranging from 170 to 200 meV are deduced from our calculation. This value, smaller than that expected in bulk ZnO (300meV) [61] result from the evanescent part of the hexagonal WGMs which obviously doesnt overlap excitons, and which is larger in the case of hexagonal cross section than in the case of circular. To this should be added the non-perfectly homogeneous exciton spatial distribution in the material, in particular in the vicinity of the semiconductor/air interfaces where large electric field can be found [62].

Polarization

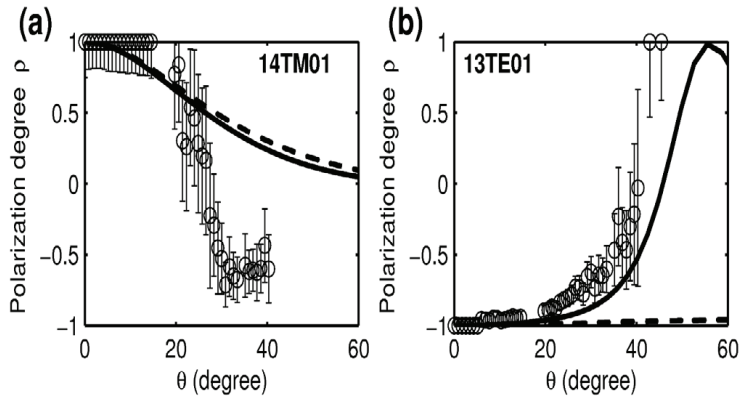

Figure 2.15 | Angular dependence of the polarization degree of modes a) 14TM01 and b) 13TE01. Angular dependence of the full width at half maximum of modes. Open symbols are the measurements, solid and dashed lines are the calculations for polariton modes and bare (uncoupled) optical modes, respectively.

The angular (θ) dependence of the polarization degree of every mode in the strong coupling regime is highly non-trivial. A measurement for modes 13TE01 and 14TM01 is shown in Figures Ia and Ib. The most striking feature is the change in the polarization observed with increasing emission angle the 13TE01 (14TM01) mode at $\theta = 0°$ completely switches to TM (TE) mode at $\theta \sim 40°$ (30°). This polarization switching is mainly due to the strong coupling, which mixes the cavity mode with each exciton state simultaneously. It is satisfactorily reproduced by the model (solid lines in Figs.Ia and Ib) for the TE mode but not for the TM mode. In fact a complete agreement on this point is more difficult to achieve for two reasons:

1) the polarization mixing is sensitive to the geometry of the system (our model assumes a circular and not hexagonal cavity);

2) the weak TM (TE) component of B (C) excitons have been neglected.

The first difference of two models we have discussed when we compared mode degree of polarization as a function of θ for cylindrical and hexagonal wires (the Fig. **??**).

2.4.4 Interaction with phonons

The other striking feature of the Fig. 2.14 is the sharpness of the polariton lines, with FWHM of 4 meV only for polaritons with half excitonic fraction (zero exciton-photon detuning), leading to a record figure-of-merit of 75 for the strong coupling regime at room temperature. This small line-width seems at first glance contradictory to the phonon damping of 40 meV reported for bare excitons [63], since the polariton line-width is usually assumed to scale as the mean value of the bare exciton and bare photon line-widths. In fact this assumption, based on the coupling between two damped classical oscillators, cannot properly account for the phonon contribution to the polariton line-width in ZnO microwires, because the exciton-photon interaction dominates over the exciton-phonon interaction by one order of magnitude [64]. In such a case, the phonon damping should be directly evaluated in the polariton states, using the Fermi golden rule. To compute the phonon contribution to the damping of a given polariton state at $k_z = 0$, we then apply Fermi golden rule including the scattering of the polariton (with the exciton/photon detuning as a parameter), which includes all scattering events towards polaritonic ($1D$) and excitonic states ($3D$) by absorption or emission of phonons. Interactions with acoustic and optical phonons are considered. A similar calculation has been done in [65] for bulk exciton-polaritons.

The results, assuming polariton scattering with a thermal bath of acoustical and optical phonons, are shown on the Fig.2.16 (a) and (b) (red solid line) for low and high temperatures (70K and 300K). The calculations show that phonon damping dramatically increases upon increasing temperature only for polariton modes contained within the energy range $[E_X, E_X - E_{LO}]$ ($E_{LO} \leq 72$ meV), while those below remain virtually unaffected, regardless of their excitonic fraction.

This phenomenon clearly shows up in the measurements of the Fig.2.16a and 2.16b: at T=300K, the polariton modes S3 to S5 are completely washed out by phonon damping upon increasing the temperature. On the other hand, the S2 polariton mode remains unaffected for large L (energy lower than $E_X - E_{LO}$) until it reaches the boundary energy $E_X - E_{LO}$ at position L=34 μm. Then, for lower L, i.e. energy larger than $E_X - E_{LO}$, it is completely suppressed. This occurs in spite of S2 polariton mode excitonic fraction exceeds 50%.

This behavior is due to LO-phonon scattering of these high energy polaritons toward higher momentum free exciton states, a very efficient process owing to the very high density of states of three-dimensional bare excitons outside the light cone. On the other hand, phonon scattering of lower energy polaritons involves only one dimensional polariton states. There, the phonon damping of polaritons is strongly reduced as compared to excitons, because the polariton density of states, which scales as the polariton mass, is lower by four orders of magnitude. From these considerations, a criterion can be drawn

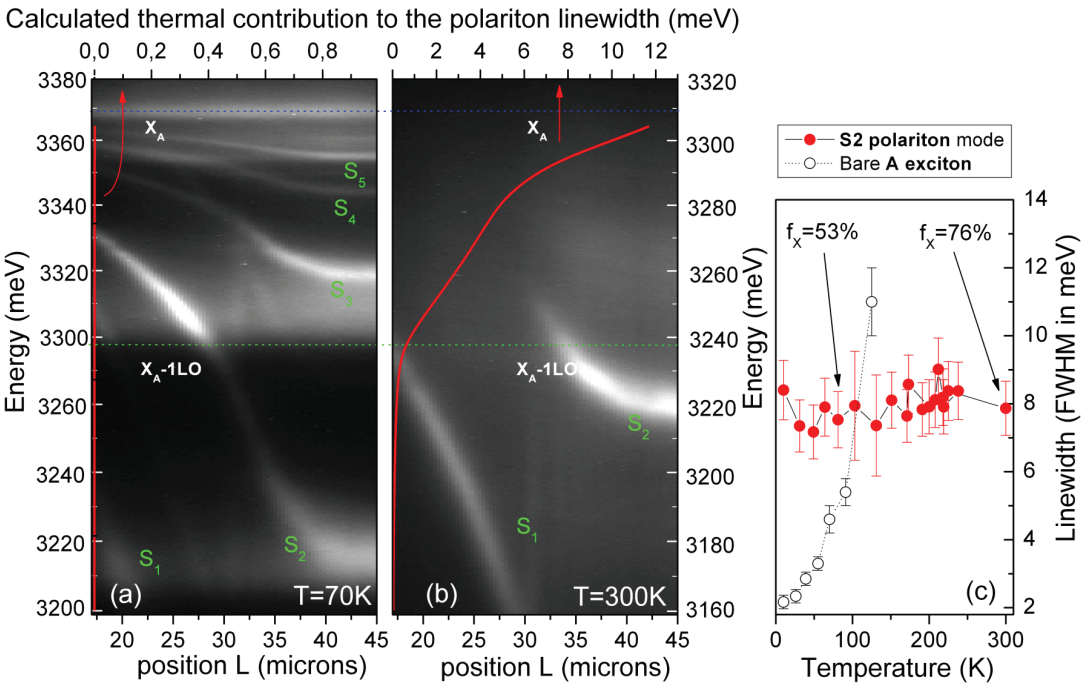

Figure 2.16 | Spatially resolved TE-polarized emission spectrum along 26 microns length of microwire 2 at temperature T=70K (a) and T=300K (b). In this place of microwire, the inhomogeneous diameter (presently increasing from left to right) provides a natural way to continuously vary the exciton/photon detuning. S1 to S5 are the labels of five visible polariton modes. The free A exciton level X_A is materialized by the blue dotted line and the green dotted line figures the A exciton energy minus 1 LO-phonon energy (E_LO=72meV). The red plot shows a calculation of the phonon contribution to the polariton line-width versus energy. At room temperature modes (b) S3, S4, S5 have vanished due to the excessive broadening taking place in the region $[X_A, X_A - E_{LO}]$, while those at lower energy S1 and a part of S2 (right side of the wire) remain virtually unaffected regardless of their significant excitonic fraction. Interestingly, when S2 crosses the energy boundary $E = X_A - E_{LO}$ at 300K (at position L=34 μm), it abruptly vanishes. (c) plots the homogeneous line-width of polariton mode S2 versus temperature (red filled circles) extracted from angle-resolved emission measurement carried out in a region centered on L= 43 μm. There, the S2 mode energy lies below $E_X - E_{LO}$. In agreement with the calculation, although its excitonic fraction steadily increases from 50% at 10K to 76% at 300K, no measurable thermal contribution to the line-width builds up upon increasing the temperature to 300K. The line-width of bare A exciton is plotted versus temperature for comparison (hollow circles).

for this phonon quenching to be achieved: half the normal mode splitting must exceed the LO phonon energy, i.e.

$$\hbar\Omega_R/2 > E_{LO} \tag{2.29}$$

In practice, this criterion is usually difficult to meet considering the large LO phonon energy in most semiconductors. In ZnO microwires this criterion is met for the first time thanks to the very large oscillator strength, particularly that of C exciton.

2.4.5 Conclusions

In the first section of this chapter we have developed a method which allows to solve Maxwell's equations in NWs of discrete symmetries, and even ones showing an anisotropic dielectric response. This method can be applied to any system having the cross section symmetry of regular polygons. It allows to find the eigenmodes of the structure (whispering gallery modes) labeled by their angular, or pseudo-angular momentum in the case of non-cylindrical structures. The dispersion (dependence of the energy on the wave vector along the wire axis), polarization, line-width, and radial densities of the modes were calculated for the cases of hexagonal and circular cross sections having the same area respectively. The modes in both cases appear to be quite similar, except from the point of view of the line-width, which is much larger for hexagonal NWs. We have found some interesting polarization mixing effects, with the transformation of TE modes close to $k_z = 0$ in modes mainly TM polarized.

In the second part of Chapter 2 we have shown that the strong coupling between whispering gallery modes and excitons in ZnO microwires results in the formation of $1D$ exciton polaritons, with Rabi splitting of about 200 meV. We demonstrate experimentally and theoretically that these $1D$ polaritons can be thermodynamically decoupled from the phonon bath, a very advantageous situation to maintain high coherence at elevated temperatures. Thus, with a record exciton binding energy of 60 meV, polaritons in ZnO microwires appear as one of the most promising Bose gases for fundamental physics and practical applications. For example, by adjusting the photon-exciton detuning with the wire diameter, one can change the strength of the repulsive polariton interaction to address the various $1D$ physics issues, e.g. quantum fluctuations and quasi condensation [66], thermalization and quantum Newton's cradle [67], fermionization in a Tonks-Girardeau gas [68], etc... The demonstration of high quality polaritons in ZnO microwires also opens new prospects for the fabrication in the near future of ultra compact and low cost polariton "lasers" [48], ultrafast parametric amplifiers [69], or non classical source of photon pairs [70] operating at unprecedented high temperatures.

Chapter 3

Josephson effect of excitons and exciton-polaritons

The first section of Chapter 3 will be devoted to Josephson effect named after B.D. Josephson, who theoretically discovered a current across two weakly coupled superconductors separated by an insulator [71]. An brief review of DC and AC Josephson effects will be given, following the reference [37]. The same theoretical approach will be applied for weakly coupled BECs leading to a system of two coupled equations for population imbalance and phase difference. In the second part we consider Josephson effect of exciton-polaritons accounting for the polarization degree of freedom. We will address intrinsic and extrinsic Josephson dynamics, showing Josephson-like oscillations and the so-called regime of macroscopic quantum self-trapping, depending on initial conditions. An interesting effect of spatial separation of polarizations may occur for coupled BECs of exciton-polaritons [72].

Contents

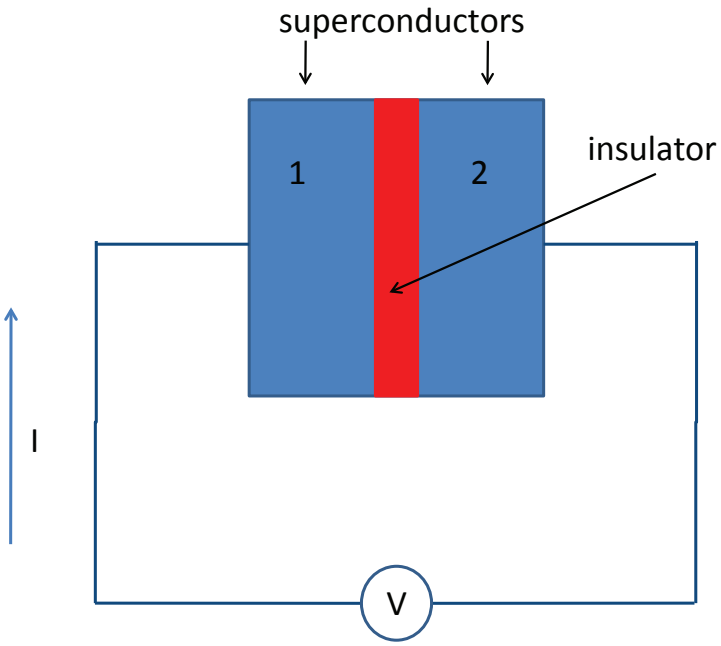

Figure 3.1 | Superconductor Josephson junction: V denotes voltage and I denotes current

3.1 Superconductor Josephson junction - SJJ

After the theoretical prediction [71], Josephson effect was experimentally observed by [73]. Cooper-pair Josephson junction consists of an insulator sandwiched by two superconductors 3.1. The particles pass through via quantum tunneling and the DC or AC current across the insulator can be measured depending on the applied voltage V. Superconductors are coupled linearly due to very weak tunneling. Thus, JJ (Josephson junction) dynamics is governed by system of two coupled Schrödinger equations, one for each superconducting subsystem

$$i\hbar\frac{d\psi_1}{dt} = eV\psi_1 - J\psi_2 \tag{3.1}$$

$$i\hbar\frac{d\psi_2}{dt} = -eV\psi_2 - J\psi_1. \tag{3.2}$$

The tunneling is given by J. The ψ_i is the order parameter and, being a complex number, can be written as

$$\psi_i(t) = \sqrt{N_i(t)}\exp(i\theta_i(t)) \tag{3.3}$$

where i=1,2 (see the Fig. 3.1). $N_i(t)$ is the particle number and $\theta_i(t)$ is the phase.

We should note here that the superconductor phase is described by Cooper pairs: two-electron bound state with zero spin satisfying Ginzburg-Landau equation. The above system of equations 3.1 and 3.2 arises when one neglects dissipation and non-linearity. In the next part we will allow for nonlinearities to obtain a system of two coupled GP equations to describe Boson Josephson junction (BJJ). The formal equivalence of Superconductor JJ (SJJ) and BJJ is a consequence of known similarity of superconducting and superfluid phenomena. The trial function 3.3 transforms each of starting equations into

$$\frac{i\hbar}{2\sqrt{N_i}}\frac{dN_i}{dt} - \hbar\sqrt{N_i}\dot{\theta}_i = \pm eV\sqrt{N_i} - J\sqrt{N_{i\pm1}}\exp\left(\theta_{i\pm1} - \theta_i\right). \tag{3.4}$$

The first sign corresponds to $i = 1$ and the second to $i = 2$. We omitted the t-dependance to shorten notation and dot stands for time derivate. As the latter equation is complex, the imaginary and real parts have to equal zero independently, giving

$$\frac{dN_i}{dt} = -\frac{2J}{\hbar}\sqrt{N_i N_{i\pm1}}\sin\theta, \tag{3.5}$$

$$\frac{d\theta_i}{dt} = \mp\frac{eV}{\hbar} + \frac{J}{\hbar}\sqrt{\frac{N_{i\pm1}}{N_i}}\cos\theta; \tag{3.6}$$

where $\theta = \theta_2 - \theta_1$ is phase difference between superconductors 2 and 1. After some very simple algebra we obtain an equation for θ

$$\frac{d\theta}{dt} = \frac{2eV}{\hbar} + \frac{J}{\hbar}\sqrt{\frac{N_1}{N_2} - \frac{N_2}{N_1}}\cos\theta. \tag{3.7}$$

As $N_1 \approx N_2$,since an external force due to applied voltage removes charge imbalance [74, 75], equation 3.7 reads

$$\frac{d\theta}{dt} = \frac{2eV}{\hbar}. \tag{3.8}$$

and to get phase difference θ one has to know explicitly the time-dependance of voltage V=V(t).

The total number of particles $N_T = N_1 + N_2$ is conserved in non-dissipative systems.The current I is

$$I = e\frac{dN_1}{dt} = I_0\sin\theta \tag{3.9}$$

with amplitude I_0

$$I_0 = -\frac{2eJ}{\hbar}\sqrt{N_1 N_2} \approx -\frac{eJN_T}{\hbar}. \tag{3.10}$$

being constant due to conservation of total number of particles. The current-voltage characteristic of SJJ is

$$I = I_0\sin\theta, \tag{3.11}$$

$$V = \frac{\hbar}{2e}\frac{d\theta}{dt}. \tag{3.12}$$

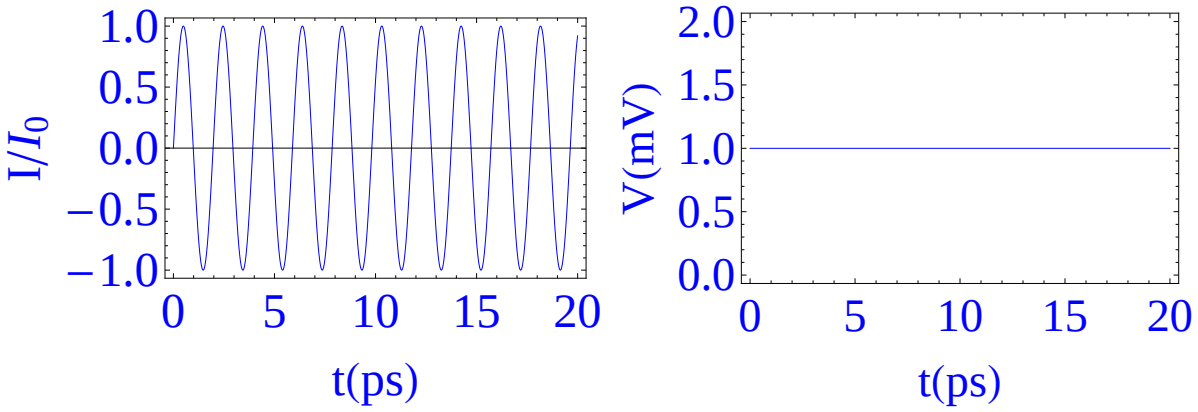

Figure 3.2 | Current (right) and voltage (left) of superconductor Josephson junction with $V = V_0$

With no external field $V = 0$, we have a DC current $I_0 \sin \phi_0$ across the insulating barrier which can take values from $[-I_0, I_0]$ depending on the initial phase difference of two superconductors.

Applying a constant voltage $V = V_0$, we have the phase difference which changes linearly with time in addition to the constant factor ϕ_0 we had in the case of absence of external field

$$\phi(t) = \phi_0 + \frac{2eV_0}{\hbar}t. \tag{3.13}$$

and for the current I we have expression

$$I(t) = I_0 \sin\left(\phi_0 + \frac{2eV_0}{\hbar}t\right). \tag{3.14}$$

This is AC current which we have obtained applying constant voltage. For typical values of voltage $\sim mV$ (right panel of Fig. 3.2) it oscillates with very high frequency $\sim 10^12Hz$ and averages to zero

$$< I >= 0, \tag{3.15}$$

where <> denotes averaging over time.

The next situation is to consider a time dependent voltage

$$V(t) = V_0 + V_1 \cos(\omega t), \tag{3.16}$$

which we can understand as lowest order expansion of some periodic function in harmonic series. Therefore, equation 3.12 takes the form

$$\frac{d\theta}{dt} = \omega_0 + \omega_1 \cos(\omega t), \tag{3.17}$$

with

$$\omega_0 = \frac{2e}{\hbar}V_0, \quad \omega_1 = \frac{2e}{\hbar}V_1. \tag{3.18}$$

The phase difference and the current are given by expressions

$$\theta(t) = \theta_0 + \omega_0 t + \frac{\omega_1}{\omega}\sin(\omega t), \tag{3.19}$$

$$I(t) = I_0 \sin(\theta_0 + \omega_0 t + \frac{\omega_1}{\omega}\sin(\omega t)). \tag{3.20}$$

In order to compare the expression 3.20 for the current when we apply the voltage given by 3.16 with the current in the case of constant voltage V_0 we make the replacement

$$A = \theta_0 + \omega_0 t \;\; and \;\; B = \frac{\omega_1}{\omega}\sin(\omega t) \tag{3.21}$$

and write

$$I(t) = I_0 \sin(A + B) = I_0(\sin A \cos B + \sin B \cos A). \tag{3.22}$$

In practice, $\omega_0 >> \omega_1$ so that B is very small number allowing us to make approximations $\sin B \approx B$ and $\cos B \approx 1$ and previous expression transforms into

$$I(t) = I_0 \sin(A + B) \approx I_0(\sin A + B \cos A). \tag{3.23}$$

After some straightforward calculation we get the final expression for the current in the case of alternating voltage

$$I(t) = I_0 \sin(\theta_0 + \omega_0 t) + I_0 \frac{\omega_1}{2\omega}[\sin(\theta_0 + (\omega + \omega_0)t) + \sin(\theta_0 + (\omega - \omega_0)t)]. \tag{3.24}$$

If we compare this expression with equation 3.24 we see that the difference is in the last term of the previous equation which adds due to harmonic change of the voltage with time. An average over time gives a quite interesting result

$$< I >= \begin{cases} 0 & (\omega \neq \omega_0) \\ I_0 \sin\theta_0 & (\omega \approx \omega_0) \end{cases} \tag{3.25}$$

Under an alternating voltage we obtain a DC current (in average) if the frequency is in resonance with ω_0. The current and voltage are shown on the Fig. 3.3, left and right panel, respectively. To stress the non-linear effect of the time dependent term of the voltage, an elevated value of frequency ω_1 is used. We clearly see that current oscillations becomes anharmonic, in comparison with the case of constant voltage. This higher harmonic oscillation, observed when the voltage frequency is in resonance with the frequency of lowest harmonic ω_0, is known as Shapiro resonance effect [75].

To summarize: absence of voltage $V = 0$ gives a DC current - DC Josephson effect. Constant voltage $V = V_0$ gives an AC current of high frequency which averages to zero in time, independently of the initial value of phase difference θ_0 between the two superconductors. This is AC Josephson effect acting as a voltage-to-frequency converter. For V of the form 3.16, at resonance, we obtain DC current $I_0 \sin\theta_0$. This is the so-called inverse AC Josephson effect and it operates as a frequency-to-voltage converter. In the literature one can find another classification, when the alternating (AC) and direct (DC) are related to t-dependance of voltage applied to the Josephson junction.

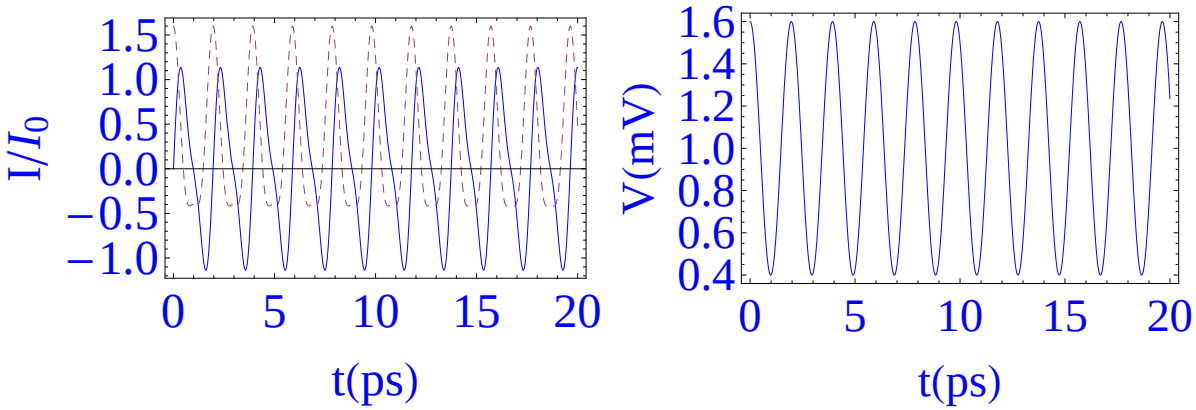

Figure 3.3 | Current (right) and voltage (left) of superconductor Josephson junction with with alternating voltage V 3.16. Full line of right panel corresponds to $\theta_0 = 0$ and dashed line to $\theta_0 = \pi/2$

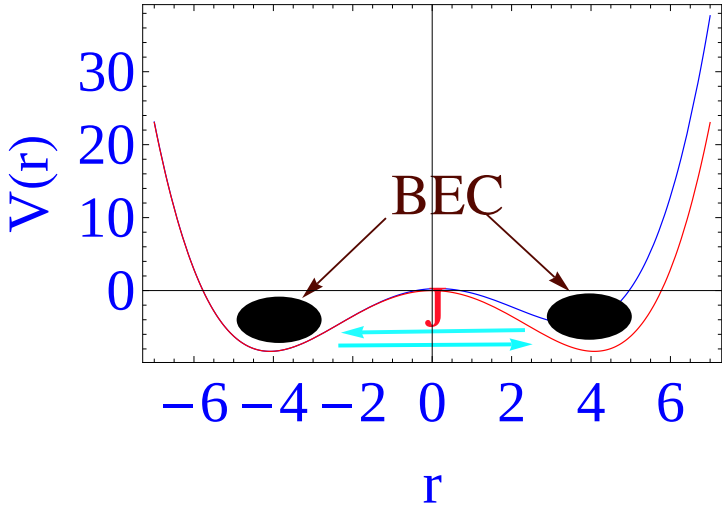

Figure 3.4 | Boson Josephson junction with double-well potential: symmetric (red line) and asymmetric double-well (blue line)

3.2 Boson Josephson junctions - BJJ

For bosonic system, the analogue of quantum tunneling through the insulator barrier between superconductors in SJJ, is the transport of bosons through the barrier of a double-well potential formed by some external means 3.4. We are interested in collective behavior of bosons including coherent phenomena and the natural departure point for this case is the GP equation. A double well trap can be created for example dividing external potential by a far-off resonance barrier or by some other experimental technique to make a BEC Josephson junction. The Josephson effect was observed not so long ago for interacting atomic condensates [76]. Previously it was observed in a superfluid system: two superfluid helium vessels connected by a nanoscale aperture [77].

We start by expanding the order parameter $\psi(r,t)$ in the time-dependent GP equation 1.102 on the eigenstates of double well potential $V_{ext}(r)$

$$\Psi(r,t) = \Psi_1(t)\phi_1(r) + \Psi_2(t)\phi_2(r). \tag{3.26}$$

where $\phi_1(r)$ and $\phi_2(r)$ are the ground states of well 1 and well 2, respectively. To simplify notation here we drop the index 0 for the ground state. Using again the ansatz 3.3 for amplitudes $\Psi_1(t)$ and $\Psi_1(t)$ like for the case of SJJ, we get the two-mode dynamical equations [75]

$$i\hbar\frac{d\psi_1}{dt} = (E_1^0 + U_1|\psi_1|^2)\psi_1 - J\psi_2, \tag{3.27}$$

$$i\hbar\frac{d\psi_2}{dt} = (E_2^0 + U_2|\psi_2|^2)\psi_2 - J\psi_1, \tag{3.28}$$

where again, like for SJJ, we neglect damping but with allowance for inter-particle interaction represented through non-linear terms. In two-mode approximation the thermal part (excited states) are also neglected. E_1^0 and E_2^0 are the energies of ground states in wells 1 and 2 respectively. For symmetric potentials (red line on the Fig. 3.4) $E_1^0 = E_2^0$. U_1 and U_2 represent inter-particle interactions and are given by

$$U_{1,2} = g\int d^3r|\psi_{1,2}(r)|^4. \tag{3.29}$$

where $g = 4\pi\hbar^2 a/m$; a is s-wave scattering length and m is particle mass. Josephson coupling J is

$$J = \int d^3r\psi_{1,2}^*(r)\left(-\frac{\hbar^2}{2m}\Delta + V_{ext}(r)\right)\psi_{2,1}(r). \tag{3.30}$$

In the basis of symmetric $\psi_+ = 1/\sqrt{2}(\psi_1+\psi_2)$ and anti-symmetric states $\psi_- = 1/\sqrt{2}(\psi_1-\psi_2)$ we see that Josephson coupling J is the difference between the energies of symmetric and anti-symmetric states

$$2J = E_+ - E_-, \tag{3.31}$$

and is negative as the energy of symmetric state is below the energy of anti-symmetric state $E_+ < E_-$. We are now going to write equations for population imbalance $z(t)$

$$z(t) = \frac{N_2(t) - N_1(t)}{N_T}, \tag{3.32}$$

and phase difference

$$\theta(t) = \theta_2(t) - \theta_1(t), \tag{3.33}$$

from the system 3.27-3.28. We have

$$\frac{dz(t)}{dt} = -\sqrt{1 - z^2(t)}\sin(\theta(t)), \tag{3.34}$$

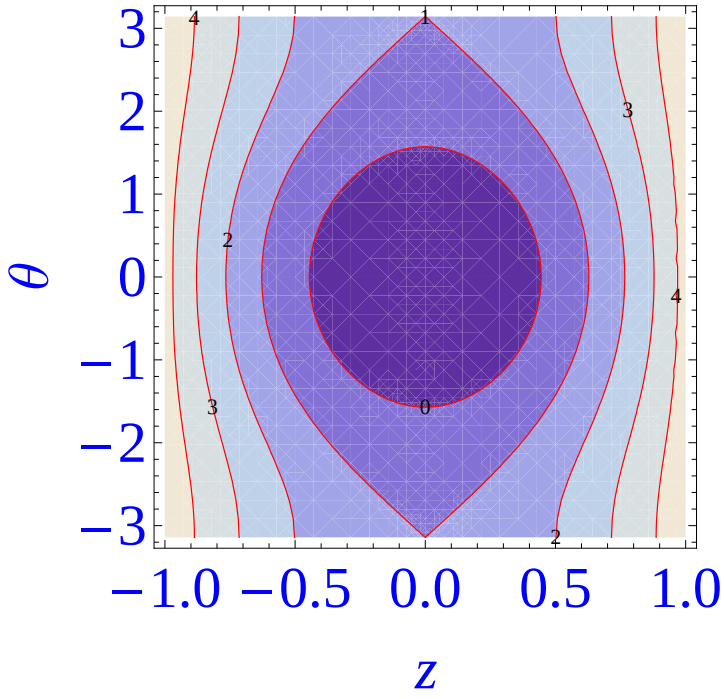

Figure 3.5 | Hamiltonian 3.37 in phase space (z,θ). Contour lines for H=0,1,2,3 and 4 are labeled

$$\frac{d\theta(t)}{dt} = \Lambda z(t) + \frac{z(t)}{\sqrt{1-z^2(t)}}\cos(\theta(t)). \tag{3.35}$$

where normalization with respect to time t is introduced in this way: $t \to 2tJ/\hbar$. An extra term ΔE adds to second equation 3.35 in the case of non-symmetric double-well potential and/or for $U_1 \neq U_2$. Here we will concentrate on the case of a symmetric double-well. The constants Λ and U equal

$$\Lambda = \frac{UN_T}{2J} \qquad U = \frac{1}{2}(U_1 + U_2). \tag{3.36}$$

The Hamiltonian of the system is

$$H(z(t),\phi(t)) = \Lambda\frac{z(t)^2}{2} - \cos\phi(t)\sqrt{1-z(t)^2} \tag{3.37}$$

and this Hamiltonian is an constant of motion which means that

$$H(z(t),\phi(t)) = H(z(0),\phi(0)) = \Lambda\frac{z(0)^2}{2} - \cos\phi(0)\sqrt{1-z(0)^2} \tag{3.38}$$

the total energy is fixed only by initial values of variables $z(t)$ and $\phi(t)$.

If two BECs have the relative phase at $t = 0$: $\theta(0) = 0$ from phase plot (z,θ) of Hamiltonian 3.37 (the Fig. 3.5) we distinguish two main regimes. The line H=1 separates trapped from untrapped motion and is called separatrix.

In the region $H < 1$ the motion is oscillatory: population imbalance changes from z to $-z$ on the line $H = const$ and the value of the constant depend on the initial conditions.

This is the regime of Josephson oscillations between two linked condensates. They are characterized with zero time-avered value of population imbalance:

$$< z(t) >= 0. \tag{3.39}$$

As we fixed $\theta(0) = 0$, there is some critical population imbalance z_c defined for $H = 1$ at which system undergoes phase transition. Above this point we have a trapped motion: population imbalance never fall to zero value. For a given system Λ , defined by relation 3.37 determines the value of z_c by expression

$$\Lambda\frac{z_c^2}{2} - \cos\phi(0)\sqrt{1 - z_c^2} = 1. \tag{3.40}$$

This phase is characterized by non-zero mean value of z

$$< z(t) >\neq 0. \tag{3.41}$$

This is regime of so-called Macroscopic Quantum Self Trapping (MQST).

An analytical solution for the $z(t)$ can be found in terms of Jacobian elliptic functions given in reference [75]. The solution formally coincides with equation for polarons (phonon-polaritons) [78].

$$z(t) = \begin{cases} Ccn[(C\Lambda/k)(t - t_0), k] & (0 < k < 1); \\ Cdn[(C\Lambda)(t - t_0), 1/k] & (k > 1). \end{cases} \tag{3.42}$$

First line corresponds to Josephson-like oscillation and the second one to MQST. Jacobi elliptic functions are denoted by $cn(x, k)$ and $dn(x, k)$. Quantities C,k are defined by expressions

$$C^2 = \frac{2}{\Lambda^2}(H_0\Lambda - 1 + \sqrt{\Lambda^2 + 1 - 2H_0\Lambda}). \tag{3.43}$$

$$k^2 = \frac{1}{2}(1 + \frac{H_0\Lambda - 1}{\sqrt{\Lambda^2 + 1 - 2H_0\Lambda}}). \tag{3.44}$$

More details on expression for the shift t_0 can be found in [75].

3.3 Josephson effect of exciton-polaritons

3.3.1 Introduction

Strictly speaking, being 2D objects, polaritons, and QW excitons can undergo BEC only when confined in a potential trap. The latter can appear due to the intrinsic lateral photonic disorder in a cavity (as it was the case in ref. [29]) or can be created in a controllable way by external laser beams [79], the application of stress [80] or using photolitographic techniques [81]. The possibility of engineering of a spatial confinement opens a way to the

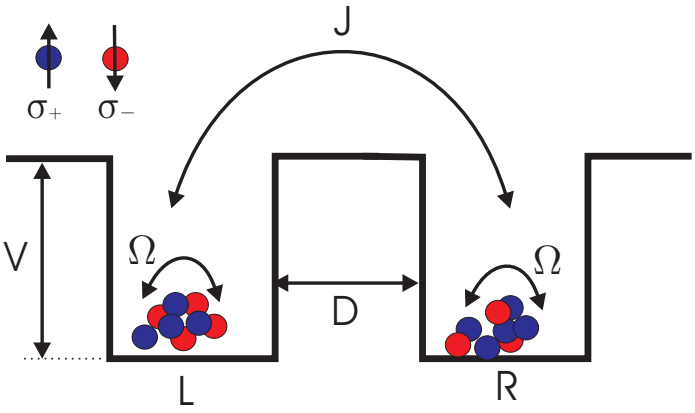

Figure 3.6 | The model system for the Josephson effect of exciton polaritons:Ω is the coupling of particles in one well with different polarization, J is the coupling of particles with the same polarization but in different wells, D is the interwell distance and V the potential depth. L and R are the indices for the two wells.

investigation of the Josephson effects for excitons and polaritons, related to the tunneling between two condensates possessing macroscopic phase coherence.

The important peculiarity of optically active $2D$ excitons and polaritons is linked with their spin-structure: they have two allowed spin projections on the structure growth axis, related to the right- and left- circular polarization of the counterpart photons. Moreover, due to the effects of exchange, the inter-particle interactions are strongly spin-anisotropic [82, 83]: particles with similar spin projections strongly repel, while particles with opposite spin projections almost do not interact with each other [84]. All this makes exciton and polariton condensates behave differently from atomic condensates or superfluids even in the thermodynamic limit. The real-space dynamics of polariton droplets is qualitatively different from those of atomic superfluids and reveals strong polarization effects [85]. The crucial property of the condensates of cold atoms and the condensates of excitons and polaritons, as compared to the superconductors, is the interaction between the tunneling particles.

This leads to the striking nonlinear effects in Josephson dynamics, such as anharmonicity of the Josephson oscillations [86, 87] and macroscopic quantum self-trapping in the case, when the initial imbalance between the two condensates exceeds some critical value [88, 89, 75]. Here we will consider these effects applied to the condensates of excitons and polaritons. With respect to the works published on a similar topic [90, 91, 92], the novelty in the reference [72] we will follow in this section, is that we take into account the polarization degree of freedom which gives rise to much richer and original phenomenology.

The system we will consider is a BJJ but the double well-potential is now filled with two weakly linked BECs of exciton-polaritons (excitons) (the Fig. 3.6). We will analyze how the results of previous section apply in the case of exciton-polaritons when we take into account polarization degree of freedom.

3.3.2 The Model

The starting point for the description of the Josephson effects is a model Hamiltonian for interacting bosons with pseudospin, confined in two traps, R and L (the Fig. 3.6). In the basis of circular polarized states $\uparrow, \downarrow$ it reads

$$\widehat{H} = E \sum_{j=L,R;\sigma=\uparrow,\downarrow} \hat{c}^+_{j\sigma}\hat{c}_{j\sigma} + J \sum_{\sigma=\uparrow,\downarrow} \left(\hat{c}^+_{L\sigma}\hat{c}_{R\sigma} + \hat{c}^+_{R\sigma}\hat{c}_{L\sigma}\right) + \Omega \sum_{j=L,R} \left(\hat{c}^+_{j\uparrow}\hat{c}_{j\downarrow} + \hat{c}^+_{j\downarrow}\hat{c}_{j\uparrow}\right) + \frac{U}{2} \sum_{j=L,R;\sigma=\uparrow,\downarrow} \hat{c}^+_{j\sigma}\hat{c}^+_{j\sigma}\hat{c}_{j\sigma}\hat{c}_{j\sigma} \tag{3.45}$$

where the first term corresponds to free particles, the second term describes the spin-conservative tunneling of particles between the two traps, the third term describes the possibly existing anisotropy of the QW in the direction of the structure growth axis [93], anisotropy which is equivalent to the application of an effective in-plane magnetic field able to provoke spin flip processes. The last term of the Hamiltonian corresponds to the interactions between particles (we neglected the interactions between particles situated in different traps and particles having opposite circular polarizations).

The geometry of the trap being known, the parameter J can be estimated as follows:

$$J \approx 4Ve^{-\hbar^{-1}\sqrt{2mV}D}, \tag{3.46}$$

where V is the depth of the trap, D is the distance between the traps. This estimation can be easily obtained by calculating of the energy splitting between the symmetric and the antisymmetric wave functions (expression 3.31) resulting from the coupling between two QWs separated by a distance much greater than the well-width. We assume that V and therefore J are independent of the particle density, which is not exact, since the repulsive interaction leads to the blue shift and to the reduction of the trap effective potential. The effects of the blue shift, which has always been neglected in the consideration of nonlinear Josephson oscillations, will be discussed later, together with the Gross-Pitaevskii equation approach.

The interaction constant is

$$U \approx E_B a_B^2/S, \tag{3.47}$$

with E_B and a_B being the binding energy and Bohr radius of the 2D exciton, S an area of a trap [83].

The spin coupling parameter Ω is not easy to calculate (see ref. [93] for details), but has been measured in the range $50 - 100$ μeV [94, 95].

Using the Heisenberg equations of motion for the operators $\hat{c}_{j\sigma}$

$$i\hbar\frac{d\hat{c}_{j\sigma}}{dt} = [\hat{c}_{j\sigma}, \hat{H}] \tag{3.48}$$

and neglecting the effects of dephasing due to the finite number of the particles, one obtains the following set of four coupled kinetic equations for a condensate order parameter $\psi_{j\sigma} = \langle \hat{c}_{j\sigma} \rangle$:

$$i\hbar \frac{d\psi_{L\sigma}}{dt} = \left(E + U|\psi_{L\sigma}|^2\right)\psi_{L\sigma} - J\psi_{R\sigma} - \Omega\psi_{L,-\sigma} \tag{3.49}$$

$$i\hbar \frac{d\psi_{R\sigma}}{dt} = \left(E + U|\psi_{R\sigma}|^2\right)\psi_{R\sigma} - J\psi_{L\sigma} - \Omega\psi_{R,-\sigma} \tag{3.50}$$

If one of the tunneling parameters J or Ω is zero, the four coupled equations 3.49-3.50 separate into two independent pairs, equivalent to those 3.27 and 3.28 we considered in the section on BJJ .

In the case of the absence of the effective in-plane magnetic field $\Omega = 0$, one has independent coherent tunneling of the condensates with opposite circular polarizations between two traps, completely analogical to the conventional Josephson effect for atomic condensates. For excitons and polaritons this will be referred to as *extrinsic Josephson effect*.

On the other hand, if different traps are uncoupled $J = 0$, but $\Omega \neq 0$ in each of the traps, we have coherent exchange of particles between the condensates with different polarizations. This will be referred to as *intrinsic Josephson effect*. This latter effect can be related with the oscillations of the circular polarization degree which have been observed in the recent years [94] and which have been successfully described within a semi-classical approach based on the description of the polariton pseudospin dynamics, [96].

The nonlinear term plays a crucial role in Josephson dynamics. Once nonlinearity is neglected, equations 3.49 and 3.50 give a well known expression 3.9 for the Josephson current for both extrinsic and intrinsic Josephson effects

$$I_{i,e} = I^0_{i,e} \sin\theta \tag{3.51}$$

where θ is the difference between the phases of the two condensates, $I^0_e = N_T J\hbar^{-1}, I^0_i = N_T \Omega\hbar^{-1}$ with N_T being the total number of particles. In this regime the occupancies of the coupled condensates exhibit harmonic oscillations with periods given by J and Ω for extrinsic and intrinsic Josephson effects respectively. The situation changes drastically if nonlinear terms are taken into account. The oscillations of the occupation numbers become anharmonic, their period depends on N_T [86, 88]. Besides, if the initial imbalance between the occupation numbers of the two coupled condensates exceeds some critical value N_c, the effect of the MQST occurs [88]. In this regime the tunneling between the condensates is suppressed and the particles remain in the state where they have been created as it was recently observed for atomic condensates [76].

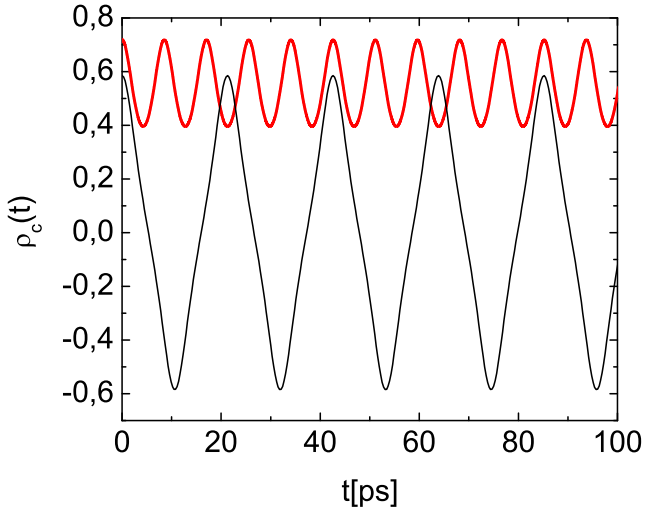

Figure 3.7 | Intrinsic Josephson effects: ρ_c vs time t for the intrinsic Josephson effect $J = 0$ and $\Omega = 50\mu eV$. Blue/dark gray line shows nonlinear oscillations and red/gray lineMQST.

3.3.3 Intrinsic Josephson effect and finite-life time effect

We consider polaritons in a GaAs microcavity. The exciton binding energy is taken as $E_b = 12$ meV and the Bohr radius $a_B = 100$ A. The detuning between the cavity photon and the QWs exciton is zero and the Rabi splitting is taken as 7 meV. We consider either an ideal case of very long lifetime for the polariton, or a more realistic one where it is taken as 16 ps.

The Fig. 3.7 illustrates the intrinsic Josephson effect ($J = 0$). It shows the the time oscillations of the circular polarization degree $\rho_c(t)$

$$\rho_c(t) = \frac{N_\uparrow(t) - N_\downarrow(t)}{N_T} \tag{3.52}$$

for two different initial values $\rho_c(0) = 0.58$ and $\rho_c(0) = 0.71$.$N_{\uparrow,\downarrow}$ denotes the number of particles with spin ↑,↓, respectively. The critical value of ρ_c defined by equation 3.40 (replacing z_c by ρ_{cr}) is 0.63. For $\rho_c(0) < \rho_{cr}$ we have Josephson-like oscillations. Approaching the critical value of polarization degree, oscillations become more and more anharmonic, like in the case of black curve on the Fig. 3.7. Above this critical value regime of MQST establishes (red curve on the Fig. 3.7) and mean value $< \rho_c(t) > \neq 0$. It is characterized by suppression of beats of ρ_c and by the onset of the self-induced Larmor precession which is an oscillation of the linear part of the polarization about the effective magnetic field created by the circular polarization degree [96, 97]. Such dynamical behavior including transition from Josephson oscillations to MQST is a consequence of interaction in the system.

It is an important problem when we discuss exciton-polariton Josephson junction to allow for finite life time of exciton-polaritons. To do this we introduce one dissipative term in pair of equations for polarization dynamics 3.49 and 3.50 of the form $i\hbar\psi_\sigma/2\tau$, where τ

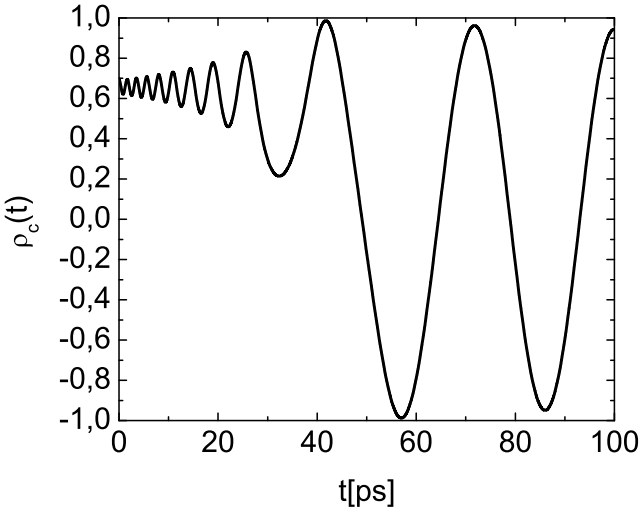

Figure 3.8 | Finite life time effect on intrinsic Josephson effects: $\rho_c(t)$ is shown for finite lifetime $\tau = 16ps$. The other parameters are: $J = 0$ and $\Omega = 50\mu eV$.

is parameter with meaning of life time. The curve 3.8 is calculated considering a pulsed resonant excitation and taking into account the decay of polaritons ($\tau = 16$ ps). At short times, the polarization oscillations are suppressed. However, the decay of the number of particles leads to the increase of the critical value ρ_c and after 40 ps the oscillatory regime is recovered.

The extrinsic Josephson effect takes place between two potential wells. We consider $\Omega = 0$, so that the two circular polarizations are uncoupled. Under the pure circular excitation of one of the coupled wells, time behavior of the normalized population imbalance $z(t)$ coincides with polarization degree we have shown on figures the 3.7 and 3.8. Both linear Josephson oscillations and MQST can be achieved, as well as the transition between the two regimes, when the finite lifetime of particles is taken into account.

3.3.4 Spatial separation of polarization

The Fig. 3.9 shows the more complex and original situation of the dynamics of an elliptically polarized condensate, still assuming $\Omega = 0$ for simplicity. The right potential well is populated at $t = 0$ with a given circular polarization degree ρ_c^R. On the figures 3.9a and 3.9c the two condensates of opposite polarization are oscillating regularly, but with two independent frequencies, which gives a very specific oscillation pattern of the population imbalance (the Fig. 1.2a) and of the circular polarization degree ρ_c^L and ρ_c^R (the Fig. 1.2c) in the left and right well respectively. For the figures 3.9b and 3.9d, the initial imbalance is higher, and the MQST effect occurs for the spin-up component, but not for the spin-down component. In this case, the former remains confined to the initial trap, while the latter exhibits Josephson oscillations between two traps, and the dynamic spatial separation of two circular polarizations thus occurs (the Fig. 3.9d). The Fig. 3.10

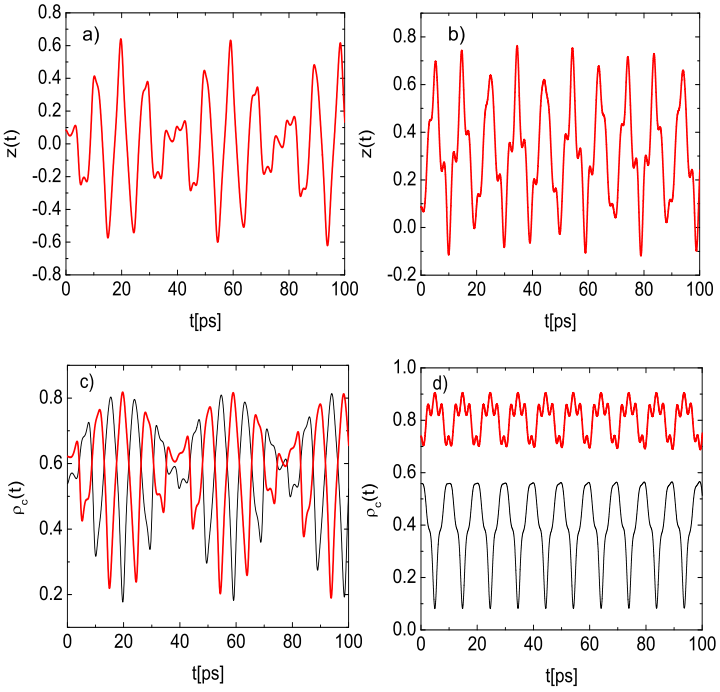

Figure 3.9 | Extrinsic Josephson effect and spatial separation of polarizations: a) Population imbalance for the case of normal Josephson oscillations; b) population imbalance for the case of spatial separation of polarizations; c) ρ_c^L (black) and ρ_c^R (red/gray) without spatial separation of polarizations; and d) ρ_c^L and ρ_c^R for the case of spatial separation of polarizations

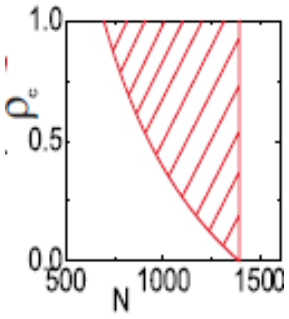

Figure 3.10 | Phase diagram for polarization separation condition versus initial polarization degree ρ_c and the number of particles N_T

summarizes the range of parameters (ρ_c and N_T) where the effect of spatial separation of polarization occurs.

To illustrate the spatial separation of polarizations we used the description of the spinor polariton condensate by a system of coupled Gross-Pitaevskii equations for excitons and Schrödinger-like equations for photons [85], which account for both realistic trapping potential and inter-particle interactions,

$$i\hbar\frac{\partial\psi_\sigma(\mathbf{r},t)}{\partial t} = \left(-\frac{\hbar^2}{2m_e x}\Delta + V(\mathbf{r}) + \alpha|\psi_\sigma(\mathbf{r},t)|^2\right)\psi_\sigma(\mathbf{r},t) + V_R\chi_\sigma(\mathbf{r},t) \quad (3.53)$$

$$i\hbar\frac{\partial\chi_\sigma(\mathbf{r},t)}{\partial t} = -\frac{\hbar^2}{2m_p h}\Delta\chi_\sigma(\mathbf{r},t) + V_R\psi_\sigma(\mathbf{r},t) + P_\sigma(\mathbf{r},t) \quad (3.54)$$

where $\psi_\sigma(\mathbf{r},t)$ is the exciton wavefunction with circular polarization σ, $\chi_\sigma(\mathbf{r},t)$ is the photon wavefunction with the same polarisation, V_R is the Rabi splitting, $V(\mathbf{r})$ is an external potential of the two traps which we introduce only for excitons, as in [80], the parameter α is the interaction constant. The equation 3.53 and 3.54 is an obvious generalization of the system of the equations 3.49 and 3.50. The imaginary part of energy allows to take into account the finite particle lifetime, and the pumping is introduced as a separate term $P_\sigma(\mathbf{r},t)$ for photonic component. We have considered a realistic trapping potential for polaritons with a barrier of 1 meV height and 1 μm width between the two minima. For such barrier, a tunneling period of about 10 ps is expected from the approximative formula. From simulations, we find a period of 25 ps for this potential. However, in non-linear regime the period of oscillations can be strongly reduced, which should allow experimental observation of the effects under study for exciton-polaritons with a lifetime of 16 ps.

The figure 3.11 shows the spatial distribution of the two circular-polarized components σ^+ and σ^-. The latter is plotted with negative sign, in order to allow direct comparison of both distributions. At $t = 0$ (the Fig. 3.11a), the maxima of the two polarizations coincide in real space, whereas at some later moment of time $t = 6$ ps (the Fig. 3.11b) the maxima are separated because of the different periods of oscillations for two components.

3.3.5 Conclusions

We analyzed the Josephson-type effects in condensates of spinor excitons and polaritons. We distinguish the extrinsic effect related to coherent tunneling of particles with the same spin between two spatially separated potential traps and the intrinsic effect related to tunneling between different spinor components of the condensate within the same trap. The Josephson effects in the nonlinear regime leads to nontrivial polarization dynamics and produce a spontaneous separation of the condensates with opposite polarizations in the real space.

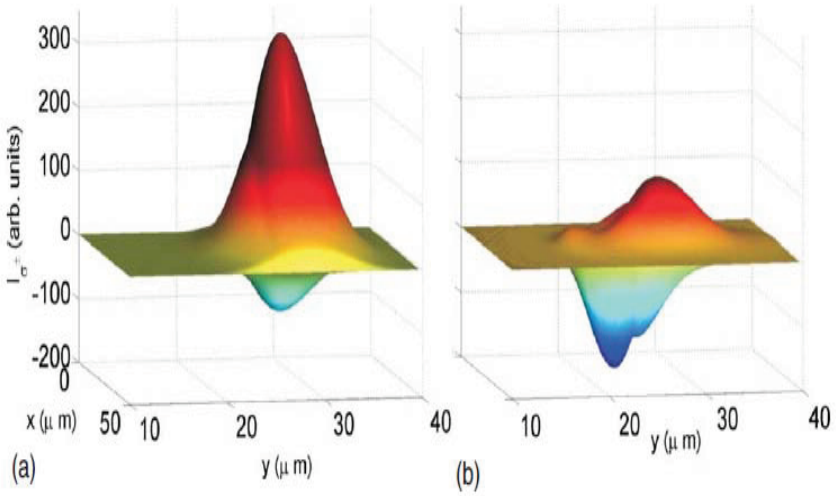

Figure 3.11 | Spatial images showing the intensity of emission for two circular-polarized components. The σ_- component is plotted with negative sign: a) No spatial separation; b)Spatial separation of polarization during nonlinear oscillations.

The Josephson oscillations of polaritons condensates created by resonant excitation is experimentally achievable, but it requires very high quality samples and a good design of the in-plane potential. As for the bare excitons, they posses a longer lifetime, but their heavier mass makes the period of oscillations longer, and, in the end, not easier to observe. Increasing the particle density leads to a blue shift of the energy which gives rise to two competing effects: the MQST, but also the decrease of the effective height of the barrier, which increases the tunneling constant. This change makes decrease the period of the Josephson oscillations and may eventually yield a complete delocalization of the condensate [98]. It reduces the possibility to observe MQST, which requires high occupation numbers in the condensates and which, to be observable requires deep potential traps with steep walls. The Josephson coupling of two exciton-polariton condensates with stochastic phases has been recently considered theoretically (Phys. Rev. B 81, 235315 (2010))

Among other interesting effects which appear when the polarization of polaritons is taken into account, we can cite the chaotic Josephson oscillations, appearing in the system described in this chapter (thanks to its sufficient complexity) under quasi-resonant pumping. These oscillations promise original applications in the domain of chaotic cryp-

tography [99]. In the reference [100] the Josephson type coupling of two exciton-polariton condensates with stochastic phases has been recently considered theoretically.

Chapter 4

Berry phase of exciton-polaritons

In the following chapter we will study in detail the Berry phase of exciton-polaritons. It is a quantum phase effect occurring in mesoscopic systems for a transport on a closed path, theoretically predicted by [101]. It is a quite general concept for a large class of quantum systems, just to mention for example the measurement of Berry phase using nuclear magnetic resonance (NMR) in Ref. [102] under magnetic field precessing about z-axis. To analyze Berry phase of polaritons we will consider in what follows the effects of an external magnetic field applied perpendicularly on a polariton circuit already possessing an (effective) extra magnetic field due to TE-TM splitting of polaritons. Since the well-known Aharonov-Bohm effect for electrons [103] can be understood as an Berry's phase effect, we will start with electrons in an Aharonov-Bohm circuit. This analogy will be used to introduce Berry phase. We will give an overview of TE-TM splitting for polariton based on review before we finally analyze how it can serve for a novel type of polariton based interferometry.

Contents

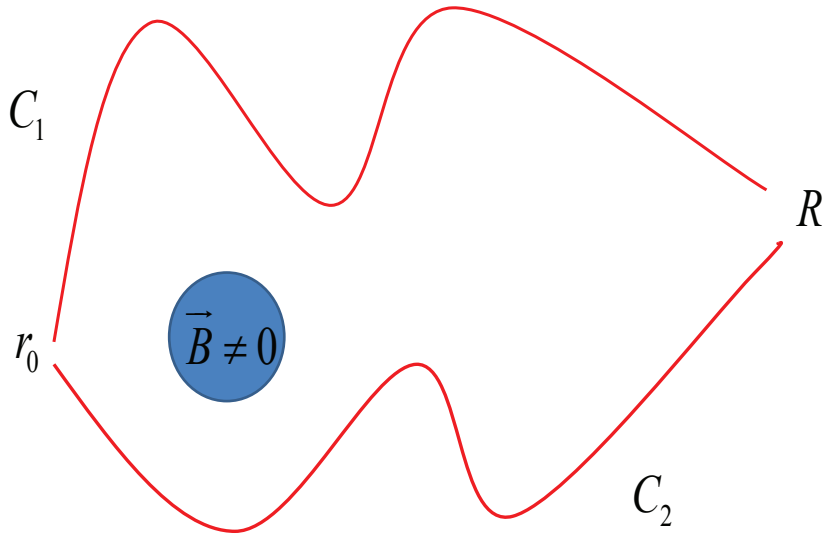

Figure 4.1 | Scheme of electrons propagating in a circuit with external magnetic field $\vec{B}$ enclosed by paths C_1 and C_2. r_0 and R denotes entrance and exit points, respectively.

4.1 Aharonov-Bohm phase

We will consider adiabatic propagation of electrons through the arms C_1 and C_2 of closed circuit as shown on the Fig. 4.1. Electrons are introduced at the entrance point r_0 and after the propagation, the electron beam is detected at the exit denoted by R. We are interested to know how an internal magnetic flux applied perpendicular to the ring, which we place in x-y plane letting magnetic field $\vec{B} = B\vec{e}_z$, influences the properties of electrons detected in R. To see this we will assume that in absence of magnetic field the electrons are described by a Hamiltonian

$$H_0 = \frac{\hbar^2 k^2}{2m_e} \tag{4.1}$$

where k is momentum and m_e is electron mass. Schrödinger equation with operator 4.1 reads

$$i\hbar \frac{\partial |\psi_0\rangle}{\partial t} = H_0 |\psi_0\rangle \tag{4.2}$$

where with $|\psi_0\rangle$ we write eigenstate, associating index zero to eigenstate in absence of magnetic field $B = 0$. In general, the presence of electromagnetic field $B \neq 0$ alters the momentum by relation

$$\vec{k} \to \vec{k} - \frac{e}{\hbar}\vec{A} \tag{4.3}$$

where $\vec{A}$ is vector potential of electromagnetic field. Therefore for $B \neq 0$ we have to modified H_0 and write

$$H = \frac{\hbar^2(\vec{k} - \frac{e}{\hbar}\vec{A})^2}{2m_e} \tag{4.4}$$

which also satisfies Schrödinger equation 4.2 but with a new eigenstates $|\psi>$.

We are interested in adiabatic evolution and we include the vector potential due to $\vec{B}$-field trough the contour as an extra phase phase factor φ in the new wave function,

$$|\psi\rangle = e^{i\varphi}\,|\psi_0\rangle \tag{4.5}$$

which is given by integral

$$\varphi = \frac{e}{\hbar}\int_\gamma \vec{A}(\vec{r})\vec{dl} \tag{4.6}$$

where the γ is a loop and $\vec{dl}$ being its vector element. Strictly speaking, the integral is only defined for closed contours, whereas for open contours the potential $\vec{A}$ is ambiguous. However, we can always close a trajectory with one curve orthogonal to $\vec{A}(\vec{r})$ and by this definition it does not influence the phase [104]. In this way we defined the phase in each point of some trajectory with respect to a chosen phase at some fixed point.

The infinitesimal phase gain being $d\varphi \to \overrightarrow{k}\,\overrightarrow{dl}$ the last relation follows simply from the replacement 4.3. For an adiabatic transport the presence of magnetic field influences only the phase of the wave function. The phase itself is not quantum mechanical observable and cannot be measured, but one can measure the phase difference.

To observe the Aharonov-Bohm (AB) phase, we measure the phase difference of the electrons propagating propagating on arms C_1 and C_2: entering the AB circuit at point r_0 and and leaving it at point R. The phases gain on lines C_1 and C_2 are

$$C_1: \quad \varphi_1 = \frac{e}{\hbar}\int\limits_{C_1} \overrightarrow{A}(\overrightarrow{r})d\,\overrightarrow{l} \tag{4.7}$$

$$C_2: \quad \varphi_2 = \frac{e}{\hbar}\int\limits_{C_2} \overrightarrow{A}(\overrightarrow{r})d\,\overrightarrow{l}\,. \tag{4.8}$$

Thus the phase difference $\Delta\varphi = \varphi_1 - \varphi_2$ of the wave traveling in in arms at the entrance point is

$$\Delta\varphi = \frac{e}{\hbar}\int\limits_{C_1} \overrightarrow{A}(\overrightarrow{r})d\,\overrightarrow{l} - \frac{e}{\hbar}\int\limits_{C_2} \overrightarrow{A}(\overrightarrow{r})d\,\overrightarrow{l} = \frac{e}{\hbar}\int\limits_{C_1} \overrightarrow{A}(\overrightarrow{r})d\,\overrightarrow{l} + \frac{e}{\hbar}\int\limits_{-C_2} \overrightarrow{A}(\overrightarrow{r})d\,\overrightarrow{l} \tag{4.9}$$

where in the last equality we change the direction of integration and in the same time direction of contour $C_2 \to -C_2$. Bearing in mind that $\overrightarrow{B} = curl\,\overrightarrow{A}$ and transforming a line in a surface integral we obtain

$$\Delta\varphi = \frac{e}{\hbar}\oint \overrightarrow{A}(\overrightarrow{r})d\,\overrightarrow{l} = \frac{e}{\hbar}\int\int_\Omega \overrightarrow{B}(\overrightarrow{r})d\vec{S} \tag{4.10}$$

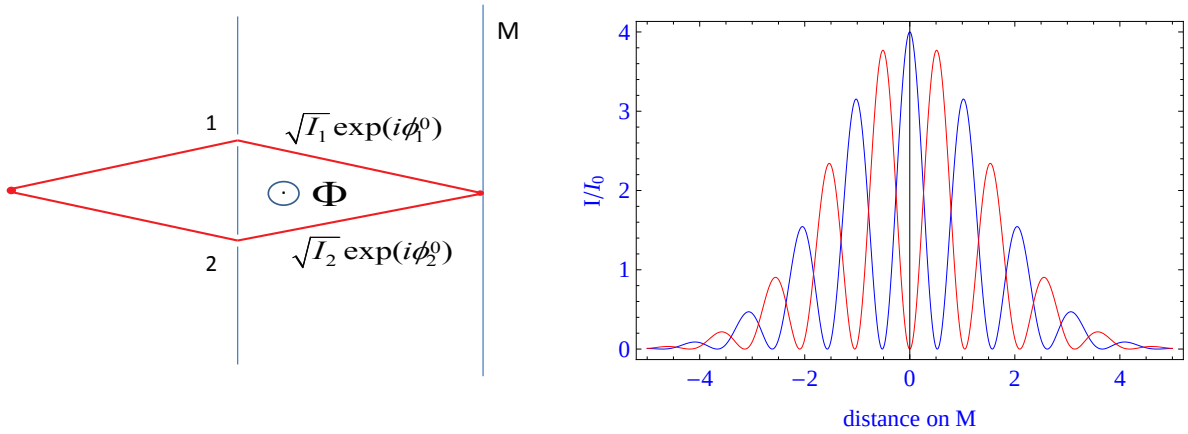

Figure 4.2 | Illustration of Aharonov-Bohm effect. LEFT: Experimental scheme for double-slit set-up with solenoid. RIGHT: Normalized intensity for $\Phi = 0$ (blue curve) and $\Phi \neq 0$ (red curve)

where $d\vec{S}$ is the vector of surface Ω containing contour C. Then for AB phase we have

$$\Delta\varphi = 2\pi\frac{\Phi}{\Phi_0}. \tag{4.11}$$

The value $\Phi_0 = e/\hbar$ is called flux quantum and Φ is magnetic flux.

According to the last formula, we can tune the phase $\Delta\varphi$ difference by changing the magnetic flux Φ through the contour. An example, very well-studied, consists of placing a solenoid between two slits in a set-up similar to those of famous Young experiment. The magnetic flux is induced by this solenoid and we can change it by controlling the current. The electrons (electron) passing through slits 1 and 2, like it is shown on the Fig. 4.2(left) arrive(s) to each point of M with the phase difference given by 4.10 or equally by 4.11. This demonstrates how one can modify the interference picture on M changing the current in solenoid (right).

For two coherent beams described by wave functions $\psi_{1,2} = \sqrt{I_{1,2}}exp(i\phi_{1,2}^{(0)})$, the total intensity reads

$$I = I_1 + I_2 + 2\sqrt{I_1 I_2}\cos\left(\Delta\phi^0 + 2\pi\frac{\Phi}{\Phi_0}\right) \tag{4.12}$$

and by means of this formula AB interferometer can be also use to measure the flux of magnetic field Φ - a classical variable - using a quantum effect. Such kind of metrology is named quantum metrology.

Being defined just by the integral parameter Φ,i.e. by one global quantity, the AB phase does not depend on local properties of the system and different paths can have equal $\Delta\phi$. Effects like this are called geometrical effects and the AB phase falls to class of geometrical (topological) phases. Aharonov-Bohm effect is very often cited as an evidence that vector potential $\vec{A}$, an auxiliary quantity in classical electrodynamics, contains physical sense as the AB phase 4.10 can be non-zero even in the case when on particle

trajectory magnetic field vanishes $\vec{B} = 0$. Magnetic field is localized inside the contour and 'non-locally', via the $\vec{A}$-field, interacts with the moving electrons.

4.2 TE-TM splitting, Rashba spin-orbit interaction and devices

We have already briefly discussed the effect of splitting of longitudinal and transverse polariton modes in the frame of intrinsic Josephson effect. As magnetic field plays the crucial role in AB effect for electrons, which we have taken to represent in some sense hole class of geometrical effects where certainly falls and Berry phase effect which we want to consider, it is very instructive to analyze an effective magnetic field in the exciton-polariton system which appears we will see due to longitudinal-transverse, i.e. TE-TM splitting.

In order to compare the Berry phase effect for exciton-polaritons with the Berry phase in a system with electrons, where another kind of effective magnetic field is present due to Rashba Spin Orbit Interaction (SOI) here we are going to detail in Rashba SOI and TE-TM polarization splitting.

These two effects concerning spin and pseudospin respectively are of particular importance in mesoscopic physics, where the problem of spin dynamics is one of the most interesting. The investigations in this field are stimulated by the possibility of creation of nanodevices where the spins of the single particles could be objects of the precise manipulation and control. The first device of this type, namely spin transistor, was proposed in early 90ies in the pioneer work of Datta and Das [105], who used an analogy between a precession of an electron spin provided by Rashba spin-orbit interaction (SOI) and rotation of a polarization plane of light in optically anisotropic media.

However, the experimental realization of the Datta and Das spin transistor turned out to be extremely complicated, due to the extremely low efficiency of the spin injection from ferromagnetic to semiconductor materials. It was thus proposed to use mesoscopic gated Aharonov-Bohm rings as a possible basis of various spintronic devices such as spin transistors [106, 107], spin filters [108, 109, 110], and quantum splitters [110]. The configuration which is usually considered, consists of a quantum ring with two symmetrically situated electrodes. The conductance of such a structure depends both on the magnetic and electric fields applied perpendicular to the structure's interface. The former provides the AB phaseshift between the waves propagating in the clockwise and anticlockwise directions thus resulting in the oscillations of the conductance.

The electric field applied perpendicular to the plane of the ring also affects the conductance. It has a double effect. First, it shifts the subband's bottom inside the ring thus providing the change of the carrier's wavenumber. Therefore the conductance of

the system can exhibit the oscillations in the complete analogy to those observed in the Fabry- Perot resonator. Second, it lifts the symmetry of the quantum well in the direction of the structure growth axis thereby inducing the Rashba SOI inside the ring that is characterised by the SOI coupling parameter. The latter depends linearly on the gate voltage and creates the dynamical phaseshift between the waves propagating within the ring, consisting of Aharonov - Casher (AC) phaseshift arising from different values of the wavenumbers for the waves propagating in opposite directions [107, 111] and a Berry phase (geometric phase) term provided by an adiabatic evolution of the electron spin in the inhomogenious effective magnetic field created by Rashba SOI and external magnetic field perpendicular to a structure's interface[106]. As a result, the conductance of the mesoscopic ring exhibits oscillations [112] as a function of the perpendicular electric field . We should mention that one important consequence of the absence of the AC phase for polaritons is the absence of the weak antilocalization for them [113].

It was recently proposed that in the domain of mesoscopic optics the controllable manipulation of the spin of excitons and exciton-polaritons can provide a basis for the construction of optoelectronic devices of the new generation, called spinoptronic devices [114]. The first element of this type, polarization- controlled optical gate, was recently realized experimentally [115].

An important property of the cavity polaritons is their (pseudo)spin [116], inherited from the spins of the QW exciton and cavity photon and directly connected with the polarization of the emitted photons as we have seen in the Chapter 1 of this thesis. The control of the spin of cavity polaritons thus opens a possibility of tuning the polarization of the emission which can be used in optical information transfer, for example.

The analog of a Rashba SOI in microcavities is provided by a longitudinal-transverse splitting (TE-TM splitting) of the polariton mode. It is well known that due to the long-range exchange interaction between the electron and a hole for excitons having non-zero in-plane wave-vectors the states with dipole moment oriented along and perpendicular to the wavevector are slightly different in energy [117]. In microcavities, splitting of longitudinal and transverse polariton states is amplified due to the exciton coupling with the cavity mode (which is also split in TE- and TM- light polarizations) [118] and can reach values of about $\approx 1meV$.

TE-TM splitting results in the appearance of the effective magnetic field provoking a rotation of polariton spin. It is oriented in-plane of the microcavity and makes a double angle with X-axis in the reciprocal space,

$$\vec{B}_{LT}(k) \sim \mathbf{e}_x \cos(2\phi) + \mathbf{e}_y \sin(2\phi) \tag{4.13}$$

This is different from the orientation of the effective magnetic field provided by Rashba SOI (see the Fig. 4.3), which makes a single angle with y-axis,

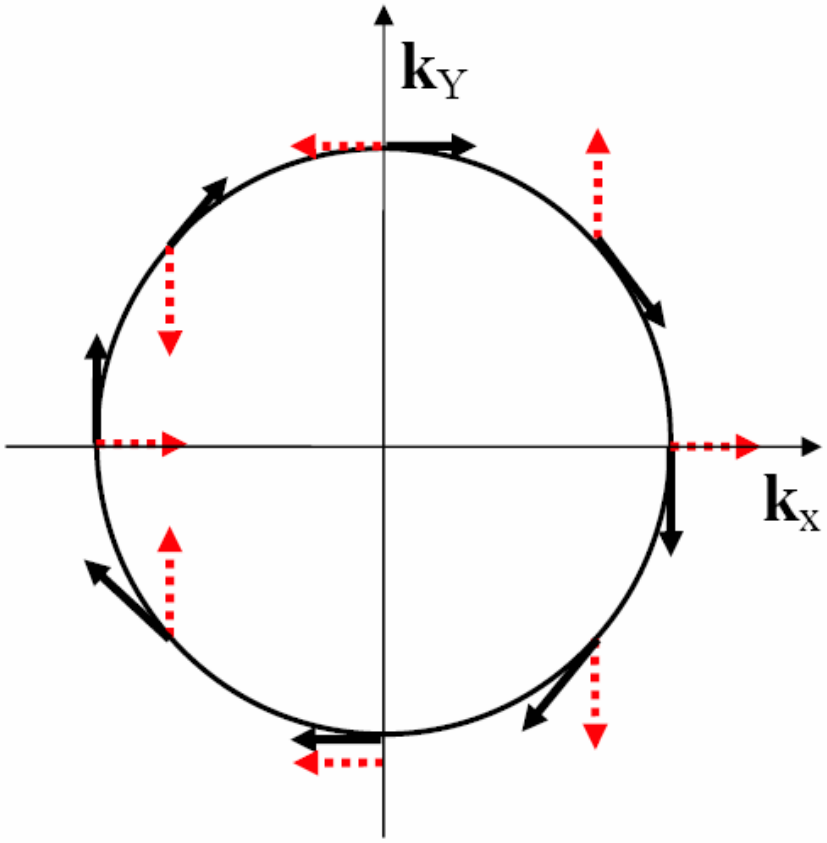

Figure 4.3 | Orientation of the effective magnetic fields provided by Rashba SOI (black) and TE-TM (red) splitting in the reciprocal space

$$\vec{B}_{SOI}(k) \sim \mathbf{e}_x \sin(\phi) - \mathbf{e}_y \cos(\phi) \tag{4.14}$$

This peculiar orientation of $\vec{B}_{LT}$ results in different interference patterns for electrons and polaritons in ring interferometers, leading in particular to an absence of AC phase for polaritons as we shall see later on.

4.3 Berry phase

When an initial state of a quantum system after slow evolution through the set of intermediate states comes to some final state which coincides with the initial one, the system obtains a quantum adiabatic geometrical phase, known as the Berry phase. It is very similar to AB phase which occurs for charged particles moving along the closed trajectory due to enclosed magnetic field. The main difference is that the Berry phase is the result of directional change of local magnetic field for the same type of evolution. An AB phase, as we pointed out in the previous part, can be zero along the AB contour.

Let's consider like in the Berry paper [101](but adapting the notation to our purpose) one system whose Hamiltonian depends on some parameter $\vec{B}$: $H(\vec{B})$. We suppose that spectrum of $H(\vec{B})$ has at least one discrete and non-degenerate eigenvalue

$$H(\vec{B})|\Psi_i(\vec{B})>=E_i(\vec{B})|\Psi_i(\vec{B})> \tag{4.15}$$

where the index i counts those states. The eigenvectors $|\Psi_i(\vec{B})>$ and eigenvalues $E_i(\vec{B})|$ are dependent on parameter $\vec{B}$ as it is the Hamiltonian 4.15. The vector $\vec{B}$ is some function of time $\vec{B}=\vec{B}(t)$ evolving adiabatically with it, around a loop such that

$$\vec{B}(0)=\vec{B}(T), \tag{4.16}$$

where the time T refers to the final time of cyclic evolution. Here we will concentrate on this case as it was considered in the original paper on the Berry phase [101], although there exist more general approaches on the same subject including analysis of non-adiabatic evolution [119], degenerate states [120], and even partial cycles [121, 122]. The adiabatic theorem (or Ehrenfest theorem) [123] states that the system will be in instant t from interval $[0,T]$ in the state

$$\exp\left(i\phi(t)\right)|\Psi_i(\vec{B}(t))> \tag{4.17}$$

if it has been initially prepared in the eigenstate $\Psi_i(\vec{B}(0))>$ of the Hamiltonian $H(\vec{B}(0))$. The initial eigenstates which depend on the parameter $\vec{B}$ just gain an extra phase $\phi(t)$ instead of jumping into another eigenstate for non-adiabatic cyclic evolution. The state 4.17 satisfies time-dependent Schrödinger equation

$$i\hbar\frac{d}{dt}\exp\left(i\phi(t)\right)|\Psi_i(\vec{B}(t))>=H(\vec{B}(t))\exp\left(i\phi(t)\right)|\Psi_i(\vec{B}(t))>. \tag{4.18}$$

After projecting it on the state $\exp\left(i\phi(t)\right)|\Psi_i(\vec{B}(t))>$ it reads

$$\frac{d}{dt}\phi(t)=i<\Psi_i(\vec{B})|\nabla_{\vec{B}}|\Psi_i(\vec{B})>\frac{d\vec{B}}{dt}-\hbar^{-1}E_i(\vec{B}). \tag{4.19}$$

From here the phase $\phi(t)$ is

$$\phi(t)=i\int_{\vec{B}(0)}^{\vec{B}(t)}<\Psi_i(\vec{B})|\nabla_{\vec{B}}|\Psi_i(\vec{B})>d\vec{B}-\hbar^{-1}\int_0^t E_i(\vec{B})d\tau. \tag{4.20}$$

defined to an arbitrary constant $\phi(0)$.

The last part in the formula 4.20 is usual dynamical phase. The first term on the RHS of the same equation is the phase acquired due to the change of the parameter $\vec{B}$ along the trajectory. As it is itself a function of time, it can be written in the form

$$\phi_B(t)=i\int_0^t<\Psi_i(\vec{B}(\tau))|\frac{d}{d\tau}|\Psi_i(\vec{B}(\tau))>d\tau. \tag{4.21}$$

The integrand

$$\vec{A}_B = i < \Psi_i(\vec{B})|\nabla_{\vec{B}}|\Psi_i(\vec{B}) > \tag{4.22}$$

is known as Berry connection.

We choose that the system evolves cyclically by paths C_1 and C_2 (same like in the Fig. 4.1) where we fix initial time $t = 0$ in the point r_o and final $t = T$ in the point R such that for both paths condition 4.16 is satisfied. Using the same technique as in derivation of AB phase in formulae 4.7-4.10 we can write the loop integral

$$\varphi_B(C) = i \oint_C \vec{A}_B d\vec{B} \tag{4.23}$$

where again $C = C_1 - C_2$ and $\varphi_B(C) = \phi_{B,1}(T) - \phi_{B,2}(T)$. The last expression is Berry phase. It is formally equal to formula for AB phaseshift 4.10 except that the circulation of the vector potential is now replaced by circulation of Berry connection in the parameter space - $\vec{B}$.

The classical analogue of the Berry phase is anholonomy angle. It occurs for cyclic transport of a vector on some non-flat surface, during which the vector stays in tangent plane without being rotated around the surface normal (parallel transport). After completion of the cycle C $(1 \to 2 \to 3 \to 1)$ the initial vector orientation has been rotated by an angle ϕ_C [124], called anholonomy angle. The initial and final vector $\vec{\tau}$ do not coincide at position 1 (the Fig. 4.4). The well-known example of dynamical system which possesses such behavior is the rotation of the oscillation plane of the Foucault's pendulum or gyroscope, whose rotation axis is transported on the closed contour.

The anholonomy angle for the vector transported on the closed surface on the sphere equals the solid angle Ω described by it and can be calculated by simple integral

$$\Omega(C) = \int_{\phi_{min}}^{\phi_{max}} d\phi \int_{\theta_{min}}^{\theta_{max}} \sin\theta d\theta \tag{4.24}$$

which for a vector circumscribing the full cycle in x-y plane $\phi \in [0, 2\pi]$ reads

$$\Omega(C) = \pm 2\pi(1 - \cos\theta_{max}) \tag{4.25}$$

where the sign depends on the direction of motion along the contour C. The Berry phase for particles of spin S is related to the solid angle [106] described by (pseudo)spin by

$$\varphi_B(C) = -S\Omega(C), \tag{4.26}$$

i.e. it is half the solid angle for particles of spin 1/2 and the full solid angle for the particles of (pseudo)spin 1.

To summarize this comparison between AB and Berry effect we point out that AB effect is a purely quantum effect for which a classical analogue like aholonomy angle for

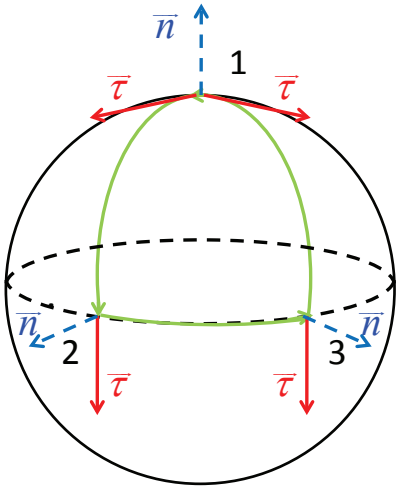

Figure 4.4 | parallel transport of the vector $\vec{t}$ on closed cycle C : $1 \to 2 \to 3 \to 1$ on sphere. The sphere normal is denoted with $\vec{n}$

the Berry phase does not exist. Furthermore, AB phase has a non-local character while the directional change of parameter vector is a local property essential for Berry phase. From the experimental point of view, Berry phase observation usually needs much higher values of magnetic fields. An AB phase shift can be obtained at lower values of it.

4.3.1 Berry phase based interferometry with polaritons

The system we are going to consider is an optical ring interferometer placed in the external magnetic field perpendicular to its interface 4.5. The polaritons are injected in the ingoing lead by a laser beam, propagate in the ring and finally the intensity into the outgoing lead is detected. To make the polaritons propagate along the desirable path, one needs to engineer the corresponding confinement potential, which can be achieved by variation of the cavity width [125], putting metallic stripes on the surface of the cavity [126] or applying a stress [127]. The other option is to produce the waveguide structure by lithography, as in the case of micropillar cavities [128]. The narrow waveguide for polaritons has its own TE-TM splitting, which is inversely proportional to waveguide dimensions [57] and which can dominate over the cavity splitting (for a waveguide of 1 μ m width this splitting can be as high as 1$\to$2 meV [129]).

To calculate the intensity of the outgoing beam, we consider the polariton states inside the $1D$ ring, and take into account the TE-TM splitting (of both origins) and the Zeeman splitting, the latter provided by an external magnetic field perpendicular to the cavity plane. With such geometry the averaging of the full Hamiltonian to $1D$ is valid since

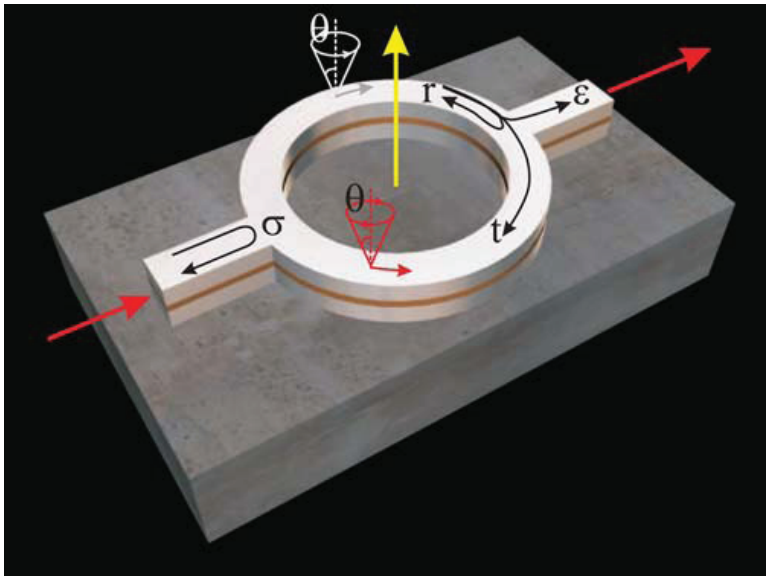

Figure 4.5 | Possible design of the microcavity waveguide. Letters mark the scattering amplitudes for particle propagation. Ellipses show the rotation of the pseudospin. Gray (red) arrows show the direction of light propagation; light gray (yellow) arrow shows the direction of the magnetic field

the energy splitting between two successive confined TE modes is much larger than the TE-TM splitting. The corresponding Hamiltonian in the basis of circular polarized states reads

$$\hat{H} = \begin{pmatrix} H_0(\hat{k}) + \frac{\Delta_Z(\hat{B})}{2} & \frac{1}{2}[e^{-2i\phi}, \Delta_{LT}(\hat{k})]_+ \\ \frac{1}{2}[e^{2i\phi}, \Delta_{LT}(\hat{k})]_+ & H_0(\hat{k}) - \frac{\Delta_Z(\hat{B})}{2} \end{pmatrix} \tag{4.27}$$

where $\hat{k} = -ia^{-1}d/d\phi$, a is a radius of a ring $H_0(\hat{k})$ is a bare polariton dispersion, $\Delta_{LT}(\hat{k})$ is a longitudinal-transverse splitting, $\Delta_Z(\hat{B})$ is a Zeeman splitting provided by a magnetic field perpendicular to a structure's interface.

In our further consideration we use an effective mass approximation

$$H_0(\hat{k}) = \hbar^2\hat{k}^2/2m_{eff} \tag{4.28}$$

and assume the longitudinal-transverse splitting to be k-independent in the region of wave numbers under study: $\Delta_{LT}(\hat{k}) = \Delta_{LT}$. The off-diagonal factors $e^{\pm 2i\phi}$ comes from double ϕ-dependance of TE-TM splitting for polaritons (see expression 4.13). For electrons

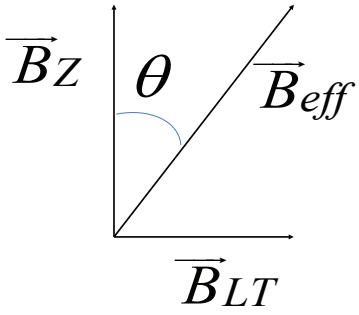

Figure 4.6 | Effective magnetic field $\vec{B}_{eff}$ formed by field due to LT splitting $\vec{B}_{LT}$ and Zeeman splitting $\vec{B}_Z$.θ is the angle which effective magnetic field makes with z-axis.

propagating on a ring one has a single angle dependance due Rashba SOI [130, 131]. The solution of the Schrödinger equation with Hamiltonian 4.27 can be expressed as

$$\Psi_+(\phi) = \frac{1}{\sqrt{1+\xi^2}} \begin{pmatrix} \xi e^{+i\phi} \\ e^{-i\phi} \end{pmatrix} e^{ik_+ a\phi} \tag{4.29}$$

$$\Psi_-(\phi) = \frac{1}{\sqrt{1+\xi^2}} \begin{pmatrix} -e^{+i\phi} \\ \xi e^{-i\phi} \end{pmatrix} e^{ik_- a\phi} \tag{4.30}$$

where the normalization factor reads

$$\xi = \frac{\Delta_{LT}/(2\Delta_Z)}{1+\sqrt{(\Delta_{LT}/(2\Delta_Z))^2+1}}. \tag{4.31}$$

The wavenumbers $k_\pm$ can be straightforwardly found from the characteristic equation of the Hamiltonian

$$\left[H_0(k+a^{-1}) + \frac{\Delta_Z}{2} - E\right]\left[H_0(k-a^{-1}) - \frac{\Delta_Z}{2} - E\right] - \frac{\Delta_{LT}^2}{4} = 0 \tag{4.32}$$

where E is a polariton's energy.

Within the effective mass approximation and neglecting the curvature of the ring ($a >> k^{-1}$) the solution of this equation reads

$$k_\pm = \frac{2m_{eff}E}{\hbar^2} \pm \frac{2m_{eff}}{\hbar^2}\sqrt{\Delta_{LT}^2+\Delta_Z^2}. \tag{4.33}$$

The eigenstates of the Hamiltonian 4.27, as it follows from equations 4.29 and 4.30 are elliptically polarized. Their pseudospin makes an angle θ with z-axis:

$$\arctan\theta = \frac{\Delta_{LT}}{\Delta_Z}, \tag{4.34}$$

following direction of effective magnetic field B_{eff} formed by TE-TM effective magnetic field B_{LT} and magnetic field perpendicular to plane of ring waveguide B_Z (the Fig. 4.6).

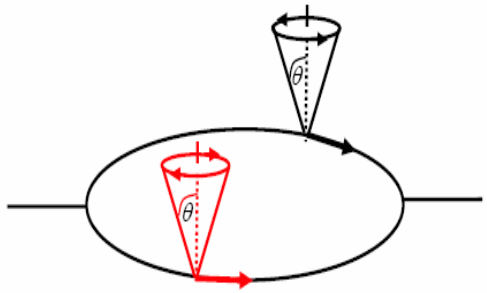

Figure 4.7 | Rotation of the pseudospin of polaritons propagating along the arms of the ring. For clockwise and anticlockwise propagation the rotation direction of the in-plane components of the pseudospin is different

This angle depends on the ratio of an intensity of the LT splitting characterized by a parameter Δ_{LT} and the Zeeman splitting $\Delta_Z(B)$. If

1) $\Delta_{LT} \ll \Delta_Z(B)$ or equivalently $\xi \to 0$ and according 4.27,4.28 the polarization is linear. The angle θ is zero for weak Zeeman splitting. $(\theta = 0)$.

2) $\Delta_{LT} \gg \Delta_Z(B)$ in opposite limit $(\xi \to \infty)$,i.e.for strong LT splitting, and polarization changes to circular for which $(\theta = \pi/2)$.

Now let us consider the intensity of the outgoing beam for a given intensity of the incoming beam. First, let us note that the state of the incoming beam Ψ_{in} can be decomposed by eigenstates of a Hamiltonian 4.27 states in the entrance point (i.e. for $\phi = 0$)

$$\Psi_{in} = \frac{1}{\sqrt{1+|\xi|^2}} \left[A^+_{in} \begin{pmatrix} \xi \\ 1 \end{pmatrix} + A^-_{in} \begin{pmatrix} -1 \\ \xi \end{pmatrix} \right] \tag{4.35}$$

Analogically, the state of the outcoming beam can be also decomposed by states 4.27 and 4.28, now at $\phi = \pi$

$$\Psi_{out} = \frac{1}{\sqrt{1+|\xi|^2}} \left[A^+_{out} \begin{pmatrix} \xi \\ 1 \end{pmatrix} + A^-_{out} \begin{pmatrix} -1 \\ \xi \end{pmatrix} \right]. \tag{4.36}$$

The outgoing amplitudes can $A^{\pm}_{out}$ be found as a sum of the all terms corresponding to the propagation of the particle between the ingoing and outgoing leads.

For a given pseudospin orientation the waves traveling in a clockwise and anticlockwise direction obtain a different Berry phase. This one can check inspecting the loop integral 4.23 and changing the contour orientation. Indeed, the direction of the effective magnetic field consisting of the in-plane TE-TM field and z-directed real field changes along the polariton's trajectory and follows a cone-shaped path (see Fig. 4.7). In the adiabatic approximation the pseudospin of a polariton follows the direction of this field and corresponding geometric phase can be found from the expression 4.26 putting $S = 1$.

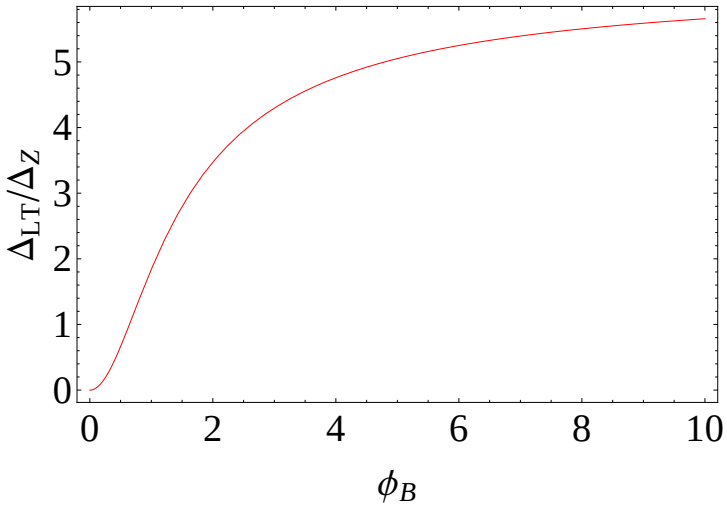

Figure 4.8 | Dependance of Berry phase ϕ_B (clockwise direction) on LT to Zeeman splitting ratio Δ_{LT}/Δ_Z

The Berry phase is the full solid angle Ω which describes pseudospin following parameter $\vec{B}_{eff}$. As from the Fig. 4.6

$$\cos\theta = \frac{\Delta_Z}{\sqrt{\Delta_Z^2 + \Delta_{LT}^2}} \tag{4.37}$$

where we changed notation from $\theta_{max} \to \theta$ in corresponding formula 4.25, the Berry phase reads

$$\phi_B = \pm 2\pi \left(1 - \frac{\Delta_Z}{\sqrt{\Delta_Z^2 + \Delta_{LT}^2}}\right) \tag{4.38}$$

where the sign depends on direction of propagation. One sees (4.8) that it depends on the LT and Zeeman splittings and changes from zero for $\Delta_{LT} \ll \Delta_Z$ to 2π for $\Delta_{LT} \gg \Delta_Z$. It differs by a factor of 2 (coming from the equation 4.27) from geometric phase for the electrons in gated AB ring with Rashba SOI.

Considering the processes with no more than one round trip inside the ring only, one has for outgoing amplitudes

$$A_{out}^{\pm} = A_{in}^{\pm}\epsilon^2 e^{-T/2\tau} e^{i\pi k_{\pm} a} \left[\left(1 + r^2 e^{-T/\tau} e^{2i\pi k_{\pm} a}\right) cos(2\phi_B) + t^2 e^{-T/\tau} e^{2i\pi k_{\pm} a} cos(6\phi_B)\right] \tag{4.39}$$

where τ is the polariton lifetime,

$$T = \pi a \sqrt{m_{eff}}/\sqrt{2E} \tag{4.40}$$

being the time of a propagation from ingoing to outgoing lead. ϵ is an amplitude of the probability for a polariton traveling along one of the arms of the ring to quit the ring in the conjunction with outgoing lead, r is an amplitude of the reflection into the same arm, t is an amplitude of the transition to another arm (see the Fig.4.9). σ is the probability of

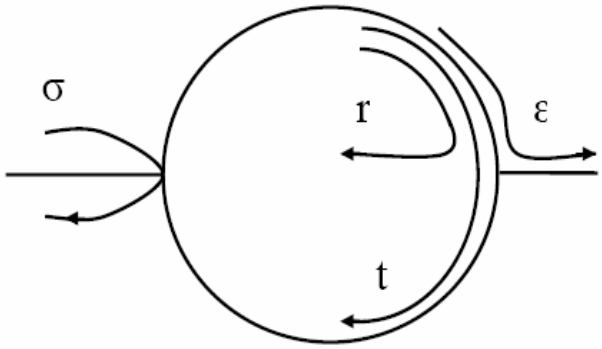

Figure 4.9 | t and r are transmission and reflection amplitudes inside the ring waveguide.σ is the reflection amplitude from the ingoing lead to itself,ϵ is transmission amplitude from the outgoing lead to the ring

the backscattering and $\sigma \ll 1$ for the structures with efficient injection. These parameters depend on properties of the structure itself.

The expressions 4.35 and 4.36 allow us to determine the intensity of an outgoing beam using relations:

$$\begin{aligned} r^2 + t^2 + \epsilon^2 &= 1 \\ \sigma^2 + 2\epsilon^2 &= 1 \end{aligned} \tag{4.41}$$

The more details on the method of quantum point contacts we used to calculate intensity in the outgoing lead can be found in ref.[132]. It depends on a Berry phase ϕ_B, which thus plays a role of the Aharonov-Bohm phase in electronic ring interferometers. The difference of the device we propose from the classical electronic AB interferometer is that it needs the presence of the magnetic field and not just of the vector potential in the region of the particle propagation, as we have already pointed out. It also should be noted that due to the peculiar orientation of the LT splitting for polaritons, there is no analogue of the Aharonov-Casher phaseshift for electrons in a ring with Rashba SOI. Indeed, for the electrons the AC phaseshift arises due to the distinct wavenumbers for the particles traveling clockwise and anticlockwise inside the ring, as for them the mutual orientation of the spin and effective magnetic field provided by Rashba SOI is different. On the contrary, for polaritons the inversion of the direction of propagetion does not change the direction of the effective magnetic field provided by TE-TM splitting (see the Fig.4.3), and thus AC phaseshift is absent.

The Berry phase can be modulated by tuning the intensity of TE-TM splitting, e.g.,

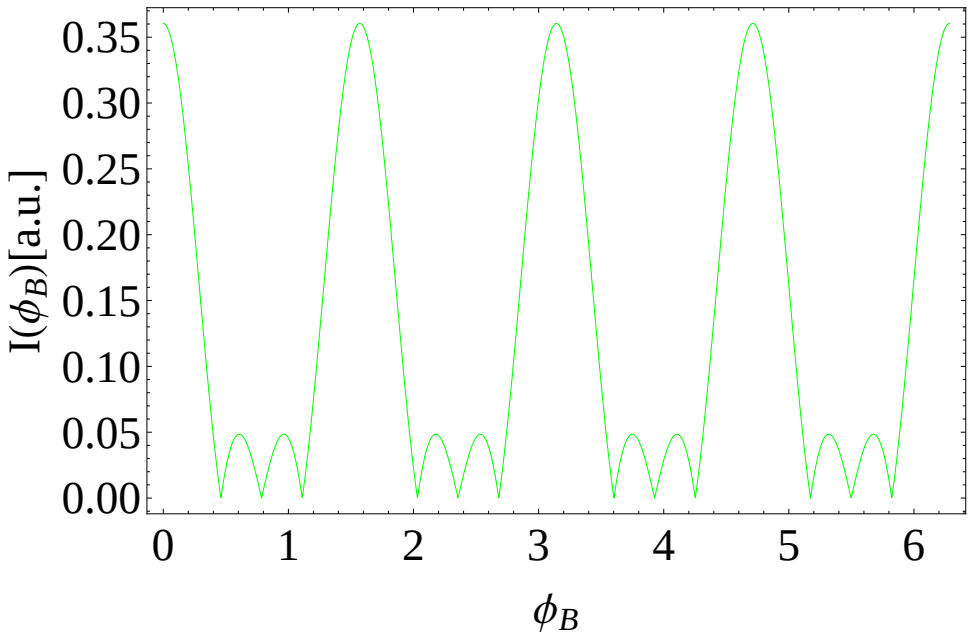

Figure 4.10 | The intensity of the outgoing polariton beam as a function of the Berry phase ϕ_B.

by variation of the detuning between the exciton and photon modes inside the ring (which can be achieved, e.g., by variation of stress forming the ring interferometer) or by tuning the external magnetic field. The dependence of the intensity of the beam on ϕ_B is shown on the Fig.4.10. The parameters are: $T/\tau = 0.2$, $r = 0.15$ and $t = 0.9$. One sees that the intensity is maximal for $\phi_B = 0, 2\pi$ and in the region between these two points reveal a local maximums at $\phi_B = \pi/2, \pi, 3\pi/2$.This interesting oscillation pattern comes from dependance on higher harmonics of ϕ_B.

To check the results of our analytical theory, we have performed a simulation of the structure we propose using coupled Gross-Pitaevskii equations for excitons and Schrödinger equations for photons taking into account their polarization.In this simulation we studied pulse propagation through the ring interferometer of 16 μm diameter without magnetic field as well as under a field of 35 T causing an exciton Zeeman splitting of 2 meV. This value can be sufficiently reduced by the use of diluted semi-magnetic cavities [133] or by choosing a different material system (e.g., CdSe/ZnSe [134]). Working at lower magnetic field is possible with materials having higher values of Landé g-factor as the Zeeman splitting scales with applied magnetic field B_Z like

$$\Delta_Z = g\mu_B B_Z, \tag{4.42}$$

where μ_B Borh magneton. This Landé factor in GaInAs structures, for example, is of an order of magnitude larger than in GaAs materials. Depending on In-dopping $g = 2.9 - 4.4$ is measured [135]. This can produce, for $g = 3.8$ Zeeman splitting $\Delta_Z = 1.1meV$ at $B_Z = 5T$. At the same time TE-TM splitting of the waveguide itself (theoretically

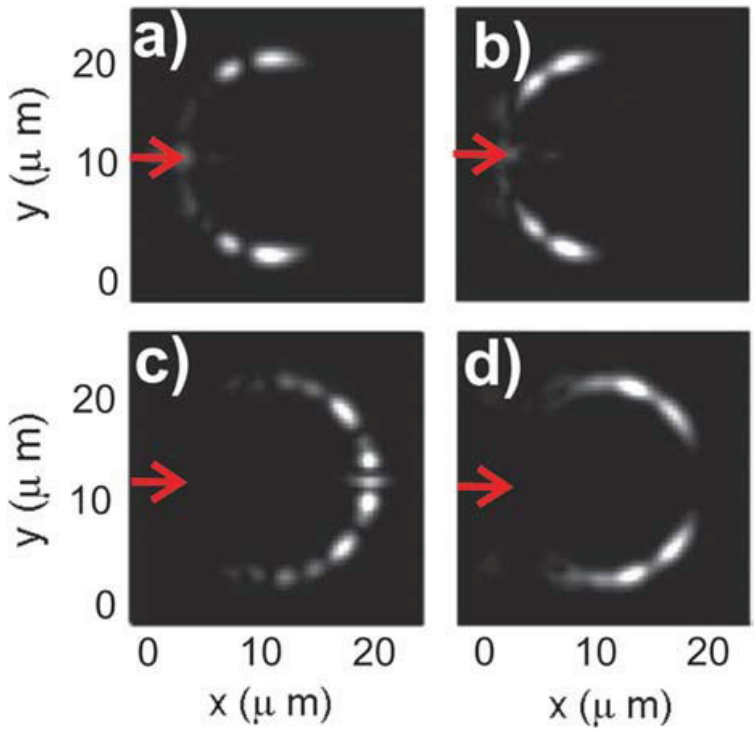

Figure 4.11 | Real-space images showing calculated emission intensity at Zeeman splitting 0 meV (a),(c) and 2 meV (b),(d) at different moments of time after the injection t=15 ps (a),(b) and t=30 ps (c),(d). Arrows show the direction of injection

predicted and measured in Ref. [129]) is about 0.25 meV for 2 μm cylindrical waveguide. To estimate the value of Δ_{LT} to this we should also add value of k-depenedent TE-TM splitting and both usually do not exceed several meVs. It is then technically possible to achieve regime of $\Delta_Z \sim \Delta_{LT}$ and experimentally observe Berry phase with exciton-polaritons. The results of our simulations are shown on the Fig. 4.11. All images show the spatial distribution of the emission intensity, which is directly proportional to the local density of polaritons. The figures 4.11(a) and 4.11(b) show the initial stage of the pulse propagation through the ring waveguide at time t= 15 ps after the excitation. The figures 4.11(c) and 4.11(d) show the final stage of the pulse propagation (t=30 ps), when the two beams interfere at the outgoing lead connection point. Without magnetic field [the figs. 4.11(a) and 4.11(c)] the interference is constructive, and the output into the outgoing lead has the highest value. Under a certain magnetic field [the figs. 4.11(b) and 4.11(d)] the interference is destructive and a dark spot is visible instead of a bright one. This result corresponds to the predictions of the analytical theory and demonstrates that such a waveguide can indeed operate as an optical interferometer.

4.4 Conclusions

We have proposed an optical analog of the spin-interference device based on a mesoscopic ring interferometer. We demonstrated that the Berry phase provided by the TE-TM and Zeeman splittings for polaritons plays a role of AB phase for electrons and leads to a variation of the intensity of the outgoing beam. On the other hand, there is no analogue of the corresponding Aharonov-Casher effect because of the peculiar symmetry of the TE-TM splitting. This system allows us to solve the main difficulties occurring in electronic systems such as the low efficiency of spin injection from a ferromagnet to a semiconductor system. The effect we propose cannot be observed for bare cavity photons, but is specific of strongly coupled exciton polaritons because it requires a finite Zeeman splitting. The use of exciton polaritons is also highly advantageous with respect to the bare excitons [136], since the mean free path of exciton polaritons is much longer due to their photon component

Chapter 5

Entanglement from a QD in a microcavity

Quantum entanglement is hardcore of a novel science - quantum information which tries to make a bridge between the fundamental ideas of quantum mechanics and new technologies. Entangled states are some kind of distant correlations in quantum systems rather coming from the superposition principle of quantum mechanics than from some kind of interactions, the latter being the reason of usual correlations. In this section we will see how these quantum states can be formed from a quantum dot strongly coupled to a microcavity. Biexcitons, or exciton molecules in QDs are known to possess two possible decay paths. To use them as an entangled state these two channels should be indistinguishable by any physical property. The principal problem is the splitting of the exciton levels in biexciton cascade which violates this property. We propose a new approach based on strong coupling to be used for recovering of the indistinguishability of biexciton decay paths.

Contents

5.1 Entanglement and quantum computing

Einstein, Podolsky, and Rosen (EPR)[137] in 1935. published a paper with the title "Can quantum mechanical description of reality be considered complete?" where they gave an argument about the incompleteness of quantum mechanics. To see what is the content of this argument we are going to consider a (thought) experiment.

A black box emits a pair of two particles of spin 1/2 in opposite directions in a singlet state - with total spin angular momentum zero, originating for example from decay of one particle with zero spin. To such a state one can associate a wave function

$$|\Psi_{12}\rangle = \frac{1}{\sqrt{2}}(|1/2\rangle_1 |-1/2\rangle_2 - |-1/2\rangle_1 |1/2\rangle_2) = \frac{1}{\sqrt{2}}(|1/2,-1/2> - |-1/2,1/2>). \quad (5.1)$$

This is an entangled state and we cannot factor it in the product of superpositions of $|1/2\rangle$ and $|-1/2\rangle$ states for particles 1 and 2

$$(|1/2\rangle_1 + |-1/2\rangle_1)/\sqrt{2} \otimes (|1/2\rangle_2 + |-1/2\rangle_2)/\sqrt{2} = \quad (5.2)$$
$$= \frac{1}{2}(|1/2,1/2> + |1/2,-1/2> + |-1/2,1/2> + |-1/2,-1/2>),$$

like it is the case when we speak about an uncorrelated state. The measurement on the particle 2 for two-particle state of the form 5.2 is not dependent of what we have measured on particle 1. After we measure the spin of first particle to be 1/2 or -1/2 the state 5.2 collapses in

$$|1/2\rangle_1 /\sqrt{2} \otimes (|1/2\rangle_2 + |-1/2\rangle_2)/\sqrt{2} \quad (5.3)$$

$$|-1/2\rangle_1 /\sqrt{2} \otimes (|1/2\rangle_2 + |-1/2\rangle_2)/\sqrt{2} \quad (5.4)$$

respectively. The outcome of the measurement on the second particle is 1/2 or -1/2 irrespectively of the spin of the first particle.

On the other hand for the entangled state 5.1 if we were to measure the spin $S_x^{(1)}$ of the first particle in the $x-$direction, for example, and obtain the value $\hbar/2$, we would know that the second particle is in an eigenstate of its spin operator $S_x^{(2)}$ with eigenvalue $-\hbar/2$. This way performing measurement on particle 1 we instantaneously know the state of particle 2 without performing any measurement on it. Furthermore, the spin of particle 2 is determined by what we have measured on particle 1 no matter how far are two particles and this is the reason why A. Einstein called this phenomena 'spooky' action-at-a-distance. In literature it is frequently refereed to as distant correlations. Since the direction of the spin is not defined before we have performed the measurement, we could choose to measure $S_y^{(2)}$ on the second particle and obtain the value $-\hbar/2$ for its spin. Automatically we would determine the value of the y-component of the spin of the first particle: $\hbar/2$. This means that observable $S_x^{(1)}$ and $S_y^{(1)}$ are compatible having the same

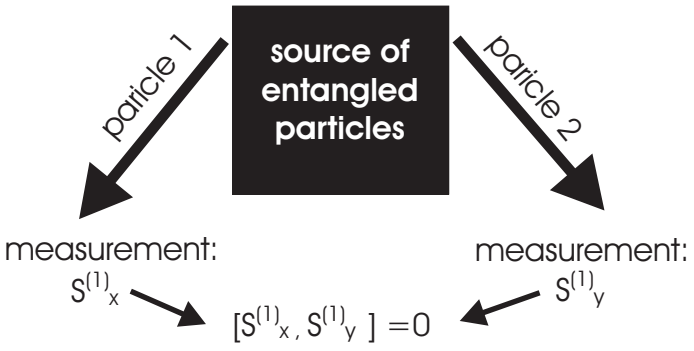

Figure 5.1 | Illustration of the EPR-paradox: two measurements made at the same time give a full set of spin components of the two entangled particles, which contradicts the basics of quantum mechanics, where the spin components do not commute.

eigenvectors and thus commuting. But $S_x^{(1)}$ and $S_y^{(1)}$ according to the Heisenberg principle of uncertainty they do not commute and they cannot both have definite values. This paradox arises, because we tend intuitively to think in classical terms, i.e. to associate an objective physical reality with each particle and its variable, whereas in quantum mechanics a dynamical variable does not have actually a value until it is measured - becoming an observable.

This situation is known as EPR paradox: the subject of one of the most interesting scientific (certainly philosophic as well) debates in previous century [138, 139, 140, 141, 142, 143, 144, 145, 146, 147, 148].

It was proposed later that the incompleteness of quantum mechanics arising in the EPR paradox can be resolved by one complete theory which should in order to account for all 'elements of reality' include the hidden variables or unmeasurable parameters [139]. Bell theoretically and after him the others (theory and experiment) [140, 141, 149, 142, 144, 145] showed that the EPR state violates an inequality - Bell's inequality which applied for large class of hidden variable theories. In particular, for local and counter-factual definiteness theories, the latter meaning the inclusion of all possible values of conjugate variables in consideration besides those which has been measured. Thus nonlocal effects are fundamentally quantum mechanical, and that no realistic local theory can account for the correlations quantitatively.

The entanglement forms the central part in new disciplines - quantum computing and quantum information. The idea itself comes from R. Feynman [150] who proposed it to simulate some quantum mechanical effects which cannot be simulated with classical computers. Quantum properties are used to represent data and quantum transformation are used as algorithms to work with these data. Instead of classical bits quantum computers use qubits. A single qubit is linear superposition

$$|\psi\rangle = c_1 |0\rangle + c_1 |1\rangle \tag{5.5}$$

where the basis vector $|\psi\rangle, |\psi\rangle$ in complex Hilbert space are represented with column-vectors $(0,1)^T, (1,0)^T$; T stands for matrix transposing and $|c_0|^2 + |c_1|^2 = 1$. Real appli-

cations needs manipulating of a register on n-qubits having 2^n-dimensional computational basis [151]. In the case of n=2, for example, the basis reads

$$\begin{aligned} |00\rangle &= |0\rangle \otimes |0\rangle = (0,0,0,1)^T, \\ |01\rangle &= |0\rangle \otimes |1\rangle = (0,1,0,0)^T, \\ |10\rangle &= |1\rangle \otimes |0\rangle = (0,0,1,0)^T, \\ |11\rangle &= |1\rangle \otimes |1\rangle = (1,0,0,0)^T. \end{aligned} \tag{5.6}$$

The 2-qubits register can be prepared in any superposition of above states similarly like in the expression for the 1-qubit state

$$|\psi\rangle = c_0 |00\rangle + c_1 |01\rangle + c_2 |10\rangle + c_3 |11\rangle . \tag{5.7}$$

The qubits 5.5 and 5.7 are vectors in Hilbert spaces C^2 and $C^2 \otimes C^2$, respectively.One can operate on this states by applying unitary operators - which are called quantum gates. Some common quantum gates used to realize quantum circuits (analogues of classical digital circuits) operating on single qubit state 5.5 are

$$\begin{array}{lll} I : |0\rangle \to |0\rangle & X : |0\rangle \to |1\rangle & Z : |0\rangle \to |0\rangle \\ \quad |1\rangle \to |1\rangle & \quad |1\rangle \to |0\rangle & \quad |1\rangle \to -|1\rangle \end{array} \tag{5.8}$$

where I is identity quantum gate, X is negation and Z is phase shift gate. If we want for example to perform a qunatum gate on a 2-qubits state such that we apply not-gate on the first qubit and phase shift gate on the second one we should act with operator $X \otimes Z$. Generalization to an n-qubit state is straightforward.

A very important transformation is the Hadamard gate given by matrix

$$H = \frac{1}{\sqrt{2}} \begin{bmatrix} 1 & 1 \\ 1 & -1 \end{bmatrix} . \tag{5.9}$$

Its action on the vector $|1,1\rangle$ of the basis 5.6

$$H \otimes H \, |1,1\rangle = H \, |1\rangle \otimes H \, |1\rangle = \frac{1}{2}(|0\rangle + |1\rangle) \otimes (|0\rangle + |1\rangle) \tag{5.10}$$

which is the superposition state 5.7 in the factor form. Possibility of making an such state from one classical state is the reason of importance of the Hadamard gate. Superposition 5.5 and 5.7 in 1-qubit and 2-qubits states plays a key role in quantum computation. Any action on a superposition of states renders the superposition of that operation on each state individually. This is not the case for classical computers and to see the importance of superposition principle for a quantum computing let's like in [151] consider an unitary

transformation U_f corresponding to a classical function f,$U_f : |x\rangle |y\rangle \rightarrow |x\rangle |y \oplus f(x)\rangle$, where $\oplus$ denotes exclusive-or. This transformation preserves the input and therefore is unitary. The $|y\rangle$ one can understood as hardware of a quantum computer. The action of U_f on state 5.7 is

$$\begin{aligned} U_f(|\psi\rangle |0\rangle) = U_f(\sum_{i=0}^{3} c_i |i\rangle |0\rangle) = \sum_{i=0}^{3} c_i U_f |i\rangle |0\rangle \\ = \sum_{i=0}^{3} c_i |i\rangle |0 \oplus f(i)\rangle = \sum_{i=0}^{3} c_i |i\rangle |f(i)\rangle \end{aligned} \tag{5.11}$$

where $|i\rangle$ is one of the basis vector in the superposition 5.7, and the last expression follows from $0 \oplus f = f$. f is simultaneously applied to all basis vector. Application of U_f computes all 2^2 values of function f: $f(0)...f(2^3 - 1)$ at once. This property is called quantum parallelism. The advantage of quantum computing is this possibility of computing 2^n values from n-qubits. The problem is that if one wants to read-out one computed value of f he has to make projection on measured state and all other information is lost. To extract such kind of information present in the superposition form one can use quantum teleportation [152, 153]. Quantum teleportation defined through various different communication protocols is essentially based on entanglement [154]. The first experimental realization of quantum teleportation has been done by Jennewein et al. in 2000 [155]. To guarantee the security of communications a new field quantum cryptography [156] is established based on idea that any 'eavesdropping' (measurement) will lead to the collapse of the wave function.

In the following section we are going to discuss solid state sources of entangled photon pairs based on single quantum dots as emitters.

5.2 Quantum dots as EPR-photon emitters

In the context of solid state physics, QDs as quantum emitters have drawn a strong attention when it has been proposed to realize entangled photon pair sources based on the biexciton decay[157]. The ideal decay paths are illustrated in the Fig.5.2. The biexciton decays emitting either first a σ_+ and second a σ_- polarized photon or vice versa, and the photons are fully polarization-entangled. In principle this idea is ingeniously simple, as it allows to implement such sources on a very small length scale and rises hope for the on-chip sources of entangled photon pairs, which could be easily implemented on nano chips for computing purposes.

Unfortunately, this proposal turned out to be hard to implement mainly because the intermediate exciton states of a typical QD are not degenerate due to the anisotropic

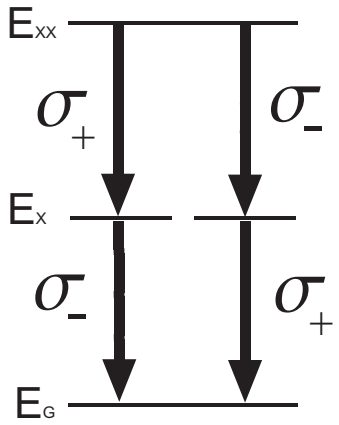

Figure 5.2 | Biexciton decay of an ideal quantum dot takes place from the biexciton state E_{XX} via two degenerate exciton states, which couple to different polarization of light. The final state is the ground state of the quantum dot.

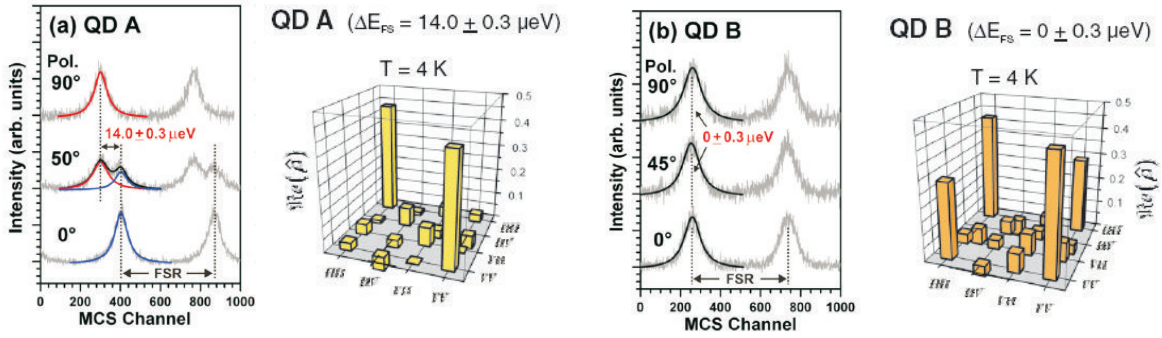

Figure 5.3 | Quantum correlations for selected quantum dots [161]: Selected quantum dots with (a) non-zero finestructure splitting and (b) zero splitting. The corresponding reconstructed density matrices for the selected quantum dots are also shown.

electron-hole interaction [158, 159]. Also the environment (i.e. the strain induced by the substrate) of the quantum dot can effect the transitions.

This interaction couples degenerate exciton states which split into two resonances coupled to two orthogonal linear polarizations called horizontal (H) and vertical (V), respectively. The resulting photons for the two decay channels are therefore distinguishable and the degree of entanglement becomes zero. The quantum correlations become hidden in time integrated measurements because a QD with split intermediate exciton levels emits photons into a time-evolving entangled state.[160]

Several proposals have been made to overcome this splitting of the exciton lines. The simplest one is of course to grow arrays of quantum dots and select only those, which show no fine structure splitting. This has been published in several reports [162, 161, 163]. The Fig. 5.3 shows the photoluminescence spectra of two quantum dots with either non-zero or

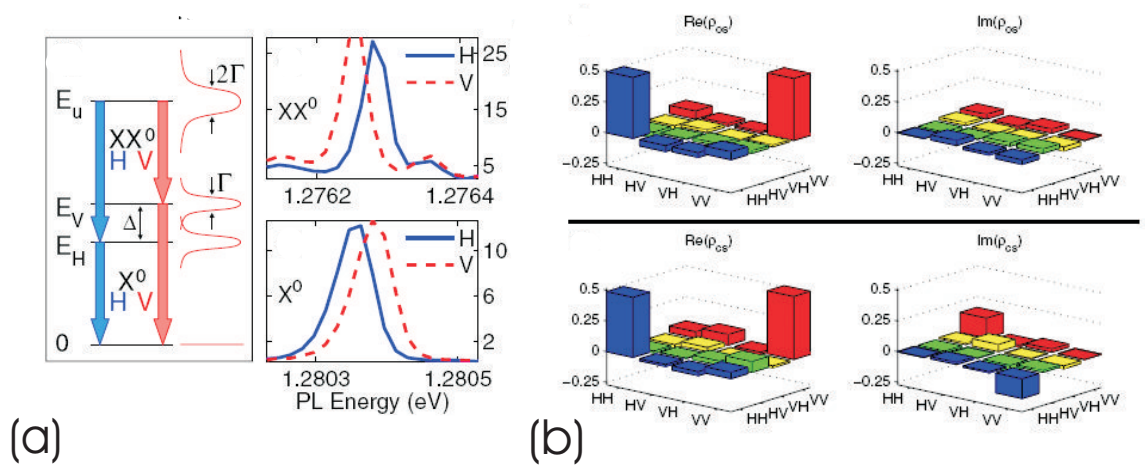

Figure 5.4 | Entanglement and spectral filtering [165]: (a) Shows the photoluminescence spectra, together with a schematic picture of the decay. (b) shows the reconstructed density matrix with a non-zero off-diagonal element for a large width of the spectral windows (upper panel) and for narrow spectral windows (lower panel).

zero splitting. The corresponding reconstructed density matrices show clearly an non-zero off-diagonal element for the zero splitting case, which corresponds directly to a non-zero degree of entanglement [164]. The disadvantage of this method is that the fabrication process of the quantum dot takes place almost without possibilities of controlling. Thus, it is always necessary to discover among a huge number of QDs those, which show no splitting. This makes future industrial implementation much more complicated because a huge effort is needed to fabricate one entangled photon source.

To avoid this, one needs other techniques to overcome the splitting. One, developed by Akopian et al. [165], is to introduce spectral filters in the experimental setup which select only the overlapping part of the transition. This procedure is illustrated in the Fig.5.4 together with the results for the reconstructed density matrix.

Depending on the splitting, the overlap of the transitions may be very small. This requires very narrow spectral windows to obtain entangled photon pairs. The disadvantage here is that the quantum efficiency (the number of detected photons), is very low, which restricts the possible applications of this technique in communication protocols. The third possibility we want to discuss here, is the use of external fields to shift the intermediate states to degeneracy. This has been shown for electrical fields [166, 167] and for magnetic fields [162, 163]. The latter work is illustrated on the Fig.5.5. The dependence of the fine structure splitting on the magnetic field is shown on the left hand side, showing the degeneracy of the exciton states for a given magnetic field. Three density matrices for different magnetic fields are shown on the right hand side, where the middle figure of the

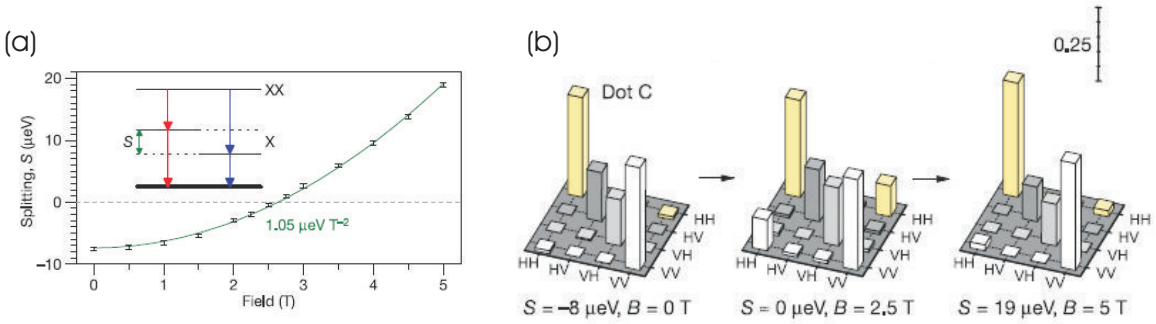

Figure 5.5 | Reduction of the finestructure splitting using external magnetic field [160]: (a) shows the fine structure splitting versus magnetic field. (b) shows the density matrices for different fields, where the matrix in the middle corresponds to a zero finestructure splitting.

lower panel corresponds to degeneracy. Both techniques together allows one to use almost arbitrary quantum dots and engineer them to work as EPR-sources.

Nevertheless, the degree of entanglement remains relatively low, due to the imperfections, dephasing [168] and other effects. This implies the need of new ideas and proposals to transform the simple idea of Benson et al. [157] to a real working device, which will be discussed in the next sections.

5.3 Strongly coupled dot-cavity system

The biexciton decay scheme for an ideal quantum dot is shown in the Fig.5.2. The intermediate exciton states are degenerate and they couple to circularly polarized light. In a real QD the Fig.5.6(a, left part) the exciton resonances coupled to H and V polarized light modes are typically split by an energy δ_X. We consider that such a QD is embedded within a photonic crystal, slightly anisotropic, which shows two confined optical modes polarized along H and V directions and split by a quantity δ_C (see the middle of the Fig.5.6(a)). Each of the two non-degenerate exciton states strongly couples to one resonance of the photonic crystal with either vertical (red) or horizontal (blue) polarization, respectively. This coupling gives rise to two polariton doublets polarized H and V. The resulting decay paths of the strongly coupled dot-cavity system can be seen on the Fig.5.6(a, right part).

There are now two possible decay channels for each polarization using either lower or upper polariton state. In Ref.[169] we have shown that for any constant values of δ_X and δ_C, the adjustment of the energy detuning between the group of exciton resonances and the group of photon resonances allows to make one polariton state with horizontal polarization degenerate with one polariton state with vertical polarization. This alignment makes the two possible decay paths of the biexciton using these two intermediate states

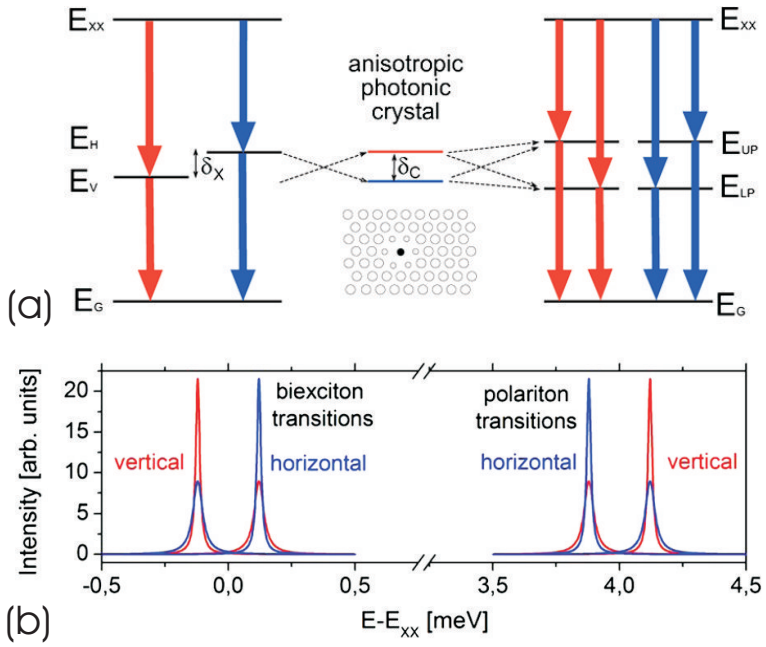

Figure 5.6 | Scheme 1: (a) biexciton decay of a real quantum dot (left), photonic crystal resonances (middle) and resulting decay scheme for the quantum dot embedded in the photonic crystal in the strong coupling regime (right). The blue arrows correspond to horizontal (H) polarization and the red arrows correspond to vertical (V) polarization. (b) shows the calculated photoluminescence spectra.

distinguishable only by their polarization which results in the generation of entangled photon pairs showing a maximum degree of entanglement.

The energy of the polariton states $E_{\pm}^{H,V}$ can be calculated using [170]

$$E_{\pm}^{H,V} = \frac{E_C^{H,V} + E_X^{H,V}}{2} \pm \frac{1}{2}\sqrt{(E_C^{H,V} - E_X^{H,V})^2 + 4\hbar^2\Omega_{H,V}^2}, \tag{5.12}$$

where H and V indicate the different polarizations, $E_C^{H,V}$ are the cavity resonances, $E_X^{H,V}$ are the exciton energies, and $\Omega_{H,V}$ are the values of Rabi splitting, proportional to the exciton oscillator strength which we assume to be equal for H and V polarized modes. In an isotropic QD, the oscillator strength of the polarized exciton modes can differ by a few percent and can provoke shifts of the polariton energy by a few μeV, which will be discussed later. It follows directly from Eq.(5.12) that the energies of the intermediate polariton states can be tuned by changing the energy of the photonic resonances.

The pairs of polariton states are degenerate($E_{\pm}^{H} = E_{\pm}^{V}$) if $E_H = E_C^V$ and $E_V = E_C^H$, which means that each resonance for V and H polarized light is adjusted to the energy of the exciton state coupled to the perpendicular polarization. In the same time, the biexciton transition is not strongly interacting with the cavity modes because the binding energy of the biexciton is at least one order of magnitude larger than $\hbar\Omega$. This resonance can of course interact with another photonic mode, but we do not want to address this case here and we therefore assume that the biexciton emission energy is not perturbed by the presence of the optical cavity. The right hand side of Fig.5.6(a) shows the resulting distribution of the energy levels. There are four possible decay channels for the biexciton.

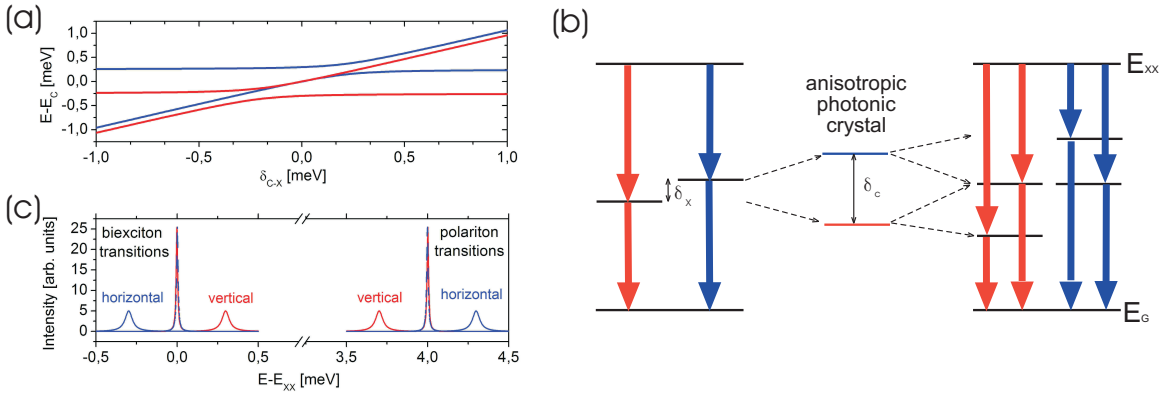

Figure 5.7 | Scheme 2: (a) Calculated energies of the polariton states for different detuning δ_{C-X} with , δ_x =0.1 meV, δ_C = - 0.5 meV, and $2\Omega_R$ =0.22 meV. Different polarizations are indicated with red (vertical) and blue (horizontal). (b) Distribution of the energy levels for δ_{C-X} =0. (c) Photoluminescence spectra for both polarizations.

The two decay paths using the UP as an intermediate state produce polarization entangled photon pairs, which is also the case for the decay paths using the LP. This configuration is particularly original and probably useful, since it allows producing two independent EPR pairs. The calculated photoluminescence spectra are shown in Fig.5.6 (b). The technological requirements for this scheme are however quite strong. The first condition is that the Rabi splitting should be larger than the splitting between the H and V exciton states $2\hbar\Omega_R > \delta_x$. The second condition is that the splitting between the optical modes is exactly equal to the splitting between the QD modes with an opposite sign $\delta_x = -\delta_c$. The first condition is usually well fulfilled. In InAS based structures δ_x is of the order of 0.05-0.1 meV, whereas $2\Omega_R \approx$ 0.15-0.25 meV. The second condition, because it is an equality, and because of the small value of δ_x , seems quite demanding, and would, in practice, require the growth and study of many structures.

We therefore propose another configuration, conceptually less ideal, but which should allow an easier experimental implementation. We propose to use an anisotropic photonic crystal showing a splitting δ_C substantially larger than δ_x. Neither the exact value, nor even the sign of δ_C play a crucial role in this scheme. This splitting should not be a problem, since it is difficult rather to fabricate photonic crystals without it. In ref. [171], for instance, the splitting measured is about 0.5 meV for a cavity with quality factor $Q > 10000$. Figure 5.7 (a) shows the eigenenergies versus the exciton-photon detuning $\delta_{C-X} = \frac{E_C^H - E_C^V}{2} - \frac{E_H - E_V}{2}$, keeping δ_x and δ_C constant. This kind of tuning of the exciton resonance energy can be performed experimentally, for example by changing the temperature of the sample [172, 173]. We consider here the case where δ_x and δ_C have

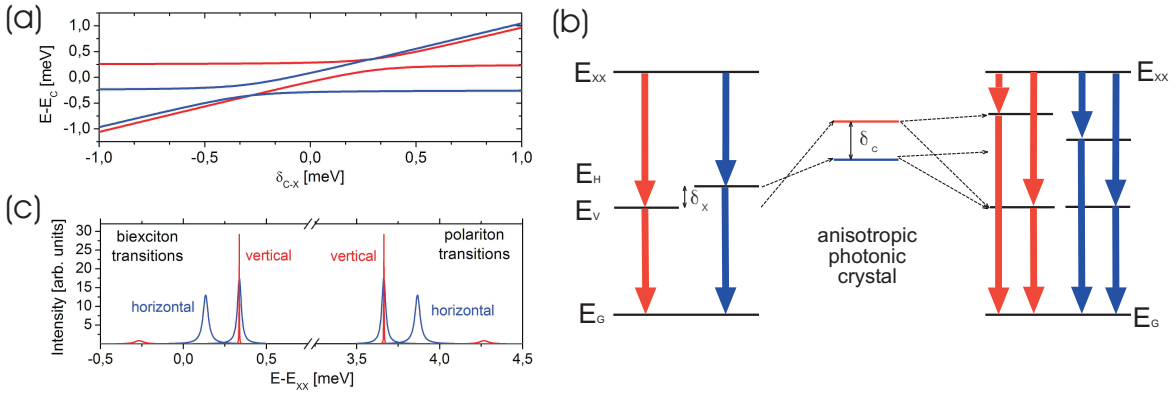

Figure 5.8 | Scheme 3: (a) Calculated energies of the polariton states for different detuning δ_{C-X} with , δ_x =-0.1 meV, δ_C = - 0.5 meV, and $2\Omega_R$ =0.22 meV. Different polarizations are indicated with red (vertical) and blue (horizontal). (b) Distribution of the energy levels for positive δ_C and negative δ_X. (c) Photoluminescence spectra for both polarizations at δ_{C-X}=-0.275 meV.

the same sign. For a wide range of detuning, the H-polarized LP and the V-polarized UP are almost degenerate. The decay channels of the biexciton are shown on the figure 5.7 (b). The luminescence spectra in two polarizations for positive detuning are shown on the figure 5.7 (c). The spectrum for each polarization consists of two groups of two peaks. The group with the lower energy corresponds to the biexciton decay to the polariton states. The group with the higher energy corresponds to the decay of the polariton states toward the ground state. For each polarization, the peak with the higher energy and the lower energy belong to the same decay cascade. The two central peaks belong to the same decay cascade as well. One can clearly see that the decay channel involving the H-polarized UP and the decay channel involving the V-polarized LP cannot be distinguished by energy measurements, but only by their polarization.

As said before, this degeneracy can also be found if δ_x and δ_C have opposite signs. Fig.5.8 (a) shows the eigenenergies versus δ_{C-X} in that case. The energy degeneracy now occurs at negative detuning between the LP states (H and V), and at positive detuning between the UP states (H and V). The decay channels of the biexciton for the negative detuning case are shown on the Fig.5.8 (b). The luminescence spectra for negative detunings are shown on the Fig.5.8 (c). Note the difference in the degeneracy of the peaks in Fig.5.7 (c) and Fig.5.8 (c): in first case LP is degenerate with UP of different polarization, and in the second case LP is degenerate with LP.

5.4 Degree of Entanglement

To describe the full decay scheme analytically we write the two-photon wavefunction in the following way neglecting cross polarization terms and using the notation UP for the upper and LP for the lower polariton state of the doublet:

$$\begin{aligned} |\Psi\rangle = &\left(\alpha_{LP}\left|p_H^{LP}\right\rangle + \alpha_{UP}\left|p_H^{UP}\right\rangle\right)|HH\rangle + \\ &+ \left(\beta_{LP}\left|p_V^{LP}\right\rangle + \beta_{UP}\left|p_V^{UP}\right\rangle\right)|VV\rangle\,, \end{aligned} \tag{5.13}$$

where we extract the coordinate part $\left|p_{H(V)}^{LP(UP)}\right\rangle$ from the polarization part of the wavefunction $|HH\rangle\,(|VV\rangle)$. The amplitudes α and β are the weights for the possible decay paths satisfying

$$|\alpha_{LP}|^2 + |\alpha_{UP}|^2 + |\beta_{LP}|^2 + |\beta_{UP}|^2 = 1. \tag{5.14}$$

After tracing out over all possible degrees of $|p\rangle$, the corresponding 2 photon density matrix in the basis of HH,HV,VH and VV for scheme 1 of the previous section reads

$$\rho = |\Psi\rangle\langle\Psi| = \begin{pmatrix} |\alpha_{LP}|^2 + |\alpha_{UP}|^2 & 0 & 0 & \gamma \\ 0 & 0 & 0 & 0 \\ 0 & 0 & 0 & 0 \\ \gamma^* & 0 & 0 & |\beta_{LP}|^2 + |\beta_{UP}|^2 \end{pmatrix}, \tag{5.15}$$

where

$$\gamma = \alpha_{LP}\beta_{LP}^*\left\langle p_H^{LP}|p_V^{LP}\right\rangle + \alpha_{UP}\beta_{UP}^*\left\langle p_H^{UP}|p_V^{UP}\right\rangle. \tag{5.16}$$

In case of scheme 2, the off-diagonal element transforms to

$$\gamma = \alpha_{LP}\beta_{UP}^*\left\langle p_H^{LP}|p_V^{UP}\right\rangle \tag{5.17}$$

We select only the degenerate intermediate states using spectral windows, represented by a projection P, around the biexciton emission energy E_{XX} and the polariton energy E_P. One can neglect those scalar products $\langle p_H|p_V\rangle$ which show no overlap assuming that the separation (in the case where two are degenerate) by at least the Rabi splitting Ω is much larger than the width of the wavefunction. This width is mostly governed by the lifetime of the polaritons. It can be more justified by the use of spectral windows where the parts outside of them are not collected and thus do not contribute to the off-diagonal element.

The use of spectral widows, which select only the degenerate LP-polariton states in scheme 1, can be performed by the application of a projection P. The wavefunction has to be retyped by $P\,||\Psi\rangle\,/|P\,||\Psi\rangle\,|^2$ which yield

$$\gamma = \frac{\alpha_{LP}\beta^*_{LP}\left\langle p_H^{LP}|P|p_V^{LP}\right\rangle + \alpha_{UP}\beta^*_{UP}\left\langle p_H^{UP}|P|p_V^{UP}\right\rangle .}{|P\,|\Psi\rangle\,|^2}. \tag{5.18}$$

. Once again, the scalar product $\alpha_{UP}\beta^*_{UP}\left\langle p_H^{UP}|P|p_V^{UP}\right\rangle$ can be neglected, because the spectral windows are centered to detect only the transitions via the lower polariton state.

The final equation for the off-diagonal element of scheme 2 reads

$$\gamma = \frac{\alpha_{LP}\beta^*_{UP}\left\langle p_H^{LP}|P|p_V^{UP}\right\rangle}{|P\,|\Psi\rangle\,|^2}. \tag{5.19}$$

Within the dipole and rotating wave approximations, the perturbation theory [165, 174] gives for the two photon function

$$A_H^{LP} \equiv \alpha_{LP}\left\langle k_1, k_2|p_H^{LP}\right\rangle = \frac{x_{ex}^{H,LP}\sqrt{\Gamma_{XX}}x_{ph}^{H,LP}\sqrt{\Gamma_H^{LP}}/2\pi}{(|k_1|+|k_2|-\epsilon_H^{XX})(|k_2|-\epsilon_H^{LP})}, \tag{5.20}$$

where k_1 and k_2 are the momenta of the photons and $\Gamma_{XX(LP)}$ is the line width of the biexciton (lower polariton). Furthermore, $\epsilon_{XX(LP)} = E_{XX(LP)} + i\Gamma_{XX(LP)}/2$ is the complex energy of the biexciton (lower polariton). The exciton (photon) Hopfield coefficients of the polariton state are denoted by $x_{ex(ph)}^{H,LP}$ and the polariton lifetime is given by the ratio of the square of the photon Hopfield coefficient and the cavity lifetime $\Gamma_{LP} = |x_{ph}^{H,LP}|^2/\tau_C$. A similar expression of the eq. (5.20) can be obtained for the upper polariton state and the perpendicular polarization. The final equation for the off-diagonal element of the density matrix reads for scheme 1 (scheme 2)

$$\gamma' = \frac{\int\int dk_1 dk_2 A_H^{LP*} W A_V^{LP(UP)}}{\int\int dk_1 dk_2 A_H^{LP*} W A_H^{LP} + \int\int dk_1 dk_2 A_V^{LP(UP)*} W A_V^{LP(UP)}}. \tag{5.21}$$

The function W corresponds to the spectral windows at the energies E_{XX} and E_{LP}^H.

Finally, to estimate the quantum correlations of the emitted photons we use the Peres criterion for entanglement [164], which states that the emitted photons are entangled for $\gamma = 1/2$ and not entangled for $\gamma = 0$ (see appendix).

The density matrix of the system is in the so-called "x-form", containing only diagonal and anti-diagonal elements and thus another measure of entanglement – the concurrence C [175] – is simply two times the absolute value of the off-diagonal element of the density matrix [176, 177].

The degree of entanglement is strongly correlated with the line shape of the transitions as it follows from the eq.(5.20)and eq.(5.21): the better the overlap of the detected emission lines, the higher the off-diagonal element. The photoluminescence spectra for each transition can be calculated by integration of the eq.(5.20) either over k_2 to obtain the biexciton-polariton emission line or over k_1 to obtain the polariton-ground state emission line [174].

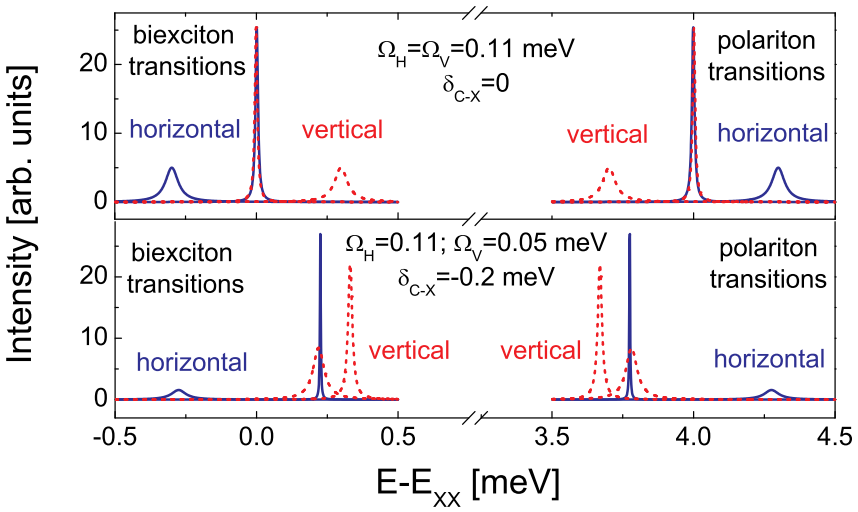

Figure 5.9 | Photoluminescence spectra for equal splittings (upper panel) at $\delta_{C-X} = 0$ and for splittings $\Omega_H = 0.11$ meV, $\Omega_V = 0.05$ meV at $\delta_{C-X} = -0.2$ meV (lower panel). The blue (red and dashed) line corresponds to horizontal (vertical) polarization.

The Fig.5.9 shows the complete spectra of emission resulting from the biexciton decay. The upper panel is calculated for $\Omega_H = \Omega_V$=0.11 meV which corresponds to the experimentally measured value of [178] and the lower one for Ω_H=0.11 meV and Ω_V=0.05 meV. The relative position of the cavity resonance $\delta_{C-X} = (E_C^H + E_C^V)/2 - (E_X^H + E_X^V)/2$ is chosen to degenerate the intermediate polariton states for both cases. The complicated complete spectra shows 4 Lorentzian lines for the biexciton-polariton transitions with a line width $(\Gamma_{XX} + \Gamma_P)$ and 4 Lorentzian lines with Γ_P for the polariton-ground state transitions. The line width depends strongly on the photonic fraction of the polariton because the cavity photon lifetime is typically 100 times shorter that the QD exciton lifetime. One should note that this type of spectra resulting from the biexciton decay in a strongly coupled microcavity has been recently measured but only for one polarization [179]. One can see on the upper panel, that the resonance condition between the two polariton states H and V also corresponds to equal line width of the states and therefore to a high degree of entanglement $\gamma' = 0.49$. On the other hand one can see on the lower panel of the figure that the nice symmetry of the scheme is broken when the oscillator strengths of the two resonances are different. The degree of entanglement is much lower $\gamma' = 0.09$ in this last case, which we are going to analyze in details in the next section.

In [180] the authors have refined our initial proposal improving the calculation of the emission spectra of the transitions by the use of the Weisskopf-Wigner approach. In the large coupling constant (g) case, the improvement with respect to the simple picture

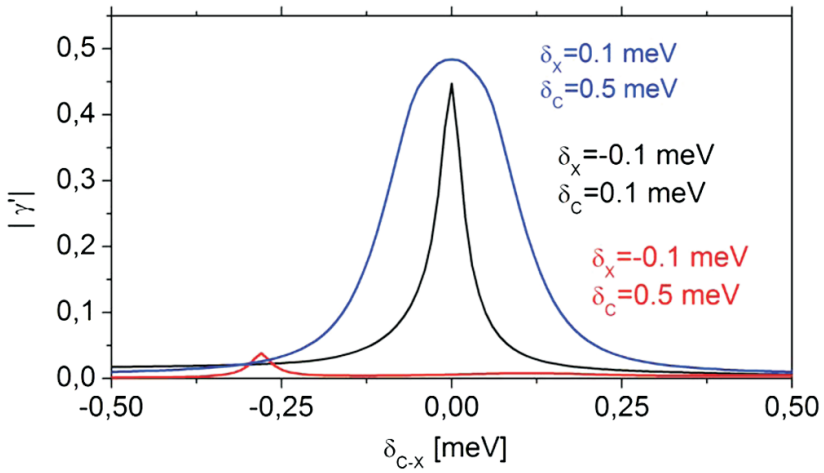

Figure 5.10 | Degree of entanglement: Dependence of the off-diagonal element γ' on the relative position of the cavity resonances δ_{C-X} for the schemes presented on the Fig. 5.6 5.7 and the Fig. 5.8.

using Lorenzian lines is not significant. Some changes arise in the small g case, where even without filtering a higher degree of entanglement is predicted with respect to our approach.

Furthermore, more complex approaches for the spectra of strongly coupled quantum dots have been published [181].

To finish this section we compare the degrees of entanglement, which can be obtained for the different schemes. We keep the Rabi-splitting constant for both polarizations. The Figure 5.10 shows the numerically obtained off-diagonal element $|\gamma|$ versus $\delta C - X$. The maximum value of $|\gamma|$ for scheme 3 is not optimal, due to the difference between the exciton and photon fractions of the degenerate polariton states. The asymmetry of the curves comes from the small lifetimes for negative detuning δ_{C-X}. Consequently, the line width is larger than the energy difference between the two polariton states, which yields $\langle P_H^{LP}|P|P_V^{LP}\rangle > 0$. On the other hand, the degree of entanglement achieved within the schemes proposed in Figs. 5.6 and 5.7 reaches almost the maximum value 1/2, which makes these configurations quite favorable.

5.5 Experimental implementation

As mentioned already in the first chapter, one dimensional polaritons have been observed recently for various cavity designs [172, 173, 182, 183]. In our proposal we focused on photonic crystal cavities. In general, the quantum dot is placed as an defect state into the lattice of holes. The structure of suited cavities with quality factors above 10^4 [184] is shown in Fig.5.11 on the left hand side. The placement of the dot is now well under control. What we need are split photonic modes for the linear polarizations. In fact, normally one tries to avoid this splitting and the photonic crystal community has made a huge effort to create degenerated photonic modes [171]. The right hand side of the Fig.

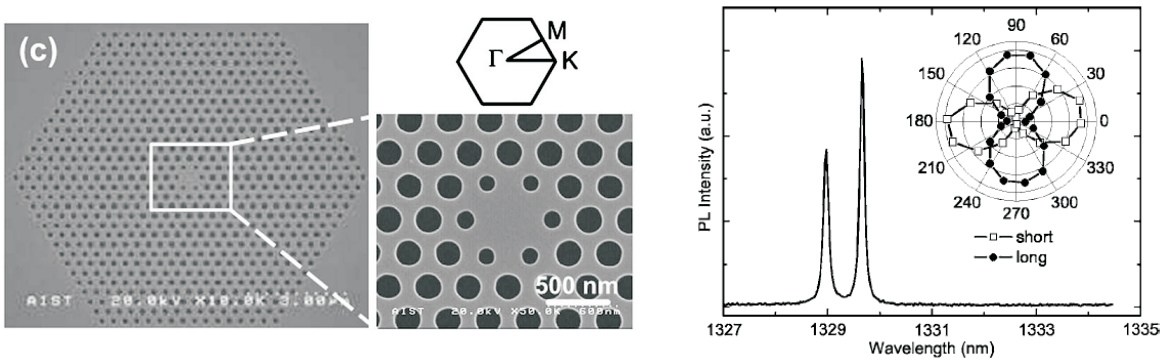

Figure 5.11 | High quality photonic crystal structures with mode splitting [171]: (left) Specifications of fabricated QD-embedded PC nanocavity. SEM image of the PC structure with the corresponding reciprocal lattice space. (right) Typical spectrum of the dipole modes with $Q > 10000$. The small local fabrication error breaks the degeneracy of modes A and B to make a 0.7 nm split. Inset: polar plot of the polarization dependence of short (open squares with line) and long (filled circles with line) wavelength modes.

5.11 shows the photoluminescence of such a structure with non-degenerate cavity dipole modes. We use now this splitting, which comes from any small fabrication imperfection of the holes in the photonic crystal [171].

Once the quantum dot is embedded into the crystal, the resonances have to be adapted carefully if has not been done before, during the fabrication of the crystal. This can be done by AFM nano-oxidation of the cavity surface [178]. The Fig. 5.12 shows the application of this technique to shift the photon modes to the desired position. The technique provides nearly continuous tuning of a single mode over several nanometers and is in principle applicable to all photonic crystal based cavity structures. This powerful tool makes our proposal more realistic because the cavity resonances can be modified after the fabrication of the quantum dot. This means the properties of the crystal can be adjusted perfectly to the properties of the embedded dot. Once the cavity modes are precisely tuned to the exciton levels in a QD, efficient nonclassical photon sources can be achieved for quantum information processing.

Finally, a strongly coupled biexciton requires additional resonances in the crystal. This can in principle provided by higher resonances. In the previous picture, we discussed dipole modes of the crystal, with a maximum of the electric field in the center of the quantum dot. The Fig. 5.13 shows the electric field distribution of different resonances of the quantum dot together with the energy distribution depending on the crystal parameters.

For example the second dipole modes (i and j in the figure) could be the candidates for strongly coupled biexciton devices.

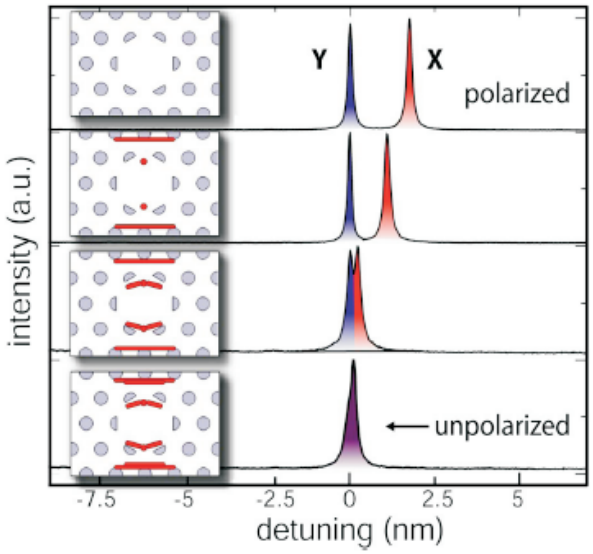

Figure 5.12 | Tuning of photonic crystal resonances [178]: PL spectra showing the detuning of the dipole-mode pair in one cavity resonant at 950 nm. The detuning of a DX mode is reduced from 2 to 0.1 nm as the cavity is sequentially AFM oxidized according to the insets on the left, where the oxide is depicted in red.

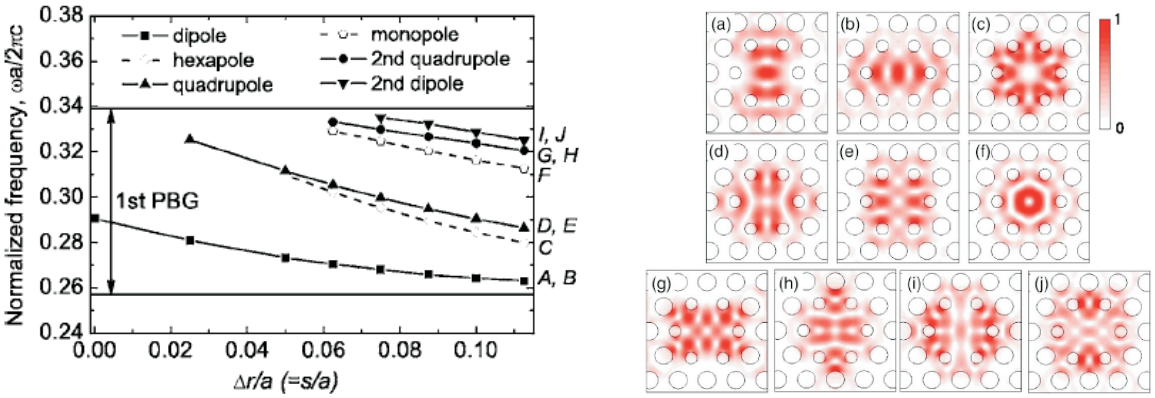

Figure 5.13 | Cavity mode frequencies and electric field inside a photonic crystal [171]: (left) Normalized cavity-mode frequencies as a function of $\Delta r/a$. The solid (dashed) lines correspond to doubly degenerate (nondegenerate) cavity modes. The ten modes are referred to as modes A-J in order of frequency. (right) Calculated electric field distributions in the slab center for ten cavity modes with $\delta r/a = 0.11$. The modes in (a)(j) correspond to modes A-J on the left hand side, respectively.

Of course the coupling between the dot and the cavity depends strongly on the position of the dot in the cavity, and the dot should may be not centered in the defect state because the electric field maxima are not centered.

All these techniques together confirm the possibility to realize the proposal of a entangled photon source, as discussed in this chapter.

Possible other cavity configurations are micropillars. Recently, new fabrication techniques have been developed to place a quantum dot exactly in the center of a micropillar [185]. Extending this techniques, one may fabricate slightly elliptic micropillars to obtain a split of the linear polarized cavity modes. Secondly, the spatial profile of the emission is the same for both polarizations. (By the way, this is not the case for photonic crystals, which make the realization based on crystals a bit more challenging.) Thus, also micropillars with embedded quantum dot can be a promising candidate for the present proposal, beside the exciting results on single photon sources [186, 187]. Nevertheless, this structures are in the process of development and several problems are not solved, i.e. the extraction of the biexciton-exciton photon is still not possible, because it is in the photonic gap. May-be lateral detection can solve this problem.

5.6 Summary and conclusions

We conclude that the control of the electronic resonances through their strong coupling to confined cavity modes opens new perspectives and is from many points of view extremely advantageous for the fabrication of a solid source of entangled photon pairs emitted on demand.

Bibliography

[1] Hopfield, J. Theory of the contribution of excitons to the complex dielectric constants of crystals. *Phys. Rev.* **112**, 1555 (1958).

[2] Agranovich, V. Dispersion of electromagnetic waves in crystals. *JETP Lett.* **37**, 430 (1959).

[3] Pekar, S. *Zh. Eksp. Teor. Fiz.* **33**, 1022 (1957).

[4] Ulbrich, R. G. & Weisbuch, C. Resonant Brillouin scattering of excitonic polaritons in Gallium Arsenide. *Phys. Rev. Lett.* **38**, 865–868 (1977).

[5] Anderson, M. H., Ensher, J., Matthews, M., Wieman, C. & Cornell, E. Observation of Bose-Einstein condensation in a dilute atomic vapor. *Science* **269**, 198–201 (1995).

[6] Imamoglu, A. & Ram, J. R. Quantum dynamics of exciton lasers. *Phys. Lett. A* **214**, 193 (1996).

[7] Malpuech, G. *et al.* Room-temperature polariton lasers based on GaN microcavities. *Appl. Phys. Lett.* **81**, 412 (2002).

[8] Savvidis, P. G. *et al.* Angle-resonant stimulated polariton amplifier. *Phys. Rev. Lett.* **84**, 1547 (2000).

[9] Gippius, N. A. *et al.* Polarization multistability of cavity polaritons. *Phys. Rev. Lett.* **98**, 236401 (2007).

[10] I.A. Shelykh, A. K. & Malpuech, G. Spin dynamics of exciton polaritons in microcavities. *Phys. Stat. Sol. (b)* **242** (2005).

[11] Frenkel, J. On the transformation of light into heat in solids. I. *Phys. Rev.* **37**, 17–44 (1931).

[12] Yamamoto, Y. & Imamoglu, A. *Mesoscopic Quantum Optics* (Wiley-Interscience, 1999).

[13] Ivchenko, E. L. *Optical Spectroscopy of Semiconductor Nanostructures* (Alpha Science International Ltd, 2005).

[14] Haug, H. & Koch, S. W. *Ouantum Theory of the Optical and Electronic Properties of Semiconductors* (World Scientific Publishing Co. Pte. Ltd., 1990).

[15] Andrews, M. Singular potentials in one dimension. *Am. J. Phys.* **44**, 1064.

[16] Mandel, L. & Wolf, E. Optical coherence and quantum optics. *Cambrige University Press* 465–522 (1995).

[17] Whittaker, D. M. *et al.* Motional narrowing in semiconductor microcavities. *Phys. Rev. Lett.* **77**, 4792–4795 (1996).

[18] Laikhtman, B. Are excitons really bosons? *J. Phys.: Condens. Maatter* **19**, 295214 (2007).

[19] Combescot, M. & Betbeder-Matibet, O. Faraday rotation in photoexcited semiconductors: A composite-exciton many-body effect. *Phys. Rev. B* **74**, 125316 (2006).

[20] T. K. Paraiso, Y. L. F. M.-G. . B. D.-P., M. Wouters. Multistability of a coherent spin ensemble in a semiconductor microcavity. *Nat. Mater.* 655660 (2010).

[21] Vladimirova, M. *et al.* Polariton-polariton interaction constants in microcavities. *Phys. Rev. B* **82**, 075301 (2010).

[22] A.I. Bobryesheva, M. M. & Shmiglyk, M. On the bi-exciton formation in crystals. *Phys. Stat. Sol. B* **53**, 71 (1972).

[23] C. Ciuti, C. P., V. Savona & Quattropani, A. Role of the exchange of carriers in elastic exciton-exciton scattering in quantum wells. *Phys. Rev. B* **58**, 7926 (1998).

[24] Bruus, H. & Flensberg, K. *Many-body Quantum Theory in Condensed Matter Physics - An Introduction* (Oxford University Press, 2007).

[25] K., H. *Introduction to Statistical Physics* (Taylor and Francis, 2001).

[26] Einstein, A. Quantentheorie des einatomigen idealen Gases. *Sitzungsberichte der preussischen Akademie der Wissenschaften* **Bd. XXII**, 261–267 (1924).

[27] Leggett, A. J. Quantum liquids - Bose condensation and Cooper pairing in condensed-matter systems. *Cambrige University Press* 40–47 (2006).

[28] Pitaevskii, L. & Stringari, S. Bose-Einstein condensation. *Clardon Press - Oxford* 341–346 (2003).

[29] Kasprzak, J. *et al.* Bose-Einstein condensation of exciton polaritons. *Nature* **443**, 409 (2006).

[30] Malpuech, G., Rubo, Y. G., Laussy, F. P., Bigenwald, P. & Kavokin, A. V. Polariton laser: thermodynamics and quantum kinetic theory. *Semicond. Sci. Technol.* **18**, S395–S404 (2003).

[31] Meier, F. & Zakharchenya, B. P. Optical orientation. *New York: North-Holland* (1984).

[32] Wolfram, S. Mathematica. *Addison-Wesley, New York* (1993).

[33] Pavlovic, G., Malpuech, G. & Gippius, N. A. Dispersion and polarization conversion of whispering gallery modes in nanowires. *Phys. Rev. B* **82**, 195328 (2010).

[34] Motayed, A., Davydov, A. V., He, M., Mohammad, S. N. & Melngailis, J. 365 nm operation of n-nanowire/p-gallium nitride homojunction light emitting diodes. *Appl. Phys. Lett.* **90**, 183120 (2007).

[35] Schenkel, T. *et al.* Solid state quantum computer development in silicon with single ion implantation. *J. Appl. Phys.* **94**, 7017 (2003).

[36] Hahm, J. & Lieber, C. M. Direct ultrasensitive electrical detection of DNA and DNA sequence variations using nanowire nanosensors. *Nano Lett.* **4 (1)**, 5154 (2004).

[37] Huang, M. H. *et al.* Room-temperature ultraviolet nanowire nanolasers. *Science* **292**, 1897 – 1899 (2001).

[38] Kavokin, A. & Malpuech, G. *Cavity polaritons* (Elsevier, 2003).

[39] Trichet, A. *et al.* One-dimensional ZnO exciton polaritons with negligible thermal broadening at room temperature. *arXiv:0908.3838v2* (2009).

[40] Wiersig, J. Hexagonal dielectric resonators and microcrystal lasers. *Phys. Rev. A* **67**, 023807 (2003).

[41] Nobis, T. & Grundmann, M. Low-order optical whispering-gallery modes in hexagonal nanocavities. *Phys. Rev. A* **72**, 063806 (2005).

[42] Kavokin, A. & Malpuech, G. *Cllasical electrodynamics* (Elsevier, 2003).

[43] Jones, H. F. *Groups, Representations and Physics* (Taylor and Francis, 1998).

[44] van den Berg, P. & Fokkema, J. The rayleigh hypothesis in the theory of diffraction by a cylindrical obstacle. *IEEE Transactions on Antennas and Propagations* **AP-27**, 577 (1979).

[45] Tikhodeev, S. G. & Gippius, N. A. Plasmonpolariton effects in nanostructured metaldielectric photonic crystals and metamaterials. *Phys.-Usp.* **52**, 945 (2009).

[46] Gippius, N. A., Weiss, T., Tikhodeev, G., S. & H., G. Resonant mode coupling of optical resonances in stacked nanostructures. *Optics Express* **18(7)**, 7569 (2010).

[47] Sun, L. *et al.* Direct observation of whispering gallery mode polaritons and their dispersion in a ZnO tapered microcavity. *Phys. Rev. Lett.* **100**, 156403 (2008).

[48] Zamfirescu, M., Kavokin, A., Gil, B., Malpuech, G. & Kaliteevski, M. ZnO as a material mostly adapted for the realization of room-temperature polariton lasers. *Phys. Rev. B* **65**, 161205 (2002).

[49] Hopfield, J. J. & Thomas, D. G. On some observable properties of longitudinal excitons. *Journal of Physics and Chemistry of Solids* **12**, 276 (1960).

[50] Schmidt-Grund, R. *et al.* ZnO based planar and micropillar resonators. *Superlattices and Microstructures* **41**, 360 (1960).

[51] Shimada, R., Xie, J., Avrutin, V., Özgür, . & Morkoc, H. Cavity polaritons in ZnO-based hybrid microcavities. *Appl. Phys. Lett.* **92**, 011127 (2008).

[52] Nakayama, M., Komura, S., Kawase, T. & Kim, D. Observation of exciton polaritons in a ZnO microcavity with HfO2/SiO2 distributed Bragg reflectors. *J. Phys. Soc. Jpn.* **77**, 093705 (2008).

[53] Chen, J.-R. *et al.* Large vacuum Rabi splitting in ZnO-based hybrid microcavities observed at room temperature. *Appl. Phys. Lett.* **94**, 061103 (2009).

[54] van Vugt, L. K. *et al.* Exciton polaritons confined in a ZnO nanowire cavity. *Phys. Rev. Lett.* **97**, 147401 (2006).

[55] Yu, K. *et al.* Efficient field emission from tetrapod-like zinc oxide nanoneedles. *Materials Letters* **59**, 1866 (2005).

[56] McCall, S. L., Levi, A. F. J., Slusher, R. E., Pearton, S. J. & Logan, R. A. Whispering-gallery mode microdisk lasers. *Appl. Phys. Lett.* **60**, 289 (1992).

[57] Dasbach, G., Schwab, M., Bayer, M., Krizhanovskii, D. N. & Forchel, A. Tailoring the polariton dispersion by optical confinement: Access to a manifold elastic polariton pair scattering channels. *Phys. Rev. B* **66**, 201201–4(R) (2002).

[58] Rühle, S. *et al.* Nature of sub-band gap luminescent eigenmodes in a ZnO nanowire. *Nano Lett.* **8**, 119–123 (2008).

[59] Chichibu, S. F., Sota, T., Cantwell, G., Eason, D. B. & Litton, C. W. Polarized photoreflectance spectra of excitonic polaritons in a ZnO single crystal. *J. Appl. Phys.* **93**, 756 (2003).

[60] Hümmer, K. & Gebhardt, P. Angular dependence of the reflection spectra and directional dispersion of the anisotropic exciton polaritons in ZnO. *Physica Status Solidi (b)* **85**, 271 (1978).

[61] Kaliteevski, M., Brand, S., Abram, R. A., Kavokin, A. & Dang, L. S. Whispering gallery polaritons in cylindrical cavities. *Phys. Rev. B* **75**, 233309–4 (2007).

[62] Soci, C. *et al.* Zno nanowire uv photodetectors with high internal gain. *Nano Letters* **7**, 1003–1009 (2007). URL `http://pubs.acs.org/doi/abs/10.1021/nl070111x`. `http://pubs.acs.org/doi/pdf/10.1021/nl070111x`.

[63] Klingshirn, C. *et al.* Excitonic properties of ZnO. *Advances in Solid State Physics* **45**, 261 (2005).

[64] Savona, V. & Piermarocchi, C. Microcavity polaritons: Homogeneous and inhomogeneous broadening in the strong coupling regime. *Phy. Stat. Sol. (a)* **164**, 45 (1997).

[65] Rudin, S., Reinecke, T. L. & Segall, B. Temperature-dependent exciton linewidths in semiconductors. *Phys. Rev. B* **42**, 11218–11231 (1990).

[66] Richard, S. *et al.* Momentum spectroscopy of 1D phase fluctuations in Bose-Einstein condensates. *Phys. Rev. Lett.* **91**, 010405 (2003).

[67] Kinoshita, T., Wenger, T. & Weiss, D. S. A quantum Newton's cradle. *Nature* **440**, 900–903 (2006).

[68] Paredes, B. *et al.* Tonks-Girardeau gas of ultracold atoms in an optical lattice. *Nature* **429**, 277–281 (2004).

[69] Saba, M. *et al.* High-temperature ultrafast polariton parametric amplification in semiconductor microcavities. *Nature* **414**, 731–735 (2001).

[70] Ciuti, C. Branch-entangled polariton pairs in planar microcavities and photonic wires. *Phys. Rev. B* **69**, 245304–8 (2004).

[71] Josephson, B. D. Possible new effects in superconductive tunnelling. *Phys. Lett.* **1**, 251 (1962).

[72] Shelykh, I. A., Solnyshkov, D. D., Pavlovic, G. & Malpuech, G. Josephson effects in condensates of excitons and exciton polaritons. *Phys. Rev. B* **78**, 041302 (2008).

[73] Likharev, K. K. Superconducting weak links. *Rev. Mod. Phys.* **51**, 101–159 (1979).

[74] Barone, A. & Paterno, G. *Physics and Applications of the Josephson Effect* (1982).

[75] Raghavan, S., Smerzi, A., Fantoni, S. & Shenoy, S. R. Coherent oscillations between two weakly coupled Bose-Einstein condensates: Josephson effects, p oscillations, and macroscopic quantum self-trapping. *Phys. Rev. A* **59**, 620 (1999).

[76] Albiez, M. *et al.* Direct observation of tunneling and nonlinear self-trapping in a single bosonic Josephson junction. *Phys. Rev. Lett.* **95**, 010402 (2005).

[77] Pereverzev, S. V., Loshak, A., Backhaus, S., Davis, J. C. & Packard, R. E. Quantum oscillations between two weakly coupled reservoirs of superfluid 3-He. *Nature* **388**, 449 (1997).

[78] Kenkre, V. M. & Campbell, D. K. Self-trapping on a dimer: Time-dependent solutions of a discrete nonlinear Schrödinger equation. *Phys. Rev. B* **34**, 4959–4961 (1986).

[79] Hammack, A. T. *et al.* Trapping of cold excitons in quantum well structures with laser light. *Phys. Rev. Lett.* **96**, 227402 (2006).

[80] Balili, R. B., Snoke, D. W., Pfeiffer, L. & West, K. Actively tuned and spatially trapped polaritons. *Appl. Phys. Lett.* **88**, 031110 (2006).

[81] Daïf, O. E. *et al.* Polariton quantum boxes in semiconductor microcavities. *Appl. Phys. Lett.* **88**, 061105 (2006).

[82] Combescot, M., Betbeder-Matibet, O. & Combescot, R. Bose-Einstein condensation in semiconductors: The key role of dark excitons. *Phys. Rev. Lett.* **99**, 176403 (2007).

[83] Ciuti, C., Savona, V., Piermarocchi, C., Quattropani, A. & Schwendimann, P. Role of the exchange of carriers in elastic exciton-exciton scattering in quantum wells. *Phys. Rev. B* **58**, 7926–7933 (1998).

[84] Renucci, P. *et al.* Microcavity polariton spin quantum beats without a magnetic field: A manifestation of Coulomb exchange in dense and polarized polariton systems. *Phys. Rev. B* **72**, 075317 (2005).

[85] Shelykh, I. A., Rubo, Y. G., Malpuech, G., Solnyshkov, D. D. & Kavokin, A. Polarization and propagation of polariton condensates. *Phys. Rev. Lett.* **97**, 066402 (2006).

[86] Jack, M. W., Collett, M. J. & Walls, D. F. Coherent quantum tunneling between two Bose-Einstein condensates. *Phys. Rev. A* **54**, R4625–R4628 (1996).

[87] Zapata, I., Sols, F. & Leggett, A. J. Josephson effect between trapped Bose-Einstein condensates. *Phys. Rev. A* **57**, R28–R31 (1998).

[88] Smerzi, A., Fantoni, S., Giovanazzi, S. & Shenoy, S. R. Quantum coherent atomic tunneling between two trapped Bose-Einstein condensates. *Phys. Rev. Lett.* **79**, 4950–4953 (1997).

[89] Milburn, G. J., Corney, J., Wright, E. M. & Walls, D. F. Quantum dynamics of an atomic Bose-Einstein condensate in a double-well potential. *Phys. Rev. A* **55**, 4318–4324 (1997).

[90] Wouters, M. & Carusotto, I. Excitations in a nonequilibrium Bose-Einstein condensate of exciton polaritons. *Phys. Rev. Lett.* **99**, 140402 (2007).

[91] Wouters, M. Synchronized and desynchronized phases of coupled nonequilibrium exciton-polariton condensates. *Phys. Rev. B* **77**, 121302 (2008).

[92] Sarchi, D., Carusotto, I., Wouters, M. & Savona, V. Coherent dynamics and parametric instabilities of microcavity polaritons in double-well systems. *Phys. Rev. B* **77**, 125324 (2008).

[93] Aleiner, I. L. & Ivchenko, E. L. Anisotropic exchange splitting in type-II GaAs/AlAs superlattices. *JETP Lett.* **55**, 692 (1992).

[94] Klopotowski, L. *et al.* Optical anisotropy and pinning of the linear polarization of light in semiconductor microcavities. *Solid State Commun.* **139**, 511 (2006).

[95] Brunetti, A. *et al.* Linear dichroism in a GaAs microcavity. *Superlattices Microstruct.* **41**, 429 (2007).

[96] Shelykh, I. A., Kavokin, A. V. & Malpuech, G. Spin dynamics of exciton polaritons in microcavities. *Phys. Status Solidi (b)* **242**, 2271 (2005).

[97] Solnyshkov, D. *et al.* Nonlinear effects in spin relaxation of cavity polaritons. *Semiconductors* **41**, 1080 (2007).

[98] Malpuech, G., Solnyshkov, D. D., Ouerdane, H., Glazov, M. M. & Shelykh, I. Bose glass and superfluid phases of cavity polaritons. *Phys. Rev. Lett.* **98**, 206402 (2007).

[99] Solnyshkov, D. D., Johne, R., Shelykh, I. A. & Malpuech, G. Chaotic Josephson oscillations of exciton-polaritons and their applications. *Phys. Rev. B* **80**, 235303 (2009).

[100] Read, D., Rubo, Y. G. & Kavokin, A. V. Josephson coupling of bose-einstein condensates of exciton-polaritons in semiconductor microcavities. *Phys. Rev. B* **81**, 235315 (2010).

[101] Berry, M. V. Quantal phase factors accompanying adiabatic changes. *Proc. R. Soc. A* **A 392**, 45 (1984).

[102] Suter, D., Chingas, G., Harris, R., & Pines, A. Berry's phase in magnetic resonance. *Mol. Phys.* **61**, 1327 (1987).

[103] Aharonov, Y. & Bohm, D. Significance of electromagnetic potentials in the quantum theory. *Phys. Rev.* **115**, 485–491 (1959).

[104] Klyshko, D. N. Basic quantum mechanical concepts from the operational viewpoint. *Physics-Uspekhi* **41(9)**, 885–922 (1998).

[105] Datta, S. & Das, B. Electronic analog of the electro-optic modulator. *Appl. Phys. Lett.* **56**, 665 (1990).

[106] Aronov, A. G. & Lyanda-Geller, Y. B. Spin-orbit Berry phase in conducting rings. *Phys. Rev. Lett.* **70**, 343–346 (1993).

[107] Nitta, J., Meijer, F. E. & Takayanagi, H. Spin-interference device. *Appl. Phys. Lett.* **75**, 695 (1999).

[108] Popp, M., Frustaglia, D. & Richter, K. Spin filter effects in mesoscopic ring structures. *Nanotechnology* **14**, 347 (2003).

[109] Kiselev, A. A. & Kim, K. T-shaped spin filter with a ring resonator. *J. Appl. Phys.* **94**, 4001 (2003).

[110] Shelykh, I. A., Galkin, N. G. & Bagraev, N. T. Quantum splitter controlled by Rasha spin-orbit coupling. *Phys. Rev. B* **72**, 235316 (2005).

[111] Shelykh, I. A., Bagraev, N. T., Galkin, N. G. & Klyachkin, L. E. Interplay of h/e and $h/2e$ oscillations in gate-controlled Aharonov-Bohm rings. *Phys. Rev. B* **71**, 113311 (2005).

[112] König, M. *et al.* Direct observation of the Aharonov-Casher phase. *Phys. Rev. Lett.* **96**, 076804 (2006).

[113] Glazov, M. M. & Golub, L. E. Quantum and classical multiple-scattering effects in the spin dynamics of cavity polaritons. *Phys. Rev. B* **77**, 165341 (2008).

[114] Shelykh, I. *et al.* Semiconductor microcavity as a spin-dependent optoelectronic device. *Phys. Rev. B* **70**, 035320 (2004).

[115] Leyder, C. *et al.* Interference of coherent polariton beams in microcavities: Polarization-controlled optical gates. *Phys. Rev. Lett.* **99**, 196402 (2007).

[116] Shelykh, I. A., Kavokin, A. V., Rubo, Y. G., Liew, T. C. H. & Malpuech, G. Polariton polarization-sensitive phenomena in planar semiconductor microcavities. *Semiconductor Science and Technology* **25**, 013001 (2010).

[117] Maialle, M. Z., de Andrada e Silva, E. A. & Sham, L. J. Exciton spin dynamics in quantum wells. *Phys. Rev. B* **47**, 15776–15788 (1993).

[118] Panzarini, G. *et al.* Exciton-light coupling in single and coupled semiconductor microcavities: Polariton dispersion and polarization splitting. *Phys. Rev. B* **59**, 5082–5089 (1999).

[119] Gaitan, F. Berrys phase in the presence of a non-adiabatic environment. *Journal of Magnetic Resonance* **139**, 152 (1999).

[120] Wilczek, F. & Zee, A. Appearance of gauge structure in simple dynamical systems. *Phys. Rev. Lett.* **52**, 2111–2114 (1984).

[121] Jordan, T. F. Berry phases for partial cycles. *Phys. Rev. A* **38**, 1590–1592 (1988).

[122] Samuel, J. & Bhandari, R. General setting for Berry's phase. *Phys. Rev. Lett.* **60**, 2339–2342 (1988).

[123] Messiah, A. *Mchanique quantique Tome 2* (Dunod, 1995).

[124] Bruno, P. Magnetism goes nano: Berry phase effect in magnetism. *Lecture Manuscripts of the 36th Spring School of the Institute of Solid State Research* (2005).

[125] Kaitouni, R. I. *et al.* Engineering the spatial confinement of exciton polaritons in semiconductors. *Phys. Rev. B* **74**, 155311 (2006).

[126] Lai1, C. W. *et al.* Coherent zero-state and p-state in an excitonpolariton condensate array. *Nature* **450**, 529 (2007).

[127] Balili, R., Hartwell, V., Snoke, D., Pfeiffer, L. & West, K. Bose-Einstein condensation of microcavity polaritons in a trap. *Science* **316**, 1007 (2007).

[128] Bajoni, D. *et al.* Polariton laser using single micropillar GaAs-GaAlAs semiconductor cavities. *Phys. Rev. Lett.* **100**, 047401 (2008).

[129] Kuther, A. *et al.* Confined optical modes in photonic wires. *Phys. Rev. B* **58**, 15744–15748 (1998).

[130] Meijer, F. E., Morpurgo, A. F. & Klapwijk, T. M. One-dimensional ring in the presence of Rashba spin-orbit interaction: Derivation of the correct hamiltonian. *Phys. Rev. B* **66**, 033107 (2002).

[131] Bulgakov, E. N. & Sadreev, A. F. Spin rotation for ballistic electron transmission induced by spin-orbit interaction. *Phys. Rev. B* **66**, 075331 (2002).

[132] Büttiker, M., Imry, Y. & Azbel, M. Y. Quantum oscillations in one-dimensional normal-metal rings. *Phys. Rev. A* **30**, 1982–1989 (1984).

[133] Brunetti, A. *et al.* Coherent spin dynamics of exciton-polaritons in diluted magnetic microcavities. *Phys. Rev. B* **73**, 205337 (2006).

[134] Renner, J., Worschech, L., Forchel, A., Mahapatra, S. & Brunner, K. Glass supported ZnSe microring strongly coupled to a single CdSe quantum dot. *Appl. Phys. Lett.* **93**, 151109 (2008).

[135] Martin, T. P. *et al.* Enhanced Zeeman splitting in $Ga_{0.25}In_{0.75}As$ quantum point contacts. *Appl. Phys. Lett.* **93**, 012105 (2008).

[136] Yao, W. & Niu, Q. Berry phase effect on the exciton transport and on the exciton Bose-Einstein condensate. *Phys. Rev. Lett.* **101**, 106401 (2008).

[137] Einstein, A., Podolsky, B. & Rosen, N. Can quantum-mechanical description of physical reality be considered complete? *Phys. Rev.* **47**, 777 (1935).

[138] Bohr, N. Can quantum-mechanical description of physical reality be considered complete? *Phys. Rev.* **48**, 696–702 (1935).

[139] Bohm, D. A suggested interpretation of the quantum theory in terms of hidden variables. *Phys. Rev* **85**, 166–179 (1952).

[140] Bell, J. On the Einstein Podolsky Rosen paradox. *Physics* **1**, 195–290, [Discontinued with Vol. 4, no. 1, (1968)] (1964).

[141] Bell, J. On the problem of hidden variables in quantum mechanics. *Rev. Mod. Phys.* **38**, 447–452 (1966).

[142] Clauser, J., Horne, M., Shimony, A. & Holt, R. Proposed experiment to test local hidden-variable theories. *Phys. Rev. Lett.* **23**, 880–884 (1969).

[143] Wigner, E. On hidden variables and quantum mechanical probabilities. *American Journal of Physics* **38**, 1005 (1970).

[144] Clauser, J. & Horne, M. Experimental consequences of objective local theories. *Phys. Rev. D* **10**, 526–535 (1974).

[145] Clauser, J. & Shimony, A. Bell's theorem. Experimental tests and implications. *Reports on Progress in Physics* **41**, 1881–1927 (1978).

[146] d'Espagnat, B. The quantum theory and reality. *Scientific American* **241**, 158–181 (1979).

[147] Mermin, N. Bringing home the atomic world: Quantum mysteries for anybody. *Am. J. Phys* **49**, 940–943 (1981).

[148] Mermin, N. Is the moon there when nobody looks? Reality and the quantum theory. *Physics Today* **38**, 38–47 (1985).

[149] Bohm, D. & Aharonov, Y. Discussion of experimental proof for the paradox of Einstein, Rosen, and Podolsky. *Phys. Rev.* **108**, 1070–1076 (1957).

[150] Feynman, R. Simulating physics with computers. *Intl. J. Theo. Phys.* **21**, 467488 (1982).

[151] Greenwood, G. W. Finding solutions to np problems: Philosophical differences between quantum and evolutionary search algorithms. *arXiv:quant-ph* 0010021v1 (2000).

[152] Bennet, C. H. & Brassard, G. *in Proceedings of the IEEE International Conference on Computers, Systems and Signal Processing* (IEEE, New York, 1984).

[153] Bennet, C. H. *et al.* Teleporting an unknown quantum state via dual classical and Einstein-Podolsky-Rosen channels. *Phys. Rev. Lett.* **70**, 1895 (1993).

[154] Ekert, A. K. Quantum cryptography based on Bell's theorem. *Phys. Rev. Lett.* **67**, 661–663 (1991).

[155] Jennewein, T., Simon, C., Weihs, G., Weinfurter, H. & Zeilinger, A. Quantum cryptography with entangled photons. *Phys. Rev. Lett.* **84**, 4729–4732 (2000).

[156] Scarani, V. *et al.* The security of practical quantum key distribution. *arXiv:* **0802.4155** (2008).

[157] Benson, O., Santori, C., Pelton, M. & Yamamoto, Y. Regulated and entangled photons from a single quantum dot. *Phys. Rev. Lett.* **84**, 2513 (2000).

[158] Gammon, D., Snow, E. S., Shanabrook, B. V., Katzer, D. S. & Park, D. Fine structure splitting in the optical spectra of single GaAs quantum dots. *Phys. Rev. Lett.* **76**, 3005 (1996).

[159] Kulakovskii, V. D. *et al.* Fine structure of biexciton emission in symmetric and asymmetric CdSe/ZnSe single quantum dots. *Phys. Rev. Lett.* **82**, 1780 – 1783 (1999).

[160] Stevenson, R. M. *et al.* Evolution of entanglement between distinguishable light states. *Phys. Rev. Lett.* **101**, 170501 (2008).

[161] R. Hafenbrak, P. M. L. W.-A. R., S. M. Ulrich & Schmidt, O. G. Triggered polarization-entangled photon pairs from a single quantum dot up to 30 K. *New Journal of Physics* **9**, 315 (2007).

[162] Stevenson, R. M. *et al.* A semiconductor source of triggered entangled photon pairs. *Nature* **439**, 179 (2006).

[163] Young, R. J. *et al.* Improved fidelity of triggered entangled photons from single quantum dots. *New Journal of Physics* **8**, 29 (2006).

[164] Peres, A. Separability criterion for density matrices. *Phys. Rev. Lett.* **77**, 1413 (1996).

[165] Akopian, N. *et al.* Entangled photon pairs from semiconductor quantum dots. *Phys. Rev. Lett.* **96**, 130501 (2006).

[166] Vogel, M. M. *et al.* Influence of lateral electric fields on multiexcitonic transitions and fine structure of single quantum dots. *Appl. Phys. Lett* **91**, 051904 (2007).

[167] Gerardot, B. *et al.* Manipulating exciton fine structure in quantum dots with a lateral electric field. *Appl. Phys. Lett.* **90**, 041101 (2007).

[168] Pfanner, G., Seliger, M. & Hohenester, U. Entangled photon sources based on semiconductor quantum dots: The role of pure dephasing. *Phys. Rev. B* **78**, 195410 (2008).

[169] Johne, R. *et al.* Entangled photon pairs produced by a quantum dot strongly coupled to a microcavity. *Phys. Rev. Lett* **100**, 240404 (2008).

[170] Kavokin, A. V., Baumberg, J. J., Malpuech, G. & Laussy, F. P. *Microcavities* (Oxford University Press, 2007).

[171] Shirane, M. *et al.* Mode identification of high-quality-factor single-defect nanocavities in quantum dot-embedded photonic crystals. *J. Appl. Phys.* **101**, 073107 (2007).

[172] Reithmaier, J. P. *et al.* Strong coupling in a single quantum dotsemiconductor microcavity system. *Nature* **432**, 197 (2004).

[173] Peter, E. *et al.* Exciton-photon strong-coupling regime for a single quantum dot embedded in a microcavity. *Phys. Rev. Lett.* **95**, 067401 (2005).

[174] Cohen-Tannoudji, C., Dupont-Roc, J. & Grynberg, G. *Atom-Photons Interactions* (John Wiley & Sons, New York, 1992).

[175] Wootters, W. Entanglement of formation of an arbitrary state of two qubits. *Phys. Rev. Lett.* **80**, 2245–2248 (1998).

[176] Yu, T. & Eberly, J. H. Evolution from entanglement to decoherence of bipartite mixed "X" states. *arXiv:quant-ph/0503089* (2005).

[177] Yonac, M., Yu, T. & Eberly, J. H. Pairwise concurrence dynamics: a four-qubit model. *J. Phys. B* **40**, S45 (2007).

[178] Hennessy, K., Hogerle, C., Hu, E., Badolato, A. & Imamoglu, A. Tuning photonic nanocavities by atomic force microscope nano-oxidation. *Appl. Phys. Lett.* **89**, 041118 (2006).

[179] Winger, M., Badolato, A., Hennessy, K. J., Hu, E. L. & Imamoglu, A. Quantum dot spectroscopy using cavity QED. *Phys. Rev. Lett.* **101**, 226808 (2008).

[180] Pathak, P. K. & Hughes, S. Generation of entangled photon-pairs from a single quantum dot embedded in a planar photonic-crystal cavity. *arXiv:0812.2474* (2009).

[181] Laussy, F. P., del Valle, E. & Tejedor, C. Strong coupling of quantum dots in microcavities. *Physical Review Letters* **101**, 083601 (2008).

[182] Hennessy, K. *et al.* Quantum nature of a strongly coupled single quantum dotcavity system. *Nature* **445**, 896 (2007).

[183] Yoshie, T. *et al.* Vacuum rabi splitting with a single quantum dot in a photonic crystal nanocavity. *Nature* **432**, 200 (2004).

[184] Vuckovic, J. & Yamamoto, Y. Photonic crystal microcavities for cavity quantum electrodynamics with a single quantum dot. *Appl. Phys. Lett.* **82**, 15 (2003).

[185] Dousse, A. *et al.* Controlled light-matter coupling for a single quantum dot embedded in a pillar microcavity using far-field optical lithography. *Phys. Rev. Lett.* **101**, 267404 (2008).

[186] Vamivakas, A., Zhao, Y., Lu, C. & Atatüre, M. Spin-resolved quantum-dot resonance fluorescence. *Nature Physics* **5**, 198–202 (2009).

[187] Flagg, E. *et al.* Resonantly driven coherent oscillations in a solid-state quantum emitter. *Nature Physics* **5**, 203–207 (2009).